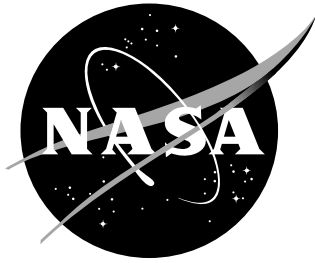


NASA/TM-2006-214296



# Exploratory Studies in Generalized Predictive Control for Active Gust Load Alleviation

*Raymond G. Kvaternik, Kenneth W. Eure, and Jer-Nan Juang  
Langley Research Center, Hampton, Virginia*

---

April 2006

## *The NASA STI Program Office ... in Profile*

Since its founding, NASA has been dedicated to the advancement of aeronautics and space science. The NASA Scientific and Technical Information (STI) Program Office plays a key part in helping NASA maintain this important role.

The NASA STI Program Office is operated by Langley Research Center, the lead center for NASA's scientific and technical information. The NASA STI Program Office provides access to the NASA STI Database, the largest collection of aeronautical and space science STI in the world. The Program Office is also NASA's institutional mechanism for disseminating the results of its research and development activities. These results are published by NASA in the NASA STI Report Series, which includes the following report types:

- **TECHNICAL PUBLICATION.** Reports of completed research or a major significant phase of research that present the results of NASA programs and include extensive data or theoretical analysis. Includes compilations of significant scientific and technical data and information deemed to be of continuing reference value. NASA counterpart of peer-reviewed formal professional papers, but having less stringent limitations on manuscript length and extent of graphic presentations.
- **TECHNICAL MEMORANDUM.** Scientific and technical findings that are preliminary or of specialized interest, e.g., quick release reports, working papers, and bibliographies that contain minimal annotation. Does not contain extensive analysis.
- **CONTRACTOR REPORT.** Scientific and technical findings by NASA-sponsored contractors and grantees.

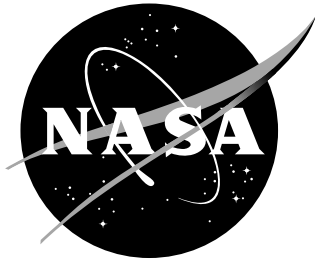
- **CONFERENCE PUBLICATION.** Collected papers from scientific and technical conferences, symposia, seminars, or other meetings sponsored or co-sponsored by NASA.
- **SPECIAL PUBLICATION.** Scientific, technical, or historical information from NASA programs, projects, and missions, often concerned with subjects having substantial public interest.
- **TECHNICAL TRANSLATION.** English-language translations of foreign scientific and technical material pertinent to NASA's mission.

Specialized services that complement the STI Program Office's diverse offerings include creating custom thesauri, building customized databases, organizing and publishing research results ... even providing videos.

For more information about the NASA STI Program Office, see the following:

- Access the NASA STI Program Home Page at <http://www.sti.nasa.gov>
- E-mail your question via the Internet to [help@sti.nasa.gov](mailto:help@sti.nasa.gov)
- Fax your question to the NASA STI Help Desk at (301) 621-0134
- Phone the NASA STI Help Desk at (301) 621-0390
- Write to:  
NASA STI Help Desk  
NASA Center for Aerospace Information  
7121 Standard Drive  
Hanover, MD 21076-1320

NASA/TM-2006-214296



# Exploratory Studies in Generalized Predictive Control for Active Gust Load Alleviation

*Raymond G. Kvaternik, Kenneth W. Eure, and Jer-Nan Juang  
Langley Research Center, Hampton, Virginia*

National Aeronautics and  
Space Administration

Langley Research Center  
Hampton, Virginia 23681-2199

---

April 2006

The use of trademarks or names of manufacturers in this report is for accurate reporting and does not constitute an official endorsement, either expressed or implied, of such products or manufacturers by the National Aeronautics and Space Administration.

---

Available from:

NASA Center for AeroSpace Information (CASI)  
7121 Standard Drive  
Hanover, MD 21076-1320  
(301) 621-0390

National Technical Information Service (NTIS)  
5285 Port Royal Road  
Springfield, VA 22161-2171  
(703) 605-6000

## Table of Contents

Abstract.....	1
Nomenclature.....	1
Introduction.....	2
Basic Features of GPC.....	3
Pertinent Equations Underlying the GPC Method.....	4
Form of System and Control Law Equations.....	5
System Identification.....	5
Multi-Step Output Prediction Equation.....	7
Derivation of Control Law.....	9
Selection of Control Model Parameters.....	10
Practical Issues.....	10
Treatment of External Disturbances.....	11
Basic Signal Processing Guidelines.....	11
Results and Discussion.....	12
Comment on Codes Used for Simulation.....	12
Numerical Simulations Using 3-DOF Math Model.....	12
Representative Results.....	14
Steady-State Disturbances.....	14
Non-Steady-State Disturbances.....	15
Summary of Observations.....	15
Numerical Simulations Using Data from Wind-Tunnel Test of HiLDA Wing Model.....	16
Test Conditions.....	16
Test Procedures.....	17
Simulation Conditions and Parameter Settings.....	17
Representative Results.....	18
Feedback with Embedded Feedforward.....	19
Feedback with Explicit Feedforward.....	20
Summary of Observations.....	20
Concluding Remarks.....	21
Appendix A — Treatment of Measurable Coherent Disturbances.....	22
Batch Identification of Disturbance Models.....	23
Adaptive Identification of Disturbance Models.....	23
Appendix B — State-Space Equations for 3-DOF Mass-Spring-Dashpot System.....	34
References.....	37
Tables.....	39
Figures.....	40



## Abstract

*The results of numerical simulations aimed at assessing the efficacy of Generalized Predictive Control (GPC) for active gust load alleviation using trailing- and leading-edge control surfaces are presented. GPC is a linear, time-invariant, multi-input/multi-output predictive control method that uses an AutoRegressive with eXogenous input (ARX) model to characterize the system and to design the controller. The equations underlying the method are presented and discussed, including system identification, calculation of control law matrices, and calculation of the commands applied to the control effectors. Both embedded and explicit feedforward paths for incorporation of disturbance effects are addressed. Representative results from two types of simulations are presented. The first used a three-degree-of-freedom mathematical model of a mass-spring-dashpot system subject to a variety of user-defined external disturbances. The second used open-loop data obtained during a wind-tunnel test in which a wing model was subjected to sinusoidal vertical gust excitation; closed-loop behavior was simulated in post-test calculations. Results obtained from these simulations have been decidedly positive. In particular, the closed-loop simulations for the wing model showed reductions in wing root moments by factors as high as 1000, depending on whether the excitation is from a constant- or swept-frequency gust and on the direction of the response.*

## Nomenclature

AR	AutoRegressive
ARX	AutoRegressive with eXogenous input
$d$	disturbance acting on plant
$d_k, d_u$	known and unknown portions of disturbance
GPC	Generalized Predictive Control
$h_p, h_c$	prediction and control horizons
$k$	integer denoting time index
$\ell$	number of data points used for system identification
$m$	number of outputs
$n_d$	order of AR disturbance model
OMP	Observer Markov Parameters
$p$	order of ARX model used for system identification

$r$	total number of inputs ( $r = r_c + r_d$ )
$r_c$	number of control inputs
$r_d$	number of disturbance inputs
SID	System IDentification
$\mathcal{T}, \mathcal{A}, \mathcal{B}, \mathcal{D}_p, \mathcal{D}_f$	coefficient matrices in multi-step output prediction equation
$u$	input
$u_c$	control input
$u_c(k)$	control input at time step $k$
$u(k), y(k), d(k)$	vectors of inputs, outputs, and disturbances at $k^{\text{th}}$ time step
$u(k-j), y(k-j), d(k-j)$	vectors of past inputs, outputs, and disturbances at $(k-j)^{\text{th}}$ time step; $j < k$
$u(k+j), y(k+j), d(k+j)$	vectors of future inputs, outputs, and disturbances at $(k+j)^{\text{th}}$ time step; $j \geq 0$
$y$	output
$\bar{Y}$	matrix of observer Markov parameters
$\chi^c, \alpha^c, \beta^c, \delta^c, \gamma^c$	control law gain matrices
$\alpha_i, \beta_i$ and $\gamma_i$	observer Markov parameters

## Introduction

The Aeroelasticity Branch and the Army Research Laboratory's Vehicle Technology Directorate at NASA Langley Research Center, in collaboration with Bell Helicopter Textron Inc, have recently completed a series of experimental evaluations of a predictive control technique known as Generalized Predictive Control (GPC) (ref. 1) to assess its potential for actively controlling the swashplate of tiltrotor aircraft to enhance aeroelastic stability in both helicopter and airplane modes of flight. The studies employed a 1/5-scale, semispan aeroelastic model of the V-22 that had been refurbished to serve as a tiltrotor research testbed for use in the Langley Transonic Dynamics Tunnel (TDT). The results of the exploratory experimental investigations conducted with this model using a multi-input/multi-output GPC-based method for active control are reported in references 2-5. The GPC algorithm employed was highly effective in increasing the stability of the critical (least stable) mode for all of the configurations and conditions tested. GPC has apparently not yet been employed to evaluate its potential for active

gust load alleviation (GLA) of fixed-wing aircraft using wing control surfaces. To this end, the intention was to upgrade and extend the GPC-based software system that was developed for the tiltrotor model and to conduct an investigation of the GPC method for active gust load alleviation as an adjunct to a planned test in the TDT of a large semi-span wing model of a SensorCraft concept being studied by Northrop Grumman as part of a High Lift over Drag Active (HiLDA) Wing Program (ref. 6). Although it was not possible to make all the necessary changes to the software in time for the subject test, appropriate data were taken during the test with the objective of conducting a post-test assessment and evaluation of the method.

The purpose of this report is to present results of numerical simulations obtained from recently-developed MATLAB (ref. 7) programs intended to serve as the basis for the planned extensions to the tiltrotor GPC software system. First, a qualitative discussion of the essential features of GPC is given. Then, the equations underlying the method are presented and discussed, including system identification, calculation of control law matrices, and calculation of the commands applied to the control effectors. Procedures for incorporation of both known and unknown disturbance effects are addressed. Some general but relevant comments on the treatment of external disturbances, signal processing, and the codes developed and used for the simulations are then presented. Representative results from two types of simulations of open- and closed-loop behavior are presented next. The first set of simulations was made using a three-degree-of-freedom mathematical model of a mass-spring-dashpot system subject to a variety of user-defined external disturbances. The second set of simulations was made using data obtained during the HiLDA wing test conducted in the TDT in September 2004 (ref. 6) in which the model was subjected to sinusoidal vertical gust excitation at constant and continuously varying frequencies. The particular results presented from each type of simulation were chosen to illustrate the potential gust-load-alleviation capability that can be obtained with a GPC-based active control system.

## **Basic Features of GPC**

Predictive control refers to a strategy wherein the decision for the current control action is based on minimization of a quadratic objective function that involves a prediction of the system response at some number of time steps into the future. A variety of predictive controllers have been proposed (ref. 8). Among these, Generalized Predictive Control, which was introduced in 1987 (ref. 9), has received notable attention by researchers. GPC is a linear, time-invariant, multi-input/multi-output predictive control method that uses an AutoRegressive with eXogenous input (ARX) model (i.e., a linear difference equation) to describe the input-output relationship of the system. The coefficient matrices of the ARX equation are determined by system identification. Such a model gives the current outputs as a linear combination of past inputs and outputs. The input-output equation is used to form a multi-step output prediction equation over a finite prediction horizon. An expression for the control to be imposed at the next time step is determined by minimizing the deviation of the predicted controlled plant outputs from the desired (or target) outputs, subject to a penalty on control effort. A version of the GPC procedure was developed at NASA Langley Research Center in 1997 for efficient computation and unknown disturbance rejection by Dr. Jer-Nan Juang and his associates. Their work resulted in a suite of MATLAB m-files that were collected into a predictive control toolbox that can be

used by researchers for GPC studies. A summary of the theory underlying their development is found in references 1 and 10-20, among others.

The essential features of a GPC-based control system are depicted in figure 1. The system has  $r_c$  control inputs  $u$ ,  $m$  measured outputs  $y$ , and is subject to external disturbances  $d$  that may be regarded as having known ( $d_k$ ) and unknown ( $d_u$ ) portions. Measurement noise (not shown) is also present. There are two fundamental steps involved in GPC implementation: (1) identification of the system, and (2) use of the identified model to design a controller. Any system identification technique that returns an ARX model for the system may be used. System identification is done on-line, but not necessarily at every time point, in the presence of the disturbances acting on the system. If all the external disturbances are unknown (or treated as unknown), the effects of the disturbance-induced output are automatically embedded in the identified model and there is no need for explicit inclusion of disturbance terms in the ARX model (ref. 1). This approach leads to a feedback controller with embedded (or implicit) feedforward. However, if any of the disturbances acting on the system are either known or measurable, that data can be used in a feedforward path simultaneously with the feedback data to enhance closed-loop performance, as suggested in figure 1. In this situation, the identified ARX model includes the effects of the disturbance-induced output associated with the unknown disturbances while an AutoRegressive (AR) model identified on-line can be used to include the effects of the measurable disturbances. This approach leads to a feedback controller with both embedded and explicit feedforward. In either case, the parameters of the identified model are used to compute the predictive control law. A random excitation  $u_{id}$  is applied initially with  $u_c$  equal to zero to identify the open-loop system. Dither is added to the closed-loop control input  $u_c$  if it is necessary to re-identify the system while operating in the closed-loop mode. It should be pointed out that this method lends itself to implementation strategies that allow all computations to be done on-line and in real time, as was demonstrated in experimental investigations with the tiltrotor model.

The GPC software system developed for the tiltrotor model identifies the plant and computes the control law gain matrices assuming that the aerodynamic forces (the disturbances) acting on the model are unknown. This is the case of feedback with embedded feedforward described above and represents the capability that was incorporated in the m-files of the aforementioned predictive control toolbox. A Langley team has recently identified, implemented (as MATLAB codes), and verified the changes needed to include a feedforward path in the GPC-based software system developed for the tiltrotor model. This extension was motivated by the fact that the data needed for a feedforward path would be available from the HiLDA wing test in the form of gust-induced flow-angle measurements made upstream of the model. It is not difficult to envision other active control situations in which one or more of the disturbances acting on a system are measurable (or known) and which could take advantage of feedforward control.

### **Pertinent Equations Underlying the GPC Method**

The key ingredients of the GPC method are system identification and output prediction based on the identified model; the control law is then derived by minimizing the error between

the predicted output and the desired output. The section begins by showing the general form of the system and control law equations.

### Form of System and Control Law Equations

The relationship between the input and output discrete time histories of a linear, time invariant, multi-input/multi-output (MIMO) system is described by an ARX model that has the form

$$y(k) = \alpha_1 y(k-1) + \alpha_2 y(k-2) + \dots + \alpha_p y(k-p) + \beta_0 u(k) + \beta_1 u(k-1) + \dots + \beta_p u(k-p) + \gamma_0 d(k) + \gamma_1 d(k-1) + \dots + \gamma_p d(k-p) \quad (1)$$

This equation states that the current output  $y(k)$  at time step  $k$  may be estimated by using  $p$  sets of the previous output, input, and disturbance measurements,  $y(k-1), \dots, y(k-p)$ ,  $u(k-1), \dots, u(k-p)$ , and  $d(k-1), \dots, d(k-p)$ ; and the current input and disturbance measurements  $u(k)$  and  $d(k)$ . The integer  $p$  is called the order of the ARX model. The coefficient matrices  $\alpha_i$ ,  $\beta_i$  and  $\gamma_i$  are referred to as observer Markov parameters (OMP) or ARX parameters and are the quantities to be determined by the identification algorithm. Closed-loop performance is enhanced by performing the system identification in the presence of the external disturbances acting on the system, thereby ensuring that disturbance information will be incorporated in the system model. The goal of system identification is to determine the OMP based on input and output data. The OMP may be determined by any identification technique that returns an ARX model of the system.

The ARX model is used to design the controller that, in the case of a regulator problem, has the general form given by

$$u_c(k) = \alpha_1^c y(k-1) + \alpha_2^c y(k-2) + \dots + \alpha_p^c y(k-p) + \beta_1^c u(k-1) + \beta_2^c u(k-2) + \dots + \beta_p^c u(k-p) + \delta_1^c d(k-1) + \delta_2^c d(k-2) + \dots + \delta_p^c d(k-p) + \gamma_1^c d(k) + \gamma_2^c d(k+1) + \dots + \gamma_p^c d(k+p-1) \quad (2)$$

Equation 2 indicates that the current control input  $u_c(k)$  may be computed using  $p$  sets of the previous input and output measurements,  $u(k-1), \dots, u(k-p)$ ,  $d(k-1), \dots, d(k-p)$ , and  $y(k-1), \dots, y(k-p)$ ; and the future disturbances  $d(k), d(k+1), \dots, d(k+p-1)$ . The coefficient matrices  $\alpha^c$ ,  $\beta^c$ ,  $\delta^c$ , and  $\gamma^c$  are the control law gain matrices. If the  $p$  past disturbances  $d(k-1), d(k-1), \dots, d(k-p)$  are measurable (known) they can be inserted directly into equation 2. The future disturbances,  $d(k), d(k+1), \dots, d(k+p-1)$ , are typically unknown. However, if there is correlation in the disturbance signal (such as in the sinusoidal gust excitation of the HiLDA wing model) an AutoRegressive (AR) model of the disturbance can be determined and used to predict the future disturbances needed in equation 2.

### System Identification

System identification (SID) in the presence of the operational disturbances is the first of the two major computational steps of the GPC method. The number of control inputs is  $r_c$ , the number of disturbance inputs is  $r_d$ , the number of measured outputs is  $m$ , and  $r = r_c + r_d$ . To initiate the identification process, the system is excited with band-limited white noise. These independent random excitations are applied to the  $r_c$  inputs simultaneously and the  $m$  responses

are measured. The resulting input and output time histories ( $u$  and  $y$ ) at  $\ell$  time points are then used to form the data matrices  $y$  and  $V$  in the equation

$$y = \bar{Y} V \quad (3)$$

where

$$y = \begin{bmatrix} y(0) & y(1) & y(2) & \cdots & y(p) & \cdots & y(\ell-1) \end{bmatrix} \quad (4)$$

$m \times \ell$

and

$$V = \begin{bmatrix} d(0) & d(1) & d(2) & \cdots & d(p) & \cdots & d(\ell-1) \\ u(0) & u(1) & u(2) & & u(p) & & u(\ell-1) \\ & v(0) & v(1) & \cdots & v(p-1) & \cdots & v(\ell-2) \\ & & v(0) & \cdots & v(p-2) & \cdots & v(\ell-3) \\ & & & \ddots & \vdots & \cdots & \vdots \\ & & & & v(0) & \cdots & v(\ell-p-1) \end{bmatrix} \quad (5)$$

$[r+(r+m)p] \times \ell$

Equations 4 and 5 follow from writing the equations for a discrete-time state-space observer model of a linear time-invariant system at a sequence of time steps  $k = 0, 1, 2, \dots, (\ell-1)$  and grouping (assembling) them into a matrix form (ref. 11). Equations 4 and 5 are valid under the assumption that the system is initially at rest. For nonzero unknown initial conditions, the first  $p$  columns of  $y$  and  $V$  must be deleted to eliminate the effect of the initial conditions (ref. 11). The vector  $v(k)$  appearing in the data matrix  $V$  is formed from the vectors  $d(k)$ ,  $u(k)$  and  $y(k)$  according to

$$v(k) = \begin{Bmatrix} d(k) \\ u(k) \\ y(k) \end{Bmatrix} \quad (6)$$

$(r+m) \times 1$

The order of the ARX model,  $p$ , and the number of time steps,  $\ell$ , are specified by the user. Some guidelines for their selection are given later. The sizes of key vectors and matrices are noted here and throughout the report as appropriate to facilitate computational considerations related to computer implementation.

In forming the matrices given in equations 4 and 5, it has been assumed that a deadbeat observer has been added to the system (ref. 18). It is through this assumption that the matrix  $V$  can be reduced to a size amenable for practical numerical computation of its pseudo-inverse. The system identification process yields observer Markov parameters rather than system Markov parameters because of the inclusion of the observer. A complete discussion of these aspects of the development may be found in reference 11.

In equation 3,  $\bar{Y}$  is the matrix of observer Markov parameters that is to be identified and has the form

$$\bar{Y} = \begin{bmatrix} \gamma_0 & \beta_0 & \gamma_1 & \beta_1 & \alpha_1 & \gamma_2 & \beta_2 & \alpha_2 & \gamma_3 & \beta_3 & \alpha_3 & \cdots & \gamma_p & \beta_p & \alpha_p \end{bmatrix} \quad (7)$$

$m \times [r + (r+m)p]$

The solution for  $\bar{Y}$  is obtained by solving equation 3 for  $\bar{Y}$  according to

$$\bar{Y} = y V^\dagger = y V^T [V V^T]^{-1} \quad (8)$$

where  $\dagger$  denotes the pseudo-inverse. If the product  $V V^T$  is a well-conditioned matrix of reasonable size, the ordinary inverse can be taken as shown. Otherwise, a pseudo-inverse must be used.

### Multi-Step Output Prediction Equation

The one-step-ahead output prediction equation given in equation 1 is the starting point for deriving the multi-step output prediction equation that is needed for designing a GPC controller. Using equation 1, the output at time step  $k+j$  may be written in the form

$$\begin{aligned} y(k+j) = & \alpha_1^{(j)} y(k-1) + \alpha_2^{(j)} y(k-2) + \cdots + \alpha_p^{(j)} y(k-p) \\ & + \beta_0 u(k+j) + \beta_0^{(1)} u(k+j-1) + \cdots + \beta_o^{(j)} u(k) + \beta_1^{(j)} u(k-1) + \beta_2^{(j)} u(k-2) + \cdots + \beta_p^{(j)} u(k-p) \\ & + \gamma_0 d(k+j) + \gamma_0^{(1)} d(k+j-1) + \cdots + \gamma_o^{(j)} d(k) + \gamma_1^{(j)} d(k-1) + \gamma_2^{(j)} d(k-2) + \cdots + \gamma_p^{(j)} d(k-p) \end{aligned} \quad (9)$$

where the coefficient matrices are given by recursive expressions involving the matrices  $\alpha_i$ ,  $\beta_i$ , and  $\gamma_i$  appearing in the ARX equation (ref. 10). The system identification process described earlier determines the matrices  $\alpha_i$ ,  $\beta_i$ , and  $\gamma_i$ . Equation 9 shows that the output  $y(k+j)$  at time step  $k+j$  may be estimated by using  $p$  sets of the previous output and input measurements,  $y(k-1), \dots, y(k-p)$  and  $u(k-1), \dots, u(k-p)$ , and the (unknown) current and future inputs  $u(k), u(k+1), \dots, u(k+j)$  and disturbances  $d(k), d(k+1), \dots, d(k+j)$ . The GPC algorithm is based on system output predictions over a finite horizon  $h_p$  known as the prediction horizon. To predict future plant outputs, some assumption needs to be made about future control inputs. In determining the future control inputs for GPC, it is assumed that control is applied over a finite horizon  $h_c$  known as the control horizon that is equal to or less than the prediction horizon. Beyond the control horizon the control input is assumed to be zero. Letting  $j$  in equation 9 range over the set of values  $j = 1, 2, \dots, h_p-1$ , the resulting equations can be assembled into a multi-step output prediction equation having the form

$$\begin{aligned} y_{h_p}(k) = & \mathcal{T} \begin{matrix} u_{h_c}(k) \\ h_p m \times h_c r_c \quad h_c r_c \times 1 \end{matrix} + \mathcal{B} \begin{matrix} u_p(k-p) \\ h_p m \times p r_c \quad p r_c \times 1 \end{matrix} + \mathcal{A} \begin{matrix} y_p(k-p) \\ h_p m \times p m \quad p m \times 1 \end{matrix} \\ & + \mathcal{D}_p \begin{matrix} d_p(k-p) \\ h_p m \times p r_d \quad p r_d \times 1 \end{matrix} + \mathcal{D}_f \begin{matrix} d_f(k) \\ h_p m \times h_p r_d \quad h_p r_d \times 1 \end{matrix} \end{aligned} \quad (10)$$

The coefficient matrices  $\mathcal{T}$ ,  $\mathcal{A}$ ,  $\mathcal{B}$ ,  $\mathcal{D}_p$  and  $\mathcal{D}_f$  are formed from combinations of the observer Markov parameters  $\alpha_i$ ,  $\beta_i$ , and  $\gamma_i$ . The quantity  $y_{h_p}(k)$  is the vector containing the future outputs, whereas  $u_{h_c}(k)$  is the vector containing the future control inputs yet to be determined. The

quantities  $u_p(k-p)$ ,  $y_p(k-p)$ , and  $d_p(k-p)$  are vectors containing the previous  $p$  sets of control inputs, outputs, and disturbance inputs, respectively. The vector  $d_f(k)$  contains the future disturbance inputs, which are usually unknown. However, if the disturbance is a coherent signal, future values of the disturbance can be estimated using an AR model of the disturbance obtained in a separate identification computation using a portion of the measured disturbance time history. The expanded form of this multi-step output prediction equation for  $h_c \leq h_p$  is shown in equation 11.

$$\begin{aligned}
& \boxed{\beta_0^{(q)} = \beta_1^{(q-1)} + \alpha_1^{(q-1)} \beta_0} \\
& \begin{pmatrix} y(k) \\ y(k+1) \\ \vdots \\ y(k+q-1) \\ y(k+q) \\ \vdots \\ y(k+h_p-1) \end{pmatrix} = \begin{pmatrix} \beta_o \\ \beta_o^{(1)} & \beta_o & & \\ \vdots & \vdots & \ddots & \\ \beta_o^{(q-1)} & \beta_o^{(q-2)} & \dots & \beta_o \\ \beta_o^{(q)} & \beta_o^{(q-1)} & \dots & \beta_o^{(1)} \\ \vdots & \vdots & \ddots & \vdots \\ \beta_o^{(h_p-1)} & \beta_o^{(h_p-2)} & \dots & \beta_o^{(h_p-h_c)} \end{pmatrix} \begin{pmatrix} u(k) \\ u(k+1) \\ \vdots \\ u(k+h_c-1) \end{pmatrix} \quad h_c \leq h_p
\end{aligned}$$
  

$$\begin{aligned}
& \boxed{\alpha_{p-1}^{(q)} = \alpha_p^{(q-1)} + \alpha_1^{(q-1)} \alpha_{p-1}} \quad \boxed{\beta_{p-1}^{(q)} = \beta_p^{(q-1)} + \alpha_1^{(q-1)} \beta_{p-1}} \\
& \begin{pmatrix} \alpha_1 & \alpha_2 & \dots & \alpha_{p-1} & \alpha_p \\ \alpha_1^{(1)} & \alpha_2^{(1)} & \dots & \alpha_{p-1}^{(1)} & \alpha_p^{(1)} \\ \vdots & \vdots & \ddots & \vdots & \vdots \\ \alpha_1^{(q-1)} & \alpha_2^{(q-1)} & \dots & \alpha_{p-1}^{(q-1)} & \alpha_p^{(q-1)} \\ \alpha_1^{(q)} & \alpha_2^{(q)} & \dots & \alpha_{p-1}^{(q)} & \alpha_p^{(q)} \\ \vdots & \vdots & \ddots & \vdots & \vdots \\ \alpha_1^{(h_p-1)} & \alpha_2^{(h_p-1)} & \dots & \alpha_{p-1}^{(h_p-1)} & \alpha_p^{(h_p-1)} \end{pmatrix} \begin{pmatrix} y(k-1) \\ y(k-2) \\ \vdots \\ y(k-p+1) \\ y(k-p) \end{pmatrix} + \begin{pmatrix} \beta_1 & \beta_2 & \dots & \beta_{p-1} & \beta_p \\ \beta_1^{(1)} & \beta_2^{(1)} & \dots & \beta_{p-1}^{(1)} & \beta_p^{(1)} \\ \vdots & \vdots & \ddots & \vdots & \vdots \\ \beta_1^{(q-1)} & \beta_2^{(q-1)} & \dots & \beta_{p-1}^{(q-1)} & \beta_p^{(q-1)} \\ \beta_1^{(q)} & \beta_2^{(q)} & \dots & \beta_{p-1}^{(q)} & \beta_p^{(q)} \\ \vdots & \vdots & \ddots & \vdots & \vdots \\ \beta_1^{(h_p-1)} & \beta_2^{(h_p-1)} & \dots & \beta_{p-1}^{(h_p-1)} & \beta_p^{(h_p-1)} \end{pmatrix} \begin{pmatrix} u(k-1) \\ u(k-2) \\ \vdots \\ u(k-p+1) \\ u(k-p) \end{pmatrix}
\end{aligned}$$
  

$$\begin{aligned}
& \boxed{\gamma_{p-1}^{(q)} = \gamma_p^{(q-1)} + \alpha_1^{(q-1)} \gamma_{p-1}} \quad \boxed{\gamma_0^{(q)} = \gamma_1^{(q-1)} + \alpha_1^{(q-1)} \gamma_0} \\
& \begin{pmatrix} \gamma_1 & \gamma_2 & \dots & \gamma_{p-1} & \gamma_p \\ \gamma_1^{(1)} & \gamma_2^{(1)} & \dots & \gamma_{p-1}^{(1)} & \gamma_p^{(1)} \\ \vdots & \vdots & \ddots & \vdots & \vdots \\ \gamma_1^{(q-1)} & \gamma_2^{(q-1)} & \dots & \gamma_{p-1}^{(q-1)} & \gamma_p^{(q-1)} \\ \gamma_1^{(q)} & \gamma_2^{(q)} & \dots & \gamma_{p-1}^{(q)} & \gamma_p^{(q)} \\ \vdots & \vdots & \ddots & \vdots & \vdots \\ \gamma_1^{(h_p-1)} & \gamma_2^{(h_p-1)} & \dots & \gamma_{p-1}^{(h_p-1)} & \gamma_p^{(h_p-1)} \end{pmatrix} \begin{pmatrix} d(k-1) \\ d(k-2) \\ \vdots \\ d(k-p+1) \\ d(k-p) \end{pmatrix} + \begin{pmatrix} \gamma_o \\ \gamma_o^{(1)} & \gamma_o & & \\ \vdots & \vdots & \ddots & \\ \gamma_o^{(q-1)} & \gamma_o^{(q-2)} & \dots & \gamma_o \\ \gamma_o^{(q)} & \gamma_o^{(q-1)} & \dots & \gamma_o^{(1)} & \gamma_o \\ \vdots & \vdots & \dots & \gamma_o^{(2)} & \gamma_o^{(1)} & \gamma_o \\ \gamma_o^{(h_p-1)} & \gamma_o^{(h_p-2)} & \dots & \gamma_o^{(3)} & \gamma_o^{(2)} & \gamma_o^{(1)} & \gamma_o \end{pmatrix} \begin{pmatrix} d(k) \\ d(k+1) \\ \vdots \\ d(k+h_p-1) \end{pmatrix}
\end{aligned}$$

(11)

The observer Markov parameters  $\alpha_i$ ,  $\beta_i$ , and  $\gamma_i$  determined in system identification are used to form the first block row in each of the coefficient matrices  $\mathcal{T}$ ,  $\mathcal{A}$ ,  $\mathcal{B}$ ,  $\mathcal{D}_p$  and  $\mathcal{D}_f$  in equation 10. These terms are colored red in equation 11. The terms in the remaining block rows are computed using the recursive relations indicated in the boxes above the coefficient matrices in equation 11 (ref. 10). All terms in equation 11 are known, except for the  $h_c$  sets of future commands, the  $h_p$  sets of predicted responses, and the  $h_p$  sets of future disturbance inputs  $d_f(k)$ . The goal of the GPC control algorithm is to determine the set of future commands  $u(k)$ ,  $u(k+1)$ , ...,  $u(k+h_c-1)$  that are required to achieve a desired predicted response  $y(k)$ ,  $y(k+1)$ , ...,  $y(k+h_p-1)$ . It should be noted that the system Markov parameters, which are commonly used as the basis for identifying discrete-time models for linear dynamical systems, form the first block column in the matrix  $\mathcal{T}$ ; the remaining block columns are formed from subsets of these parameters. The system Markov parameters are the pulse response of a system and are unique for a given linear system. The discrete-time state-space matrices  $A$ ,  $B$ ,  $C$ , and  $D$  are embedded in the system Markov parameters.

### Derivation of Control Law

The predictive control law is obtained by minimizing the deviation of the predicted controlled response (as computed from the multi-step output prediction equation) from a desired response over a prediction horizon  $h_p$ . To this end, one first defines an error function that is the difference between the desired (target) response  $y_T(k)$  and the predicted response  $y_{hp}(k)$ :

$$\begin{aligned}\mathcal{E} &= y_T(k) - y_{hp}(k) \\ &= y_T(k) - \mathcal{T}u_{h_c}(k) - \mathcal{B}u_p(k-p) - \mathcal{A}y_p(k-p) - \mathcal{D}_p d_p(k-p) - \mathcal{D}_f d_f(k)\end{aligned}\quad (12)$$

An objective function  $J$  quadratic in the error and the unknown future controls is then formed:

$$J = \mathcal{E}^T Q \mathcal{E} + u_{h_c}^T R u_{h_c} \quad (13)$$

Two weighting matrices are included in the objective function:  $R$  (symmetric and positive definite) is used to weight the control effort and stabilize the closed-loop system;  $Q$  (symmetric and positive semi-definite) is used to weight the relative importance of the differences between the target and predicted responses. Typically,  $R$  and  $Q$  are assumed to be diagonal with  $R$  having the same value  $w_c$  along its diagonal and  $Q$  having the same value  $w_r$  along its diagonal. Minimizing  $J$  with respect to  $u_{h_c}(k)$  and then solving for  $u_{h_c}(k)$  gives

$$u_{h_c}(k) = -(T^T R T + Q)^{\dagger} T^T R \left( -y_T(k) + \mathcal{B}u_p(k-p) + \mathcal{A}y_p(k-p) + \mathcal{D}_p d_p(k-p) + \mathcal{D}_f d_f(k) \right) \quad (14)$$

$h_c \times 1$

as the control sequence to be applied to the system over the next  $h_c$  time steps. However, only the first  $r_c$  values (corresponding to the first future time step)

$$u_c(k) = -\chi^c y_T(k) + \beta^c u_p(k-p) + \alpha^c y_p(k-p) + \delta^c d_p(k-p) + \gamma^c d_f(k) \quad (15)$$

are applied to the  $r_c$  control inputs, the remainder is discarded, and a new control sequence is calculated at the next time step. Equation 15 is the desired control law equation. The target response  $y_T(k)$  is zero for a regulator problem and non-zero for a tracking problem. The coefficient matrices  $\chi^c$ ,  $\alpha^c$ ,  $\beta^c$ ,  $\delta^c$ , and  $\gamma^c$  are the control law gain matrices and have sizes  $r_c \times mh_p$ ,  $r_c \times pm$ ,  $r_c \times pr_c$ ,  $r_c \times pr_d$ , and  $r_c \times rdh_p$ , respectively.

### Selection of Control Model Parameters

An expression for estimating the order of the ARX model that is to be used for SID is given by

$$p \geq \text{ceil} \left( \frac{\text{number of system states} + \text{number of disturbance states}}{m} \right) \quad (16)$$

where *ceil* denotes rounding up the value of the quantity in parentheses to the next higher integer. The number of system states is typically chosen to be twice the number of significant structural modes; the number of disturbance states is set to twice the (estimated) number of frequencies in the disturbance;  $m$  is the number of output measurements. If measurement noise is of concern, the value of  $p$  so computed should be increased to allow for computational poles and zeros to improve system identification in the presence of noise. In practice, simply choosing  $p$  to be about five times the number of significant modes in the system is often adequate. The prediction and control horizons are set according to the relations

$$h_p \geq p \quad h_c \leq h_p \quad (17)$$

By extending the prediction and control horizons to very large values, the GPC solution approaches that of the linear quadratic regulator (LQR). Thus, GPC approximates an optimal controller for large  $h_p$  (ref. 9).

Weighting matrices  $R$  and  $Q$  are used to weight the control effort and to weight the relative importance of the differences between the target and predicted responses, respectively. In practice, the relative values of the weighting matrices play the major role in the optimization process. Therefore, the weighting matrix  $Q$  is often set to an identity matrix. The control weight matrix  $R$  then becomes the only one needed to be tuned to produce an acceptable solution without going unstable. Reducing  $w_c$  increases controller performance but may saturate the actuators or drive the control system unstable.

### Practical Issues

Two issues need to be addressed before applying the GPC method to a real problem: the treatment of external disturbances and basic signal processing guidelines.

## Treatment of External Disturbances

If the external disturbances acting on a system are unknown, the best that can be done is to identify the system in the presence of these disturbances so as to include their effects in the identified OMP. The control law obtained using the OMP with the embedded disturbance information is then used to compute the control inputs. This is the procedure that was employed successfully in the GPC-based active controls testing of the tiltrotor model.

If any of the external disturbances acting on the system are known or can be measured a feedforward loop can be employed in combination with the feedback loop. There are two feedforward terms (e.g., see equation 10): a term involving past values  $d_p$  and a term involving future values  $d_f$ . If only past values are available one simply discards the other term. If future values are also available from an AR prediction model then both terms are retained. If there is correlation in the disturbance signals and the character of those disturbances is not changing significantly with time an AR model can be determined using an initial portion of the disturbance data. This model can then be used to predict the future values needed in equation 15. If the disturbances are changing significantly with time (e.g., due to frequency or amplitude variations, changes in the pattern or type of disturbance, etc) but there is coherence in the signals, an AR model can still be determined. However, for the AR model to adapt to the changing conditions it would have to be updated (ideally at each time step) using some type of recursive least squares algorithm. If there is no coherence in the disturbance signals no predictions of future disturbances are possible and only the term involving past values of the disturbance can be retained. These aspects are addressed in Appendix A.

## Basic Signal Processing Guidelines

Several signal-processing considerations must be taken into account when using either measured data or simulated data in GPC-based active controls work. The measured response time histories must be passed through a low-pass filter with a cut-off frequency  $f_c$  chosen so that the maximum frequency of interest is about 75% of  $f_c$ . Assuming that  $f_c$  is equal to the Nyquist frequency  $f_N$ , the required sampling frequency  $f_s$  should be at least twice this value of  $f_N$  to prevent aliasing. However, if  $f_s$  is made too large the low-frequency modes will be poorly identified due to a loss of frequency resolution. A sampling rate between 2 to 3 times  $f_N$  is generally sufficient. Once the sampling frequency has been selected, the minimum number of data points required for system identification is at least 5-10 cycles of the lowest frequency mode in the measured response time histories. Normalization of the input and output data that is used for identification on the maximum actual or expected values of the data is often helpful numerically.

It should be noted that active controllers are usually designed using a reduced-order mathematical model that includes only the most important subset of modes of a system. The frequency band spanned by the retained system modes sets the effective bandwidth of the resulting reduced-order controller. Such controllers may destabilize higher-order modes of the system due to truncation and spill over effects. The modes having frequencies in the transition region between retained and truncated modes are particularly susceptible. While these aspects of controller design are dealt with only casually below (e.g., through the choice of  $p$ , sampling

frequency, decimation factor, frequency range of interest, filter cutoff frequency, and number of data points used for SID), it is recognized that such considerations often require substantial attention by controls engineers.

## **Results and Discussion**

Results from two types of closed-loop simulations are presented. One uses a mathematical model of a three-degree-of-freedom mass-spring-dashpot system subject to user-specified disturbance force time histories. The other uses gust response data obtained from the wind-tunnel test of the HiLDA wing model. The intent of these simulations is to demonstrate the efficacy of a GPC-based active control system for gust load alleviation and the improvement in performance associated with including a feedforward path if any of the external disturbances are known, measurable, or predictable. The results presented below have been selected primarily with these objectives in mind.

### **Comment on Codes Used for Simulations**

Two MATLAB programs were developed and used for the simulation studies that provided the numerical results for this report. One is an extension of the three-degree-of-freedom (3-DOF) code that was used extensively to develop and evaluate the computational procedures that underlie the GPC software system that was used for the active controls testing of the tiltrotor model. This program treats a simple system with known dynamic properties and user-defined external disturbances. It also lends itself to easy modification should the need arise to address either a what-if question or a computational issue. The other program is new and was written specifically to access and process the data sets that were obtained during the wind-tunnel test of the HiLDA wing model (ref. 6). For that reason, it is tailored to treat that system. Although the programs are considerably different if viewed from a coding perspective, they are based on the same theoretical and computational principles and are therefore equivalent.

### **Numerical Simulations Using 3-DOF Math Model**

The 3-DOF mass-spring-dashpot system used in the 3-DOF simulations is depicted in figure 2 and the corresponding equations of motion are summarized in Appendix B. The model has three masses, three springs, and three dashpots. Disturbance forces  $ud_1$ ,  $ud_2$ , and  $ud_3$  and control forces  $uc_1$ ,  $uc_2$ , and  $uc_3$  act on masses  $m_1$ ,  $m_2$ , and  $m_3$ , respectively. The degrees of freedom  $x_1$ ,  $x_2$ , and  $x_3$  are the absolute displacements of the corresponding masses. For the simulations, the masses were set equal to 1.0 lb-sec<sup>2</sup>/in, the spring rates to 1000 lb/in, and the damping coefficients to 0.01 lb/in/sec. This yields natural frequencies of 2.240, 6.276, and 9.069 Hz and corresponding damping ratios of 7.0367e-005, 1.9716e-004, and 2.8491e-004 for the three natural modes of the system. Disturbances, control forces, and responses (displacements, velocities, or accelerations) can be specified and selected in any combination (see Appendix B). However, for the results to be shown here, controls were imposed at masses 1 and/or 3 (except for one case of three control inputs), disturbances were imposed at masses 1 and/or 2, and accelerations were measured at masses 1 and/or 2. Both steady-state (constant amplitude and frequency) and non-steady-state (varying amplitude and frequency) disturbances were imposed on the system.

The steady-state disturbances (figure 3) were chosen to be sinusoidal with a frequency of 6.276 Hz, which coincides with the second natural frequency of the system. The expressions used to represent these disturbances in the simulations were  $ud_1 = 2*\cos(2*\pi*f*t)$  and  $ud_2 = \sin(2*\pi*f*t)$ . The non-steady-state disturbances had variable and/or discontinuous amplitude and frequency time histories. The first of these was composed of four variable-amplitude, constant-frequency segments (fig. 4a); the other represented a disturbance with increasing frequency and decreasing amplitude (fig. 4b).

The MATLAB function *c2d* was used to convert the continuous-time state-space models of the 3-DOF system (Appendix B) to discrete-time using  $\Delta t = 0.05$  as set below. The resulting discrete-time state-space models, along with their corresponding discretized disturbances, were then used in the MATLAB function *dlsim* to generate the open-loop time histories needed for SID.

The maximum frequency of interest for the 3-DOF system is just over 9 Hz. Based on the signal processing guidelines mentioned earlier, the sampling frequency  $f_s$  was set to 20 Hz ( $\Delta t = 0.05$  sec) and the number of time steps  $\ell$  of input/output data was set to 300. The control horizon  $h_c$  was set equal to the prediction horizon  $h_p$  and  $h_p$  was set equal to the order of the ARX model  $p$ . The value of  $p$  was set to 6, 8, or 10 depending on the control case being considered and the number of disturbances acting on the system. For the cases of feedback-only and feedback with feedforward  $p$  was set to 6. The use of feedback with embedded feedforward requires  $p$  to be increased by (at least) two for each of the dominant frequencies present in the external disturbances acting on the system. This expedient provides the additional degrees of freedom needed to ensure that the effects of the unknown periodic disturbances are embedded in the observer Markov parameters that are computed during system identification. Thus,  $p$  was set to 8 when using the single disturbances in figure 4 and to 10 when using the double disturbances in figure 3. Based on previous experience with the 3-DOF model, the response weights  $w_r$  were set to 1.0 and the control weights  $w_c$  were taken to be equal and set to 0.3. In practice, the response weights  $w_r$  are usually set to unity and  $w_c$  is varied to tune the controller to the nuances of the subject system. Tuning proceeds by initially setting the value of  $w_c$  to a “conservative” value (e.g., 1, as was initially done for the 3-DOF system) and then tracking the value of the objective function  $J$  given in equation 13 as  $w_c$  is incrementally reduced until either a minimum value of  $J$  is identified or the control system actuators become saturated. This process for selecting  $w_c$  is analogous to the familiar procedure for selecting the controller gain in a single-input/single-output system. Previous experience with the 3-DOF model indicates that the selected values are all reasonable but not optimum. No attempt was made to “optimize” (i.e., tune) the parameters  $p$ ,  $h_c$ ,  $h_p$ ,  $w_r$ , and  $w_c$  to the nuances of the system under the different disturbances to elicit the best (lowest) possible closed-loop responses. In the simulations, the loop was closed after 100 time steps (5 sec) when using steady-state disturbances and 20 time steps (1 sec) when using non-steady-state disturbances.

Results are presented below for three types of control cases: (1) feedback only, in which no account is taken of any external disturbances acting on the system during SID and controller design; (2) feedback with embedded feedforward, in which all the disturbances acting on the

system are assumed to be unknown while performing the SID and controller design; and (3) feedback plus feedforward, in which all of the external disturbances acting on the system are assumed to be measurable and are used during the SID and design of the feedforward controller. A second-order AR disturbance model ( $n_d = 2$ ) (see Appendix A) was used for predicting the future disturbances needed by the feedforward controller. This portion of the feedforward controller was adaptive and used RLS with a forgetting factor (ref. 21) of 0.9. Results are presented for both steady-state (constant amplitude and frequency) and non-steady-state (varying amplitude and frequency) disturbances. For ease of discussion, the second control case will be referred to simply as ‘embedded feedforward’ and the third control case will be referred to as ‘explicit feedforward’.

While some of the results shown below indicate the effect on performance of increasing the number of control effectors, there is no discussion of trade-offs between the number of control inputs used and the costs associated with implementation or power requirements. These would be important considerations in any studies aimed at full-scale implementation but are beyond the scope of this report.

## Representative Results

**Steady-State Disturbances:** Representative results obtained from simulations made using the steady-state disturbances shown in figure 3 acting on masses 1 and 2 ( $ud_1$  and  $ud_2$  in fig. 2) are given in figures 5-9. Loop closure (active control on) was taken to occur after five seconds. Figures 5-7 show results for feedback only, embedded feedforward, and explicit feedforward, respectively, for the case in which control is applied at mass 3 ( $uc_3$ ) and feedback is the acceleration of mass 1 ( $\ddot{x}_1$ ). In all three cases, the response was quickly reduced to very small values when the loop was closed and then maintained at those low values thereafter. The closed-loop response levels for embedded feedforward (fig. 6) are essentially the same as those for explicit feedforward (fig. 7), but both are smaller than those for the feedback-only case of figure 5. However, the feedback-only case also produces a considerably reduced response level. This result indicates that ignoring the disturbances during SID may produce an acceptable ARX model for designing a GPC controller for a system. The control inputs for all three cases are nearly the same.

The effect of applying control forces at two masses ( $uc_1$  and  $uc_3$ ) rather than just at one mass ( $uc_3$ ) as in figure 7 is illustrated in figure 8 for explicit feedforward. Comparing these results to those of figure 7 indicates that the use of an additional control force reduced both the closed-loop response and the magnitudes of the required control forces below the values associated with a single control, as might be expected.

Figure 9 shows results for explicit feedforward for the case of control inputs at masses 1 and 3 ( $uc_1$  and  $uc_3$ ) as in figure 8 but with acceleration outputs at both masses 1 and 2 ( $\ddot{x}_1$  and  $\ddot{x}_2$ ). Both responses are very quickly quashed after the loop is closed. There is a slight increase in the magnitudes of the required control forces because two responses are now being worked by the controller rather than just one as in figure 8.

**Non-Steady-State Disturbances:** Typical results obtained from simulations made using the piecewise varying frequency and amplitude disturbance shown in figure 4a acting on mass 2 ( $ud_2$ ) and taking the feedback to be the acceleration of mass 1 ( $\ddot{x}_1$ ) are given in figures 10-14 for cases involving one to three control inputs. Loop closure (active control on) was imposed after one second. All responses were reduced to varying extents depending on the number of control inputs. Figures 10 and 11 show results using embedded feedforward and explicit feedforward, respectively, for the case in which control is applied at mass 3 ( $uc_3$ ). The closed-loop response using explicit feedforward is slightly better than for embedded feedforward while the magnitudes of the control inputs are either slightly larger, smaller or about the same depending on the segment of the disturbance that is active.

Figures 12 and 13 show results for embedded feedforward and explicit feedforward, respectively, for the case of control inputs at masses 1 and 3 ( $uc_1$  and  $uc_3$ ). The closed-loop response is only slightly better using explicit feedforward (fig. 13) than embedded feedforward (fig. 12) while the required control inputs are about the same. Increasing the number of control inputs from one to two produces lower responses (compare figure 12 to figure 10 and figure 13 to figure 11).

Figure 14 shows results using explicit feedforward for the case in which control inputs are at masses 1, 2 and 3 ( $uc_1$ ,  $uc_2$  and  $uc_3$ ). The closed-loop responses and controls in this case are improved relative to the two-control-input results shown in figure 13, as should be expected.

Results from simulations made using the disturbance shown in figure 4b acting at mass 2 ( $ud_2$ ) and taking the feedback to be the acceleration of mass 1 ( $\ddot{x}_1$ ) are given in figures 15-17. Loop closure was taken to occur after one second. Figures 15 and 16 show results for embedded feedforward and explicit feedforward, respectively, for the case of a control input at mass 3 ( $uc_3$ ). The response is reduced in both cases but is decidedly better using explicit feedforward with adaptive identification of the disturbance. Control inputs for the latter are slightly larger during the early (lower frequency) portion of the disturbance but lower during the latter (higher frequency) portion of the disturbance. Figure 17 shows results using explicit feedforward for the case of control inputs at masses 1 and 3 ( $uc_1$  and  $uc_3$ ). The closed-loop response in this case is lower than that for the case of one control in figure 16, and control inputs are slightly smaller during the early (lower frequency) portion of the disturbance but generally the same or larger during the latter (higher frequency) portion.

**Summary of Observations:** Taken as a whole, the 3-DOF simulations indicate that GPC-based controllers are able to significantly reduce acceleration responses under a variety of imposed disturbance conditions and to do so very quickly after closing the loop. For the cases involving steady-state disturbances (figs. 5-9), the lightly-damped system was being excited at one of its natural frequencies and the open-loop responses are all diverging with time. Thus, the percentage reduction in response after closing the loop in these cases depends on when the loop is closed as the magnitude of the steady-state closed-loop response is essentially independent of loop closure time. For figures 5-8 (2 disturbances, 1 output, 1 control) the amplitude of the open-loop response at time of closure (5 sec) is about 70 in/sec<sup>2</sup>. With respect to this value, the reduction in acceleration responses ranged from about 90% to essentially 100%. For the case of figure 9 (2 disturbances, 2 outputs, 2 controls) both  $\ddot{x}_1$  and  $\ddot{x}_2$  were effectively reduced to zero.

The results in figures 10-17 are for disturbances with varying frequency and amplitude and can't be quantified with a single number because the percentage reduction in response varies with the frequency and amplitude of the disturbance. However, depending on the position in the time history, the reduction varies from about 50% to essentially 100%. Given that the maximum values of the disturbance forces vary from one to two pounds in magnitude the required steady-state control forces in figures 5-17, which range from about 0.2 lbs to 2 lbs, are considered reasonable.

With respect to the effects on performance associated with varying the number of control inputs and response outputs, the 3-DOF simulation results indicate that increasing the number of controls  $r_c$  for a fixed number of outputs  $m$  improves performance (both responses and control inputs are lower). Conversely, increasing the number of outputs  $m$  for fixed  $r_c$  increases the required control inputs slightly but still quells all the responses. If both  $m$  and  $r_c$  are increased simultaneously, all the responses are reduced with only a slight increase in the required control inputs. As mentioned earlier, no attempt was made to tune any of the GPC parameters to the nuances of the system under the different disturbances to obtain the best (lowest) possible closed-loop responses. However, the results (not shown) of some limited parametric variations indicate that increasing the order  $p$  of the ARX model and/or reducing the magnitude of the control weight  $w_c$  can improve the performance of the controller in all of the 3-DOF simulations presented above.

### **Numerical Simulations Using Data from Wind-Tunnel Test of HiLDA Wing Model**

The HiLDA wing model, as mounted in the Langley Transonic Dynamics Tunnel (TDT), is shown in figure 18. The model has four trailing-edge control surfaces that span the lifting portion of the wing and one leading-edge control surface located near the wing tip. A simulated vertical gust field was applied to the test section flow in the form of a sinusoidal oscillation of the flow direction. This oscillating flow was generated by an airstream oscillator system consisting of a biplane arrangement of vanes located on the side walls of the tunnel about 70 feet upstream from the model (fig. 19). The gust-induced flow angle was measured by a vane-type flow direction transmitter that was mounted on the top of a seven-foot high post attached to the tunnel floor six feet ahead of the model (fig. 18). A schematic of the wing planform is depicted in figure 20, which shows the arrangement of the five control surfaces that were used as control effectors and the locations of the three strain gage sensors that provided the feedback response time histories for the simulations. The reader is referred to reference 6 for a description of the model.

### **Test Conditions**

The data used in the simulations presented below were obtained during a run in the TDT heavy gas (R134a) test medium at a dynamic pressure of 51 lb/ft<sup>2</sup>. The corresponding Mach number and velocity were 0.25 and 138 ft/sec, respectively. Sinusoidal vertical gust excitations were induced in the test section by the vertical components of the tip vortices shed from the oscillating biplane vanes. The amplitude of oscillation of the airstream oscillator was set to  $\pm 6$  degrees. This amplitude was sufficient to produce gust angles as large as one degree at the location of the model at the lower airspeed/frequency combinations. The airstream oscillator

excitation signatures consisted of constant frequency dwells at the natural frequencies of the first and second vertical bending modes ( $f_{1v} \approx 2$  Hz,  $f_{2v} \approx 8$  Hz), and frequency sweeps from 0.5 Hz to 10 Hz in 30 seconds. For SID purposes random excitations of the five control surfaces were imposed simultaneously and consisted of uncorrelated, normally-distributed random numbers with mean zero and a variance chosen to limit the oscillation angles of the control surfaces to about  $\pm 2$  degrees.

## Test Procedures

The SID data for the case in which the gust excitation frequency is held constant were obtained as follows: (1) Set tunnel dynamic pressure to the desired value; (2) Set the frequency of the airstream oscillator to its desired value; (3) Impose a random excitation on each of the five control surfaces; and (4) Record the resulting input and output time histories for 35 seconds. For the case in which the gust frequency is swept from a low value to a high value the procedure was: (1) Set tunnel dynamic pressure to the desired value; (2) Set the frequency of the airstream oscillator to its starting value of 0.5 Hz; (3) Impose a random excitation on each of the five control surfaces; and (4) Sweep the gust frequency continuously from 0.5 Hz to 10 Hz in 30 seconds while recording the resulting input and output time histories.

## Simulation Conditions and Parameter Settings

The original data were taken using a sampling rate of 500 Hz and recorded for 35 seconds, yielding data records consisting of 17500 time samples. To exclude transients, the data outside time samples 1000 and 15000 were discarded. Since the wing modes to be controlled were less than 15 Hz, the truncated data were then decimated by a factor of 10 using the MATLAB command *decimate*, resulting in data representing a sampling rate of 50 Hz. Finally, the mean value of each measurement was subtracted from its time history.

The conditioned input-output data were used to identify the plant and to develop the controller. SID was accomplished using the command *arx\_ud* from the predictive control toolbox. The outputs from strain-gage sensors SBI2, SBY, and STI2 shown in figure 20 were selected as the quantities to be minimized collectively ( $m = 3$ ). All five control inputs, CTL1, CTL2, CTL3, CTL4, and CTL5, were utilized simultaneously as control effectors ( $r_c = 5$ ). The feedforward signal was taken from the flow direction transmitter.

System identification returned the ARX parameters of equation 1. The control law gain matrices in equation 15 were then obtained by processing the ARX parameters according to the computational methods described earlier in this report. The ARX parameters were used for the time history simulation of both the open- and closed-loop plant, as well as for the design of both the embedded feedforward and explicit feedforward controllers. Controller design was accomplished using a modified version of the m-file *msop* from the predictive control toolbox. The same controller was used for embedded feedforward and explicit feedforward simulations, the difference being that in the former case the feedforward controller path was not utilized. For closed-loop simulations employing embedded feedforward, only the terms involving the past control inputs  $u_p$  and feedback outputs  $y_p$  in equation 15 were used to compute the control inputs  $u_c$ . For cases employing explicit feedforward, all four terms were used. In order to use the  $d_f$

term of equation 15, some estimate must be made of future disturbance inputs given the history of past disturbance measurements. As discussed earlier, depending on the character of the disturbances acting on the system, either an adaptive or a non-adaptive AR model can be used to predict future disturbances. Here, an adaptive 6<sup>th</sup> order AR model was chosen to predict the future disturbances. A recursive least squares procedure with a forgetting factor of 0.97 was used to update the AR model parameters every time step, thus allowing for enhanced tracking of the swept sine gust.

A comment is in order here regarding some additional data processing that was necessary to allow a proper comparison of measured open-loop time histories with simulated closed-loop time histories. The desired open-loop time histories (quiescent controls during each of the three gust-excitation conditions) were not among the data sets collected during the test. The closest set of data was that taken for SID wherein the five control surfaces were randomly excited during gust excitation. Fortunately, it is possible to compute the desired open-loop responses using that data set. Essentially, one first performs an SID using as input the random excitations of the control surfaces and the gust vane measurements. This yields the OMP  $\alpha_i$ ,  $\beta_i$  and  $\gamma_i$  of equation 1. One then performs a time-history simulation for  $y(k)$  using equation 1 but retaining only the  $\alpha_i$  and  $\gamma_i$  terms on the right-hand-side and using for  $d$  the same set of gust vane measurements used for the SID. The resulting time histories are the desired open-loop time histories. To maintain consistency, the same set of gust vane measurements is added to the plant response  $y$  at each time step during the closed-loop simulations.

The system model identified as described above was used in both the open-loop and closed-loop simulations for the cases of both embedded feedforward and explicit feedforward controllers. The control inputs  $u_c(k)$  were set to zero for the open-loop simulation. For the closed-loop simulation the control signal computed using equation 15 was used. The control input for embedded feedforward used only the past outputs  $y_p$  and past control inputs  $u_p$ ; no use was made of the past and future feedforward terms ( $d_p$  and  $d_f$ ). For the explicit feedforward controller the computed control signal  $u_c(k)$  was obtained using all four terms on the right-hand-side of equation 15: the past outputs, past control inputs, past measured feedforward values, and future predicted feedforward values. The same weights that were used for the 3-DOF simulations ( $w_r=1$  and  $w_c=0.3$ ) were tried for the HiLDA wing data and found to be acceptable. The value of  $p$  was estimated using equation 16 and set to 10. Its value was not varied with controller type as for the 3-DOF model. The controller was turned on five seconds into the simulations.

## Representative Results

Figures 21 through 62 show simulated open- and closed-loop responses of wing root vertical bending (SBI2), fore-and-aft bending (SBY), and torsion (STI2) to sinusoidal vertical gust excitation held constant at the natural frequencies of the first and second vertical bending modes and while sweeping the frequency of the gust from 0.5 Hz to 10 Hz. Bending and torsion moment response time histories, power spectral densities of bending and torsion moment time histories, and control angle input time histories are shown for each of the three gust excitation conditions for two control cases: (1) Feedback with embedded feedforward; and (2) Feedback with explicit feedforward and using an adaptive AR model for predicting the future disturbances.

**Feedback with Embedded Feedforward:** Figures 21-27 indicate controller performance in reducing wing root moments due to gust excitation at the natural frequency of the first vertical bending mode (2 Hz). The SBI2 closed-loop time history (fig. 21) shows a dramatic reduction of that modal response almost immediately after the controller is turned on. The corresponding SBY and STI2 closed-loop time histories (figs. 22-23) are also significantly, and promptly, reduced. The PSD plots (figs. 24-26) indicate that the primary effect has been to reduce the response at the frequency of excitation (the first mode), as would be expected. However, the closed-loop spectra are not flat indicating that there is residual correlation in the sensor signals. It may not be possible to remove all correlation in regulated systems due to stability issues, the presence of unobservable and/or uncontrollable modes, or limits on actuator authority. Based on experience with GPC applied to other systems, it is known that tuning of the GPC parameters (horizons, control penalty, order) oftentimes leads to enhanced performance. However, no adjustments were made in these parameters to optimize performance in the results shown here or below. Figure 27 shows the commanded control deflection angles to be small once transients decay. In a physical control system, the overshoot occurring at loop closure would be suppressed by low-pass filtering the control signal and/or placing upper and lower bounds on the allowable control amplitudes in both the hardware and software. The roll-off occurring in the magnitudes of the PSD curves at frequencies above about 20 Hz is due to the filtering action of the function *decimate* that was used to decimate the original wind-tunnel data.

Figures 28-34 summarize controller performance due to gust excitation of the wing at its second vertical bending natural frequency (8 Hz). The response time histories (figs. 28-30) show a dramatic and essentially immediate drop in amplitude once the control is applied. The PSD plots (figs. 31-33) show a relatively flat controlled spectrum. Again, the primary effect has been to reduce the response at the frequency of excitation (the second mode), as would be expected. In this case the response in that mode is virtually eliminated. Additionally, the SBY responses at 5 Hz (the first fore-and-aft bending mode) and at 16 Hz are greatly reduced. Figure 34 shows the control effort to be small once transients decay. In practice, the overshoot occurring at 5 seconds would be suppressed by low pass filtering the control signal and/or placing upper and lower bounds on the allowable control amplitudes.

Figures 35-41 show controller performance for the case in which the gust frequency is swept from 0.5 Hz to 10 Hz. In comparison to the constant-frequency gust excitation cases of figures 21-34, controller performance is only fair. This is due to the fact that SID in the presence of a varying-frequency gust leads to an internal (i.e., embedded) disturbance model that is effectively an average model over the bandwidth of the gust. This leads to a controller that can not effectively reduce the responses at all the frequencies contained in the gust as in the constant-frequency gust cases. One possible solution to this problem is to use a GPC controller in which all the coefficient matrices  $\chi^c$ ,  $\alpha^c$ ,  $\beta^c$ ,  $\delta^c$ , and  $\gamma^c$  in equation 15 periodically adapt (see, for example, ref. 15). Figure 41 shows that the control deflection angles in this case are large compared to those required for a constant-frequency gust excitation. It is thought that this is because the responses to the disturbance input (gust vane measurement added to  $y$ ) were larger than the responses to the random disturbances input by the control surfaces during SID. There was thus a greater correlation in the gust vane disturbance input-to-output path than in the control input-to-output path. A more accurate mapping from control input  $u$  to system output  $y$

would produce a better model of the plant. This could be achieved by either increasing the amplitude of the random noise applied to the control inputs for SID or reducing the level of the disturbance (gust vane measurement added to  $y$ ) applied to the system during SID.

**Feedback with Explicit Feedforward:** Figures 42-48 show the performance of the explicit feedforward controller for the case in which the gust frequency is set to that of the first vertical bending mode of the model. Recursive least squares is employed to update the coefficients in the AR model used to estimate the future values of the gust disturbance  $d_f$  given the past disturbance values  $d_p$ , as described in Appendix A. In comparison to the embedded feedforward controller (figs. 21-27), the explicit feedforward controller exhibits better performance as can be seen by comparing time histories, PSDs, and required control angles. The steady-state control angles are all small after the transients have decayed. The improved performance is due to the incorporation of the measured past disturbance values  $d_p$  into the controller as well as the ability of the future component of the feedforward path to tune itself to the changing conditions at each time step, thereby providing improved estimates of future disturbance values  $d_f$ .

Figures 49-55 are for the case of explicit feedforward with a gust frequency set to that of the second vertical bending mode of the model. The adaptive part of the controller is the matrix  $D_{fp}$  in equation A4 that is used to predict the future disturbance values  $d_f(k)$  needed in the last term in equation 15. Enhanced performance over the embedded feedforward case is observed as it was for the first vertical bending mode. The control angles are again all small once the transients decay. It is of interest to note that the closed-loop spectra (figs. 53-55) are effectively flat, indicating that the controller is approximately optimal.

Figures 56-62 show performance of the explicit feedforward controller for the case in which the gust frequency is swept from 0.5 Hz to 10 Hz. Improvement over the performance of the embedded feedforward controller (figs. 35-41) is due to the incorporation of a feedforward path (the last two terms in eq. 15) and the ability of the explicit feedforward component (the last term in eq. 15) to track changes in the gust frequency. The closed-loop spectra (figs. 60-62) are reasonably flat, indicating that the controller is near optimal. The required control angles are quite large compared to that required for quelling the responses for constant-frequency gust excitations. As discussed earlier in the case of the embedded feedforward controller, this may be due to the system identification being compromised by the magnitude of the disturbance signal relative to the noise input on the control channels during identification. Again, it is suspected that if the controller were fully adaptive ( $\alpha^c$ ,  $\beta^c$ ,  $\delta^c$ , and  $\gamma^c$  in equation 15 all adapt at each time step) performance would be much better and require much smaller control angles.

**Summary of Observations:** Taken as a whole, the simulated closed-loop behavior of the HiLDA wing model during constant- and swept-frequency vertical gust excitation indicates that GPC-based controllers are able to significantly reduce wing bending and torsion moments and to do so rapidly after closing the loop. Tables 1 and 2 summarize the overall factors by which the SBI2, SBY, and STI2 wing root moments were reduced for each of the three gusts for the cases of embedded feedforward and explicit feedforward, respectively. For the case of embedded feedforward (table 1), the reductions range from a factor of four to as high as 667, depending on whether the excitation is from a constant- or swept-frequency gust and on the direction of the response. For the case of explicit feedforward (table 2), the reductions range from a factor of

four to as high as 1000, again depending on whether the excitation is from a constant- or swept-frequency gust and on the direction of the response. The control angles required to effect these reductions ranged from one to three degrees for fixed-frequency gust excitations and from 10 to 20 degrees for swept-frequency gusts. Viewed as a whole, these results are decidedly positive in regard to establishing the credibility of GPC as a serious candidate approach for active GLA. Additional wind-tunnel testing of the HiLDA wing model is planned to provide additional validation of the method.

## **Concluding Remarks**

The results of numerical simulations aimed at assessing and evaluating the efficacy of a predictive control method known as Generalized Predictive Control (GPC) for active gust load alleviation (GLA) using trailing- and leading-edge control surfaces have been summarized. GPC is a linear, time-invariant, multi-input/multi-output predictive control method that uses an AutoRegressive with Exogenous input (ARX) model to describe the input-output relationship of the system. The coefficient matrices of the ARX equation are determined using system identification techniques. The input-output equation is used to form a multi-step output prediction equation over a finite prediction horizon. The control to be imposed at the next time step is determined by minimizing the deviation of the predicted controlled plant outputs from the desired (or target) outputs, subject to a penalty on control effort. The method lends itself to an implementation that allows all computations to be done on-line and in real time. Following a qualitative discussion of the essential features of GPC, the equations underlying the method were presented and discussed, including system identification, calculation of control law matrices, and calculation of the commands applied to the control effectors. Both embedded and explicit feedforward paths for incorporation of disturbance effects were addressed.

Representative results from two types of simulations were presented. The first used a three-degree-of-freedom mathematical model of a mass-spring-dashpot system subject to a variety of user-defined external disturbances. The second used open-loop data obtained in a wind-tunnel while subjecting a wing model to constant-frequency and swept-frequency sinusoidal vertical gust excitations. Closed-loop behavior of the model was simulated in post-test calculations. Results obtained from these simulations have been decidedly positive. In particular, the results of all the closed-loop simulations conducted for the wing model showed reductions in wing root moments ranging from factors of four to as much as 1000, depending on whether the excitation is from a constant- or swept-frequency gust and on the direction of the response. The control angles required to achieve these reductions ranged from one to three degrees for fixed-frequency gust excitations and from 10 to 20 degrees for swept-frequency gusts. The GPC-based controller was evaluated for both embedded feedforward and explicit feedforward modes of operation. The effectiveness of the explicit feedforward controller using an adaptive AutoRegressive (AR) model for predicting future disturbances was particularly notable, both in improving performance and in tracking the variable disturbance frequency.

Based on the results of these studies, it appears that GPC is a strong candidate approach for active GLA and warrants further investigation in the subject area. Additional wind-tunnel testing of the HiLDA wing model is planned to provide additional validation of the method.

## Appendix A

### Treatment of Measurable Coherent Disturbances

If the disturbance is measurable and coherent, an AutoRegressive (AR) model of the disturbance giving the disturbance at a future time step  $k$  can be written in the form

$$d(k) = \eta_1 d(k-1) + \eta_2 d(k-2) + \dots + \eta_{n_d} d(k-n_d) \quad (\text{A1})$$

where the coefficient matrices  $\eta_i$  are  $r_d \times r_d$ , the disturbance vectors  $d$  are  $r_d \times 1$ ,  $r_d$  is the number of disturbances, and  $n_d$  is the order of the AR model. The coefficient matrices  $\eta_i$  in the model can be determined using established system identification techniques. The disturbance  $d(k+j)$  at an arbitrary future time step  $k+j$  can be written as

$$d(k+j) = \eta_1 d(k+j-1) + \eta_2 d(k+j-2) + \dots + \eta_{n_d} d(k+j-n_d) \quad (\text{A2})$$

Letting  $j$  range over the set of values 0 to  $h_p-1$  one obtains the set of equations

$$\begin{aligned} d(k) &= \eta_1 d(k-1) + \eta_2 d(k-2) + \dots + \eta_{n_d} d(k-n_d) \\ d(k+1) &= \eta_1 d(k) + \eta_2 d(k-1) + \dots + \eta_{n_d} d(k-n_d+1) \\ d(k+2) &= \eta_1 d(k+1) + \eta_2 d(k) + \dots + \eta_{n_d} d(k-n_d+2) \\ d(k+3) &= \eta_1 d(k+2) + \eta_2 d(k+1) + \eta_3 d(k) + \dots + \eta_{n_d} d(k-n_d+3) \\ &\vdots \\ d(k+h_p-1) &= \eta_1 d(k+h_p-2) + \eta_2 d(k+h_p-3) + \dots + \eta_{n_d} d(k+h_p-n_d-1) \end{aligned} \quad (\text{A3})$$

The first equation in this set is the AR equation given in (A1) and succeeding equations are given using previously computed future disturbances (indicated in color) and measured past disturbances according to the pattern shown. The shifting pattern of the computations indicated in these equations is easily implemented in MATLAB. The results of these shifting calculations can be assembled into a matrix  $D_{fp}$  relating future disturbances to past disturbances according to the equation

$$\begin{aligned} \{d_f(k)\} &= [D_{fp}] \{d_p(k-p)\} \\ h_p r_d \times 1 & \quad h_p r_d \times p r_d \quad p r_d \times 1 \end{aligned} \quad (\text{A4})$$

and the term  $D_f d_f(k)$  in equation 10 can be replaced by  $D_f D_{fp} d_p(k-p)$ .

## Batch Identification of Disturbance Models

Comparisons of several imposed/measured disturbance time histories with those predicted using a non-adaptive AR model are summarized in figures A1-A5. The AR model was identified using a small block of “measured” disturbance data. These results are intended to provide an indication of the ability of AR models to adequately represent correlated disturbances for GPC-based active control systems.

The imposed disturbance time history used for figures A1 and A2 is composed of four equal-length time segments, each containing 100 data points, for a total time period of 20 seconds ( $4 \times 100 \times 0.05 = 20$  sec, where  $\Delta t = 0.05$  sec). Each segment has a different amplitude and frequency. The predictions in figure A1 were based on a model that was identified using only the first 50 data points (first  $50 \times 0.05 = 2.5$  sec of data) while the predictions in figure A2 were based on a model that used all 400 data points. A 6<sup>th</sup> order (six-term) AR model ( $n_d = 6$ ) was assumed for both. These results suggest that a disturbance that has considerable variation in its amplitude and/or frequency can be represented rather well by a low-order model based on a single identification using a modest-length block of data if there is correlation in the disturbance. This appears to be so even if there are abrupt changes in the character of the disturbance (and hence in the coefficient matrices  $\eta_i$  in equation A1).

Figures A3-A5 show comparisons of gust angles measured during the HiLDA test at a dynamic pressure of  $51 \text{ lb/ft}^2$  with predictions obtained using a six-term AR model of the disturbance. The data were obtained at a sampling rate of 500 Hz but were decimated by a factor of ten to reduce the effective sampling rate to 50 Hz. Hence, the effective sampling time is  $\Delta t = 0.02$  sec. The decimated time history contained 1300 points. The first 500 data points (first  $500 \times 0.02 = 10$  sec) of this decimated time history were used to identify the coefficient matrices  $\eta_i$  of the AR disturbance model. Figure A3 shows the measured versus predicted time histories for the case in which the gust frequency was held constant near the first vertical bending mode (about 2 Hz). Similar results for a constant-frequency excitation near the second vertical bending mode (about 8 Hz) are given in figure A4. Figure A5 is for the case in which the gust frequency was swept from 0 to 10 Hz in 30 seconds. In spite of the fact that the gusts are not pure sinusoids and are contaminated by higher harmonics and noise, there appears to be sufficient coherence in the signals to allow use of non-adaptive methods to identify disturbance models that produce reasonable results, particularly at the lower frequencies.

## Adaptive Identification of Disturbance Models

Sometimes it is necessary to update the model of a system or a disturbance on-line and in real time while a system is in operation. Methods using models that are adjusted on-line using measured input/output data up to the current time are called adaptive. To be adaptive in real time requires that the measurements obtained at any time point can be processed during one sampling period. In such instances, recourse must be made to recursive identification techniques, which process data sequentially as they become available. A variety of recursive estimation methods are described in the literature (see, for example, refs. 11 and 21). Among these, the classical

recursive least squares (RLS) method is probably the most popular and simplest. For models whose assumed order is relatively small (such as the disturbance models of interest here), it is the method of choice. However, there are several fast versions of the method available that would be better suited to large models.

Adaptive identification of a disturbance model would update the  $r_d \times r_d$  coefficient matrices  $\eta_i$  in equation A1 at each time step. This updated model would then be used at each time step to compute the vector  $d_f(k)$  in equation A4 and then  $d_f(k)$  used in equations 10, 11, 12, 14, and 15 as appropriate.

Although the results of figures A1-A5 indicate that a non-adaptive identification scheme may be adequate for a wide range of disturbance time histories, there could be times when an adaptive scheme may prove advantageous or necessary. Figures A6-A9 show comparisons of several imposed and measured disturbance time histories with those predicted using an AR model of the disturbance that is updated at each time step using the classical recursive least squares technique. Figures A6 and A7 show results using 2-term and 6-term AR models, respectively. The imposed disturbance time history used is the same one that was employed in figures A1 and A2. Increasing the order of the AR model gives a predicted disturbance that is in better agreement with the imposed disturbance, except when transitioning from one type of disturbance to another where the differences increase away from transition points.

Figures A8 and A9 show results for the case of random disturbances using 6-term and 16-term AR models, respectively. No agreement is evident (or should be expected) because there is no correlation in random signals.

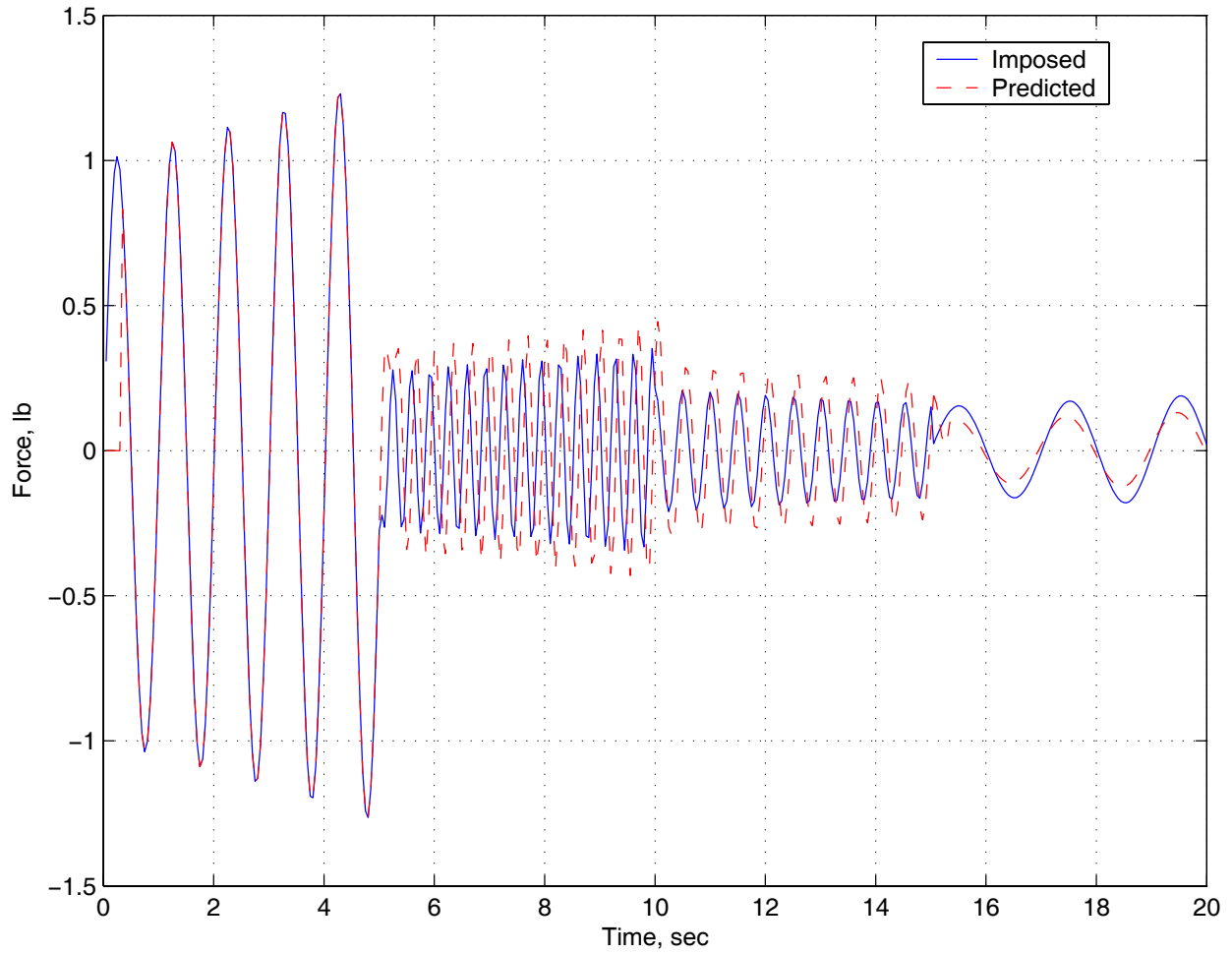


Figure A1.- Imposed versus predicted disturbance time histories using a 6-term AR model identified using the first 50 data points (first 2.5 sec of data).

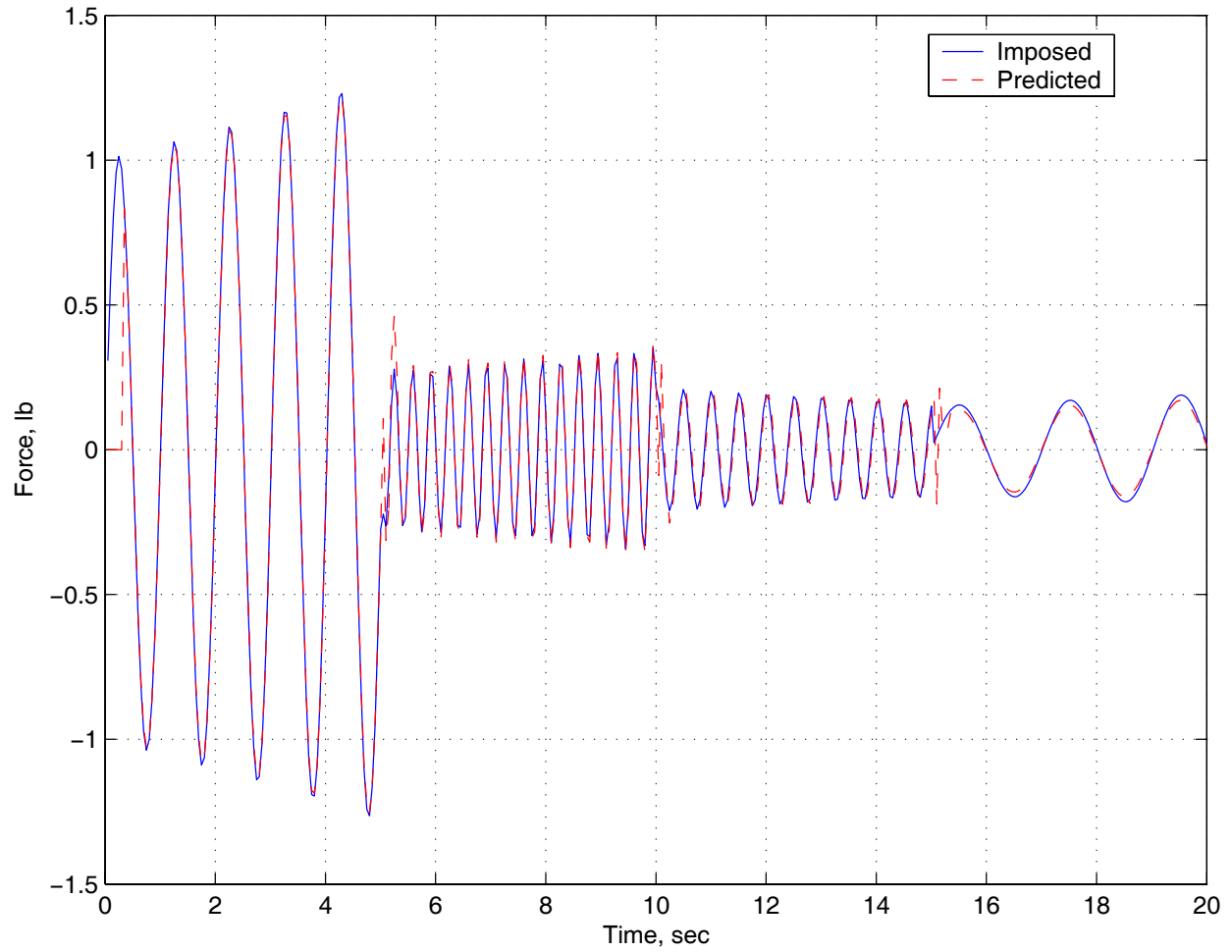
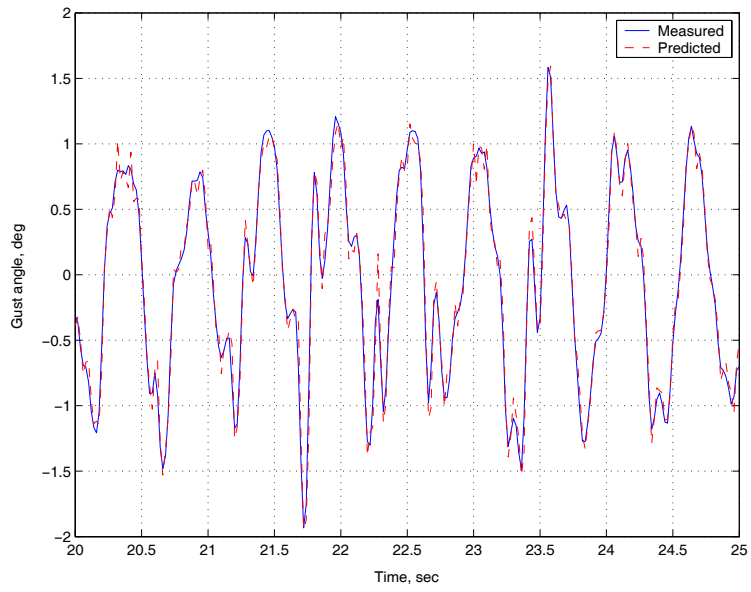
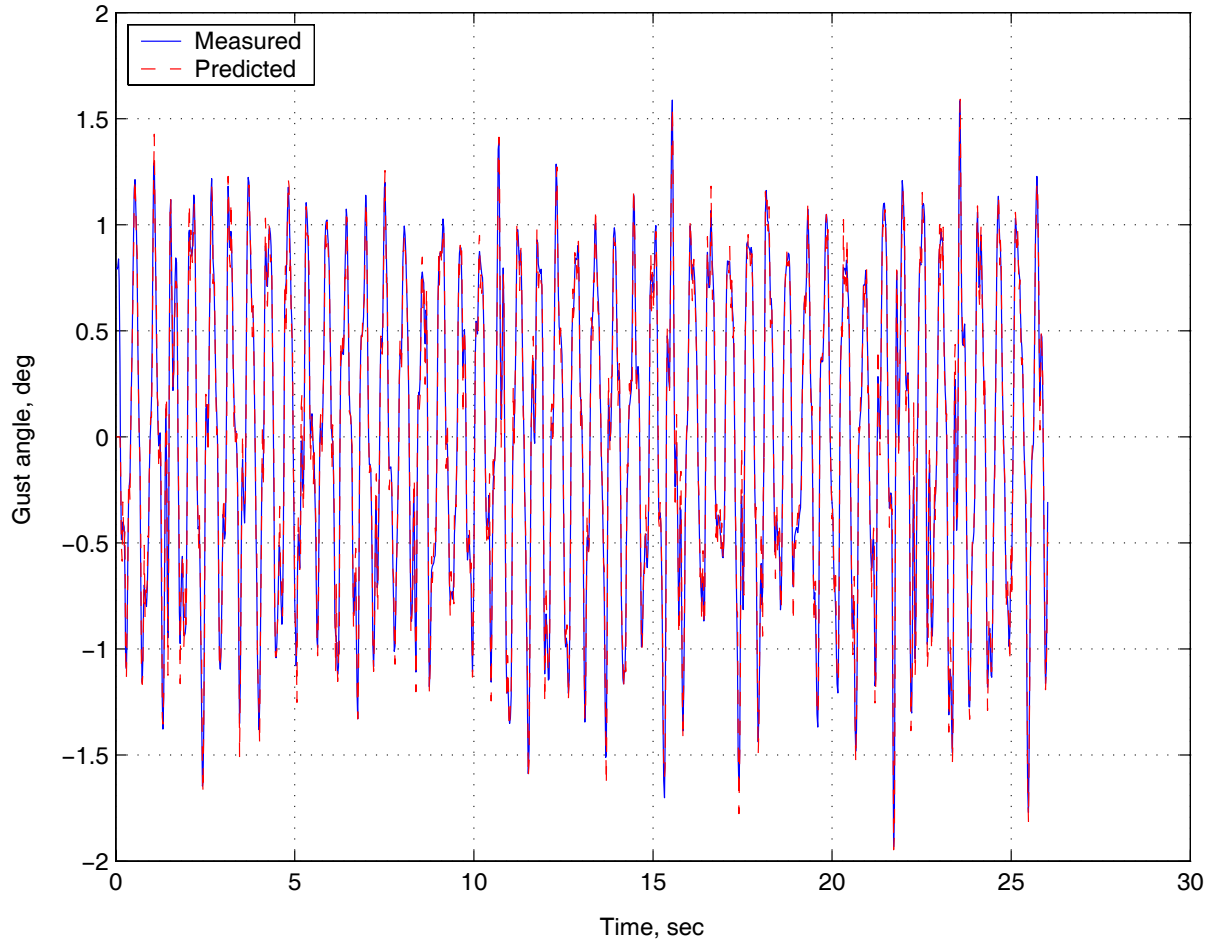


Figure A2.- Imposed versus predicted disturbance time histories using a 6-term AR model identified using all 400 data points.



Expanded view of curves between 20 and 25 sec

Figure A3.- Measured versus predicted gust time histories using a 6-term AR model identified using the first 500 data points (out of 1300) from HiLDA wing test. Airstream was excited at 2 Hz.

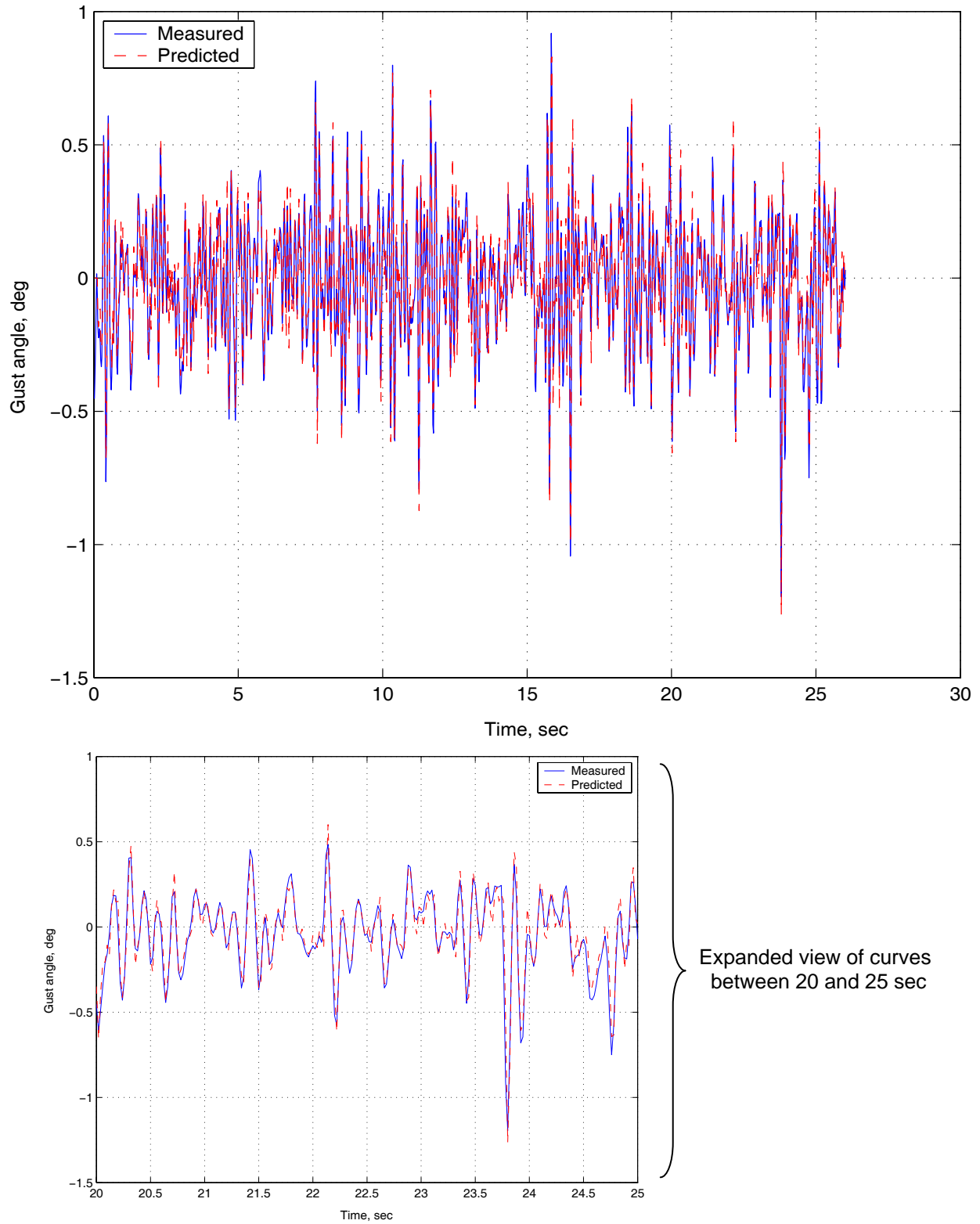


Figure A4.- Measured versus predicted gust time histories using a 6-term AR model identified using the first 500 data points (out of 1300) from HiLDA wing test. Airstream was excited at 8 Hz.

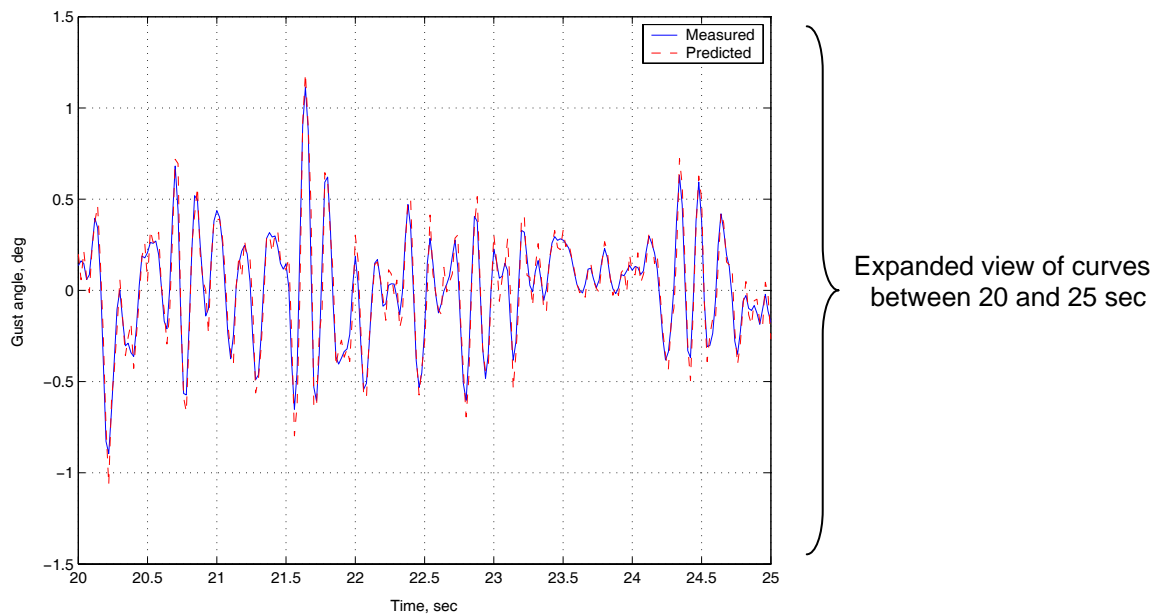
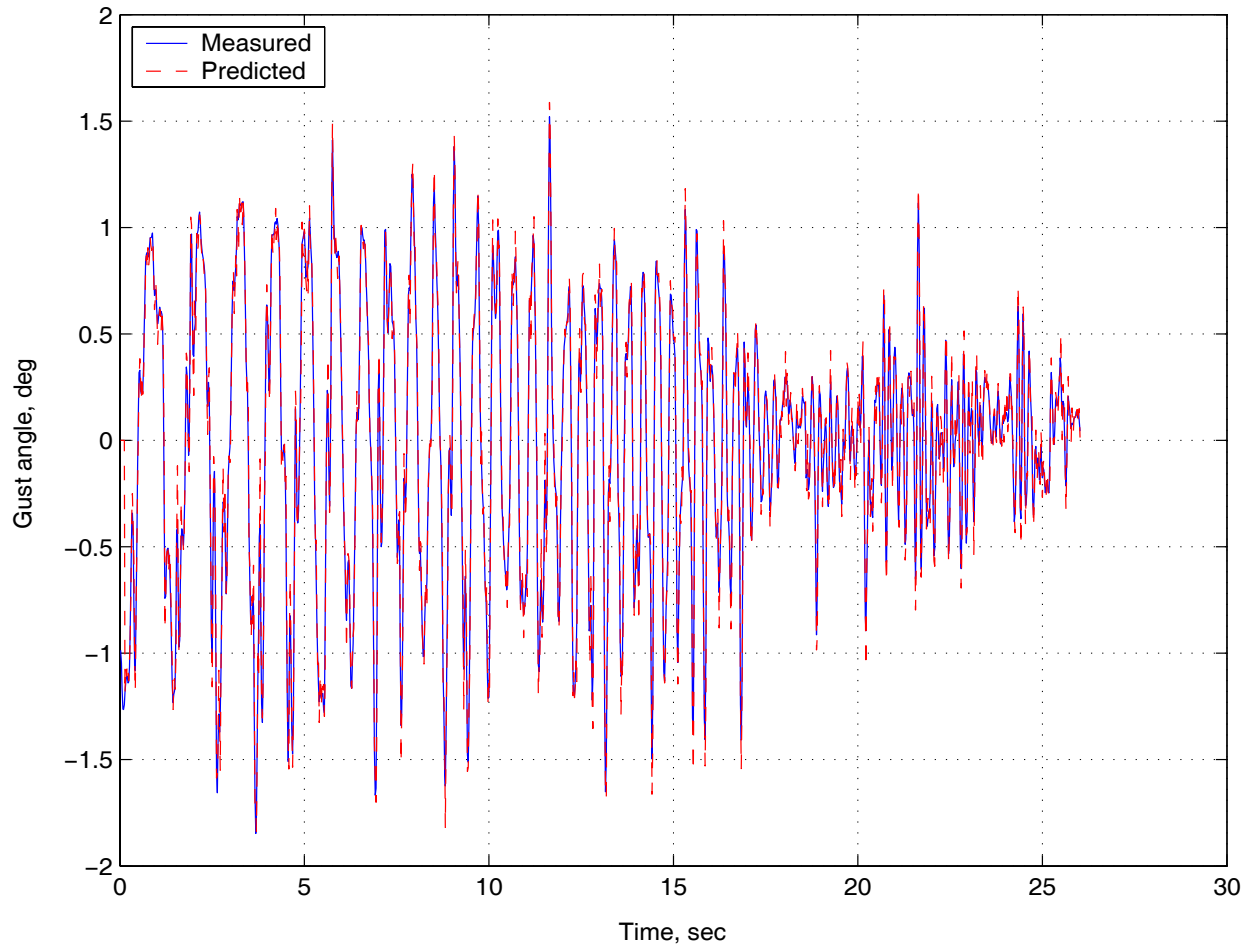


Figure A5.- Measured versus predicted gust time histories using a 6-term AR model obtained using the first 500 data points (out of 1300) from HiLDA wing test. Airstream was excited by sweeping gust frequency from 0.5 to 10 Hz.

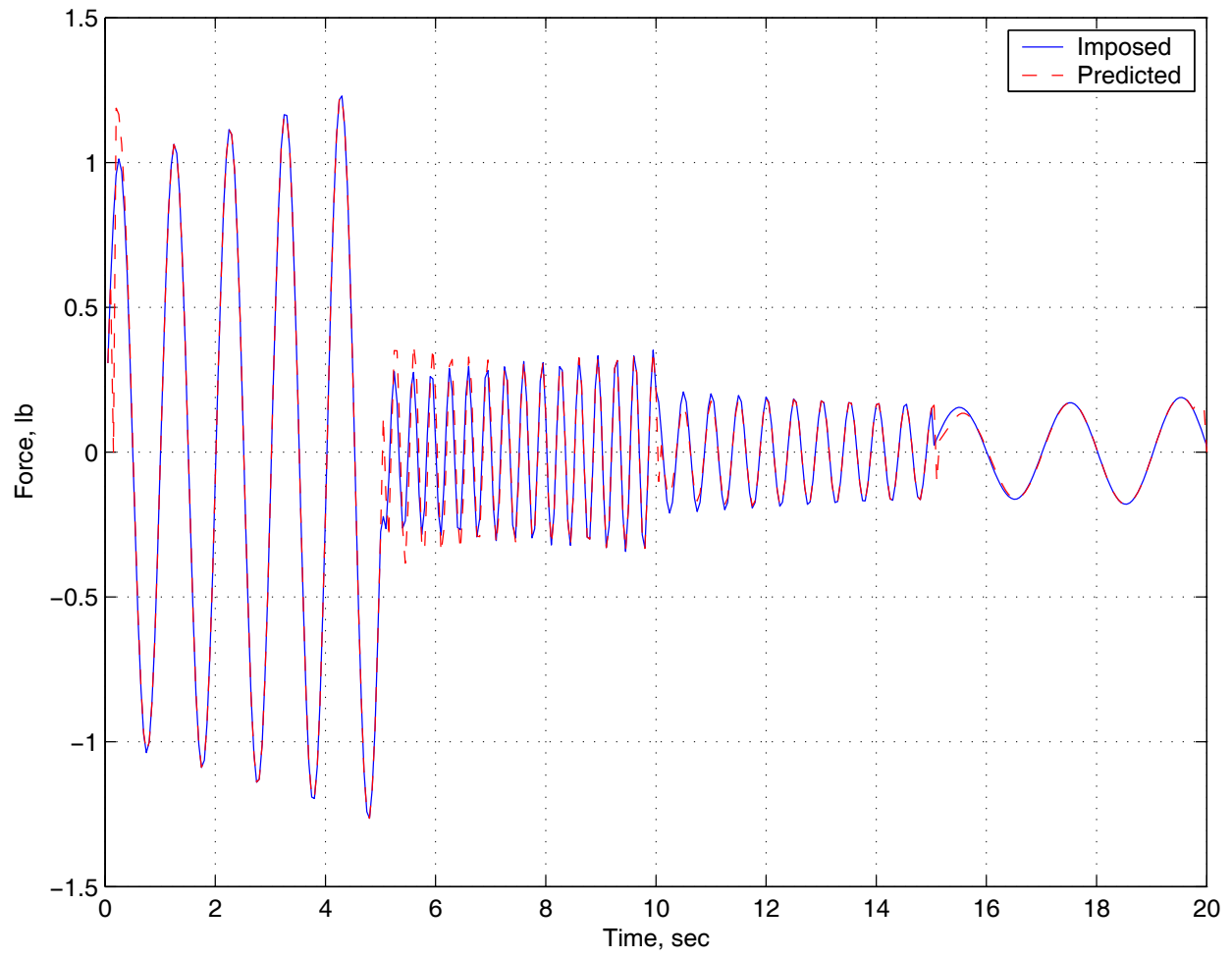


Figure A6.- Imposed versus predicted disturbance time histories using a 2-term AR model updated at each time step using RLS.

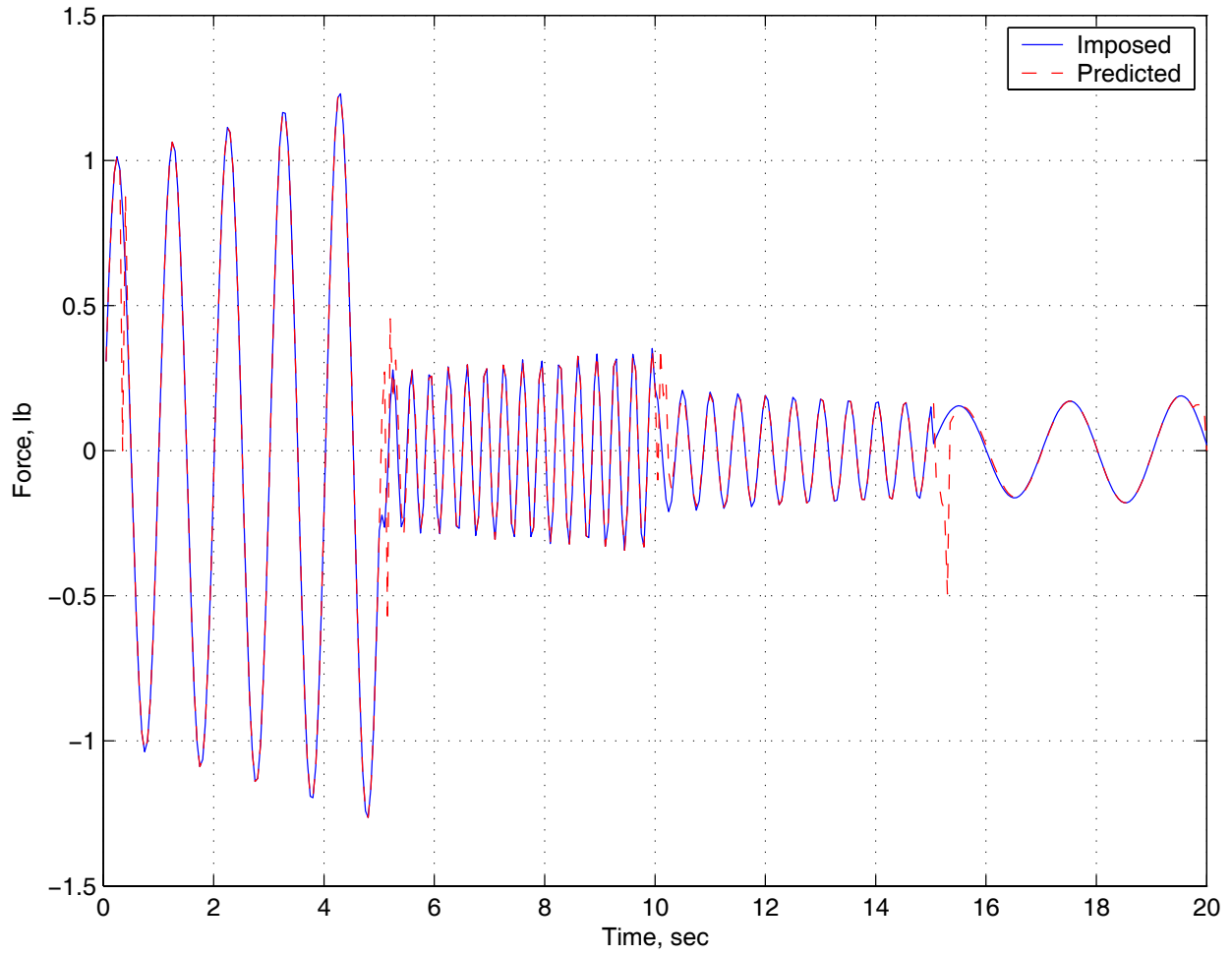


Figure A7.- Imposed versus predicted disturbance time histories using a 6-term AR model updated at each time step using RLS.

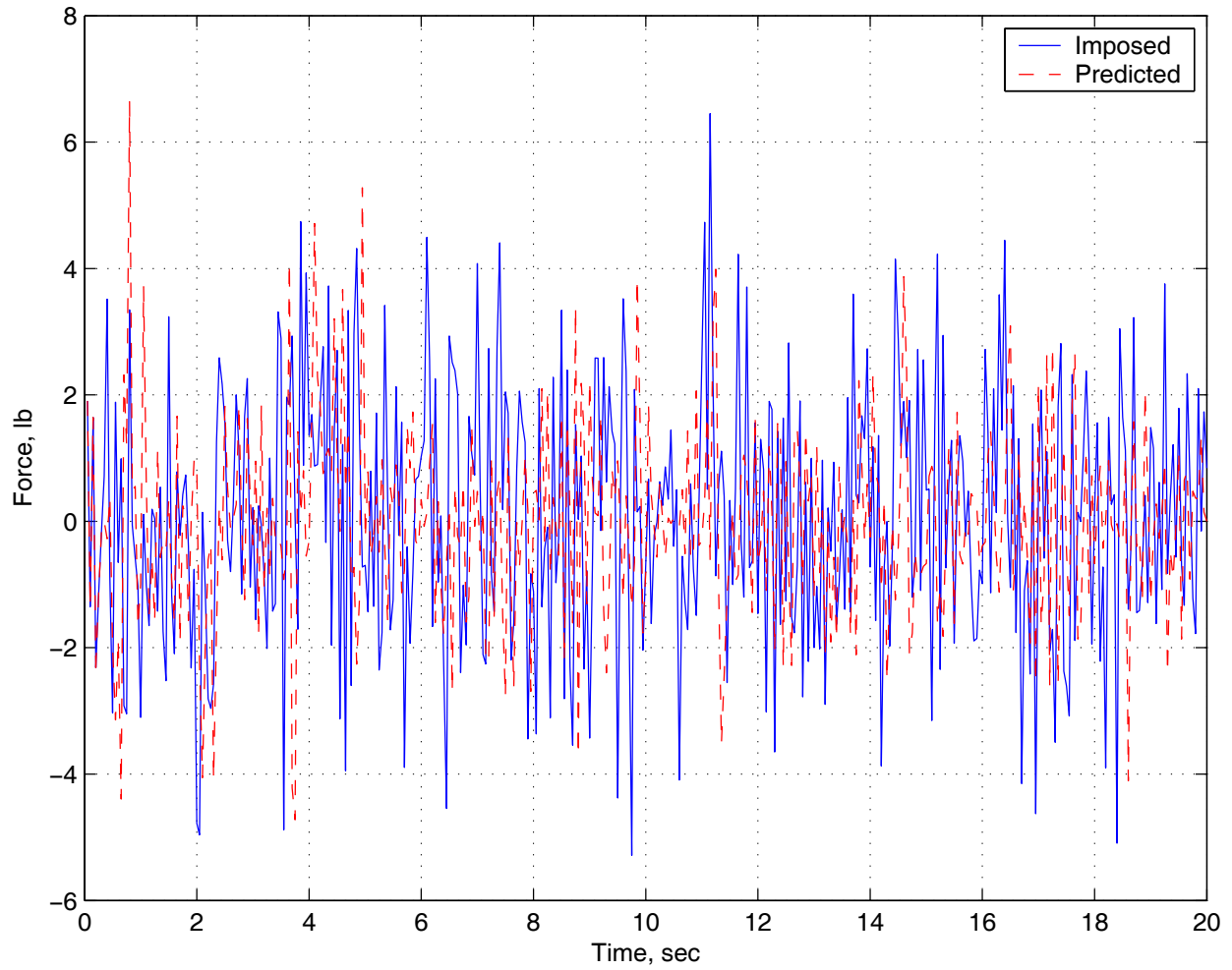


Figure A8.- Imposed versus predicted disturbance time histories using a 6-term AR model updated at each time step using RLS.

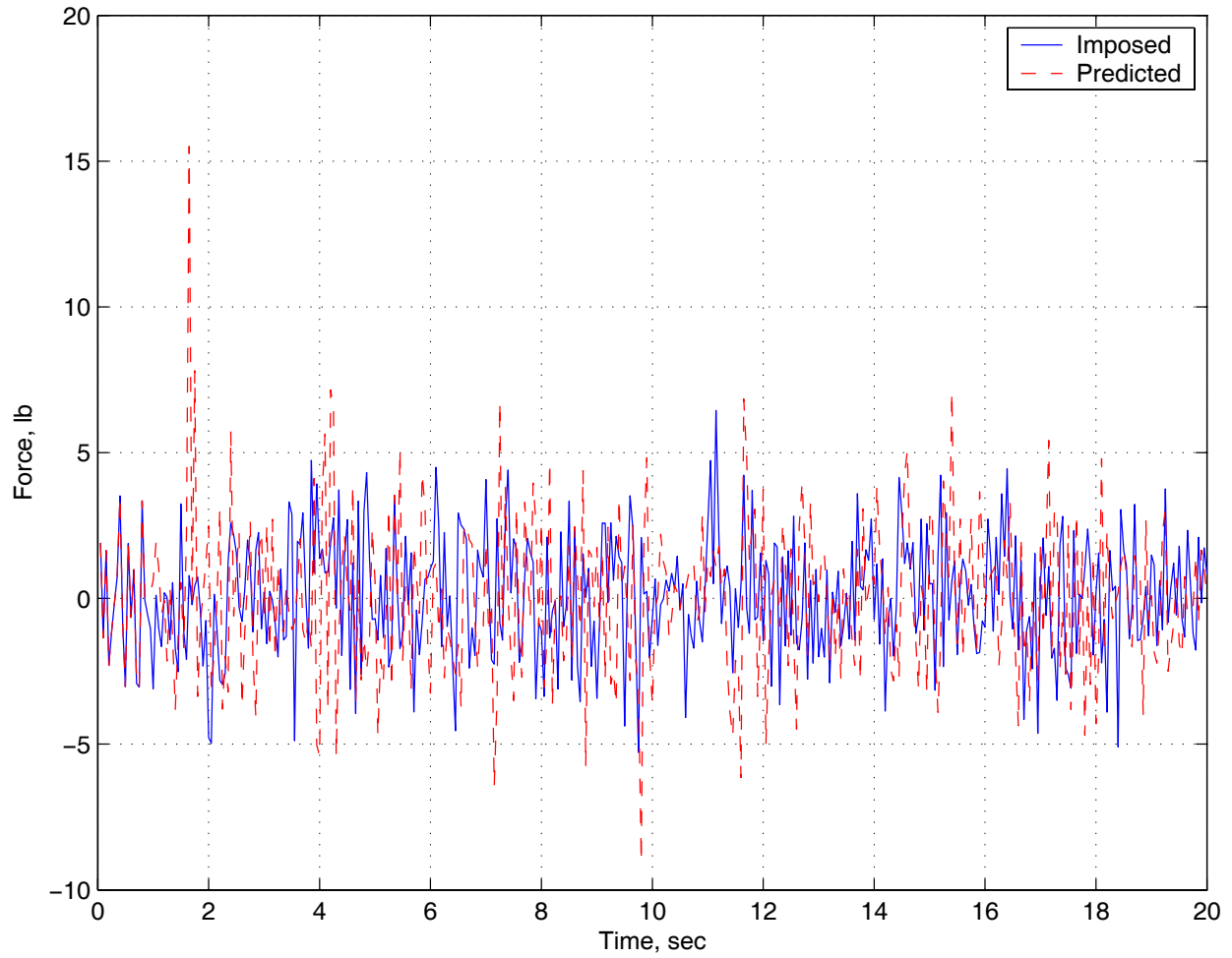


Figure A9.- Imposed versus predicted disturbance time histories using a 16-term AR model updated at each time step using RLS.

## Appendix B

### State-Space Equations for 3-DOF Mass-Spring-Dashpot System

The second-order matrix equations of motion for the 3-degree-of-freedom mass-spring-dashpot system shown in figure 2 are given by

$$\begin{aligned}
 & \begin{bmatrix} m_1 & 0 & 0 \\ 0 & m_2 & 0 \\ 0 & 0 & m_3 \end{bmatrix} \begin{Bmatrix} \ddot{x}_1 \\ \ddot{x}_2 \\ \ddot{x}_3 \end{Bmatrix} + \begin{bmatrix} c_1 + c_2 & -c_2 & 0 \\ -c_2 & c_2 + c_3 & -c_3 \\ 0 & -c_3 & c_3 \end{bmatrix} \begin{Bmatrix} \dot{x}_1 \\ \dot{x}_2 \\ \dot{x}_3 \end{Bmatrix} + \begin{bmatrix} k_1 + k_2 & -k_2 & 0 \\ -k_2 & k_2 + k_3 & -k_3 \\ 0 & -k_3 & k_3 \end{bmatrix} \begin{Bmatrix} x_1 \\ x_2 \\ x_3 \end{Bmatrix} = \begin{Bmatrix} f_1 \\ f_2 \\ f_3 \end{Bmatrix} \\
 & = \begin{bmatrix} 1 & 0 & 0 & 1 & 0 & 0 \\ 0 & 1 & 0 & 0 & 1 & 0 \\ 0 & 0 & 1 & 0 & 0 & 1 \end{bmatrix} \begin{Bmatrix} ud_1 \\ ud_2 \\ ud_3 \\ uc_1 \\ uc_2 \\ uc_3 \end{Bmatrix} = \begin{bmatrix} [I_{ud}] & [I_{uc}] \end{bmatrix} \begin{Bmatrix} \{ud\} \\ \{uc\} \end{Bmatrix} = [B_2] \{u\} \tag{B1}
 \end{aligned}$$

where the external forces acting on the system are divided into disturbance forces  $u_{di}$  and control forces  $u_{ci}$  for convenience in controls simulation work. The matrix  $[B_2]$  is an input influence matrix indicating the locations and types of force inputs. Equation B1 can be written compactly as

$$[M]\{\ddot{x}\} + [C]\{\dot{x}\} + [K]\{x\} = \{f\} = [B_2]\{u\} \tag{B2}$$

The corresponding first-order equations describing the continuous-time state-space model for the system are given by the state equation

$$\{\dot{X}\} = [A_c]\{X\} + [B_c]\{u\} \tag{B3}$$

and the output equation

$$\{y\} = [C_c]\{X\} + [D_c]\{u\} \tag{B4}$$

where the state matrix  $[A_c]$ , state matrix  $[B_c]$ , and state vector  $\{X\}$  are given by

$$[A_c] = \begin{bmatrix} [0] & [I] \\ -[M^{-1}K] & -[M^{-1}C] \end{bmatrix}; \quad [B_c] = \begin{bmatrix} [0] \\ [M^{-1}B_2] \end{bmatrix}; \quad \{X\} = \begin{Bmatrix} \{x\} \\ \{\dot{x}\} \end{Bmatrix} \tag{B5}$$

The outputs (measured physical quantities) are related to the state variables and the inputs by the output equation which can be written as

$$\{y\} = [C_d \quad C_v] \begin{Bmatrix} \{x\} \\ \{\dot{x}\} \end{Bmatrix} + [C_a] \{\ddot{x}\} \quad (\text{B6})$$

where  $C_d$ ,  $C_v$ , and  $C_a$  are  $3 \times 3$  output influence matrices for displacement, velocity, and acceleration, respectively, and have the form

$$[C_d] = \begin{bmatrix} c_{d_1} & & \\ & c_{d_2} & \\ & & c_{d_3} \end{bmatrix}; \quad [C_v] = \begin{bmatrix} c_{v_1} & & \\ & c_{v_2} & \\ & & c_{v_3} \end{bmatrix}; \quad [C_a] = \begin{bmatrix} c_{a_1} & & \\ & c_{a_2} & \\ & & c_{a_3} \end{bmatrix} \quad (\text{B7})$$

These matrices describe the relationship between the vectors  $\{x\}$ ,  $\{\dot{x}\}$ ,  $\{\ddot{x}\}$  and the measurement vector  $\{y\}$ . If the measurement unit is a physical unit (e.g., displacement, velocity, or acceleration) the corresponding term is unity; otherwise there is a conversion factor from physical units to the measurement units.

Solving equation B2 for  $\{\ddot{x}\}$  and substituting into equation B6 gives

$$\{y\} = [C_d \quad C_v] \begin{Bmatrix} \{x\} \\ \{\dot{x}\} \end{Bmatrix} + [C_a] \left[ -[M^{-1}C] \{\dot{x}\} - [M^{-1}K] \{x\} + [M^{-1}B_2] \{u\} \right] \quad (\text{B8a})$$

or

$$\{y\} = [C_d - C_a M^{-1}K \quad C_v - C_a M^{-1}C] \begin{Bmatrix} \{x\} \\ \{\dot{x}\} \end{Bmatrix} + [C_a M^{-1}B_2] \{u\} \quad (\text{B8b})$$

or

$$\{y\} = [C_d - C_a M^{-1}K \quad C_v - C_a M^{-1}C] \{X\} + [C_a M^{-1}B_2] \{u\} \quad (\text{B8c})$$

which can be written compactly as

$$\{y\} = [C_c] \{X\} + [D_c] \{u\} \quad (\text{B9})$$

where  $[C_c]$  and  $[D_c]$  are the output and direct transmission matrices and are given by

$$[C_c] = \begin{bmatrix} C_d - C_a M^{-1} K & C_v - C_a M^{-1} C \end{bmatrix} \quad (\text{B10})$$

$$[D_c] = [C_a M^{-1} B_2]$$

The direct transmission matrix  $[D_c]$  is zero if accelerations are not included in the output measurements  $\{y\}$  (in which case  $[C_a] = [0]$ ), or if accelerations are measured but there are no external forces (disturbance and control) acting at those locations (in which case some of the diagonal elements of  $I_{ud}$  and  $I_{uc}$  will be zero).

Special cases of the general equations given above are easily obtained. For example, the number, type, and combination of input and output quantities can be varied by deleting appropriate rows of the output equation and/or zeroing appropriate diagonal elements in  $I_{ud}$ ,  $I_{uc}$ ,  $C_d$ ,  $C_v$ , and  $C_a$ .

## References

1. Juang, J.-N., and Eure, K. W.: Predictive Feedback and Feedforward Control for Systems with Unknown Disturbances, NASA/TM-1998-208744, December 1998.
2. Kvaternik, R. G.; Juang, J.-N.; and Bennett, R. L.: Exploratory Studies in Generalized Predictive Control for Active Aeroelastic Control of Tiltrotor Aircraft. NASA TM-2000-210552, October 2000.
3. Kvaternik, R. G.; Piatak, D. J.; Nixon, M. W.; Langston, C. W.; Singleton, J. D.; Bennett, R. L.; and Brown, R. K.: An Experimental Evaluation of Generalized Predictive Control for Tiltrotor Aeroelastic Stability Augmentation in Airplane Mode of Flight. *J. Amer. Hel. Soc.*, Vol. 27, No. 3, July 2002, pp. 198-208.
4. Nixon, M. W.; Langston, C. W.; Singleton, J. D.; Piatak, D. J.; Kvaternik, R. G.; Corso, L. M.; and Brown, R. K.: Hover Test of a Soft-Inplane Gimballed Tiltrotor Model, *J. Amer. Helicopter Soc.*, Vol. 48, Jan 2003, pp. 63-66.
5. Nixon, M. W.; Langston, C. W.; Singleton, J. D.; Piatak, D. J.; Kvaternik, R. G.; Corso, L. M.; and Brown, R.: Aeroelastic Stability of a Four-Bladed Semi-Articulated Soft-Inplane Tiltrotor Model. Presented at the AHS 59th Annual Forum and Technology Display, May 6-8, 2003, Phoenix, Arizona. In American Helicopter Society 59th Annual Forum Proceedings.
6. Vartio, E.; Shimko, A.; Tilmann, C. P.; and Frick, P. M.: Structural Model Control and Gust Load Alleviation for a SensorCraft Concept. Presented at 46<sup>th</sup> AIAA/ASME/ASCE/AHS/ASC Structures, Structural Dynamics, and Materials Conference, Austin, TX, April 2005. Paper No. AIAA-2005-1946.
7. MATLAB Reference Guide. The MathWorks, Inc., Natick, MA, August 1992.
8. Clark, D. W. (Ed): *Advances in Model-Based Predictive Control*. Oxford University Press, New York, 1994.
9. Clarke, D. W.; Mohtadi, C.; and Tuffs, P. S.: Generalized Predictive Control – Parts I and II. *Automatica*, Vol. 23, No. 2, 1987, pp. 137-160.
10. Juang, J.-N., and Phan, M. Q.: *Identification and Control of Mechanical Systems*. Cambridge University Press, New York, NY, 2001, ISBN 0-521-78355-0.
11. Juang, J.-N.: *Applied System Identification*. Prentice-Hall, Englewood Cliffs, NJ, 1994.
12. Eure, K. W.; and Juang, J.-N.: *Broadband Noise Control Using Predictive Techniques*. NASA TM 110320, January 1997.

13. Juang, J.-N.: *State-Space System Realization with Input- and Output-Data Correlation*. NASA TP 3622, April 1997.
14. Juang, J.-N.; and Phan, M. Q.: *Deadbeat Predictive Controllers*. NASA TM 112862, May 1997.
15. Eure, K. W.: *Adaptive Predictive Feedback Techniques for Vibration Control*. Ph.D. Dissertation, Virginia Polytechnic Institute and State University, May 1998.
16. Phan, M. Q.; and Juang, J.-N.: Predictive Controllers for Feedback Stabilization. *Journal of Guidance, Control, and Dynamics*, Vol. 21, No. 5, Sept.-Oct. 1998, pp. 747-753.
17. Juang, J.-N.; and Eure, K. W.: *Predictive Feedback and Feedforward Control for Systems with Unknown Disturbances*. NASA/TM-1998-208744, December 1998.
18. Phan, M. Q.; Horta, L. G.; Juang, J.-N.; and Longman, R. W.: *Identification of Linear Systems by an Asymptotically Stable Observer*. NASA TP 3164, June 1992.
19. Juang, J.-N.; and Phan, M. Q.: *Recursive Deadbeat Controller Design*. NASA TM 112863, May 1997 (also, *Journal of Guidance, Control, and Dynamics*, Vol. 21, No. 5, Sept.-Oct. 1998, pp. 747-753).
20. Phan, M. Q.; and Juang, J.-N.: Predictive Feedback Controllers for Stabilization of Linear Multivariable Systems. *AIAA Guidance, Navigation and Control Conference*, San Diego, CA, July 29-31, 1996.
21. Åström, K. J.; and Wittenmark, B.: *Adaptive Control*. Addison-Wesley Publishing Company, New York, 1995.

**Table 1.- Reduction Factors for HiLDA Wing Model Moment Responses  
Using Embedded Feedforward**

<b>Gust Frequency</b>	<b>SBI2</b>	<b>SBY</b>	<b>STI2</b>
2 Hz	667	10	34
8 Hz	75	33	30
Swept from 0.5 – 10 Hz	31	7	4

**Table 2.- Reduction Factors for HiLDA Wing Model Moment Responses  
Using Explicit Feedforward**

<b>Gust Frequency</b>	<b>SBI2</b>	<b>SBY</b>	<b>STI2</b>
2 Hz	1000	30	170
8 Hz	500	100	60
Swept from 0.5 – 10 Hz	625	40	4

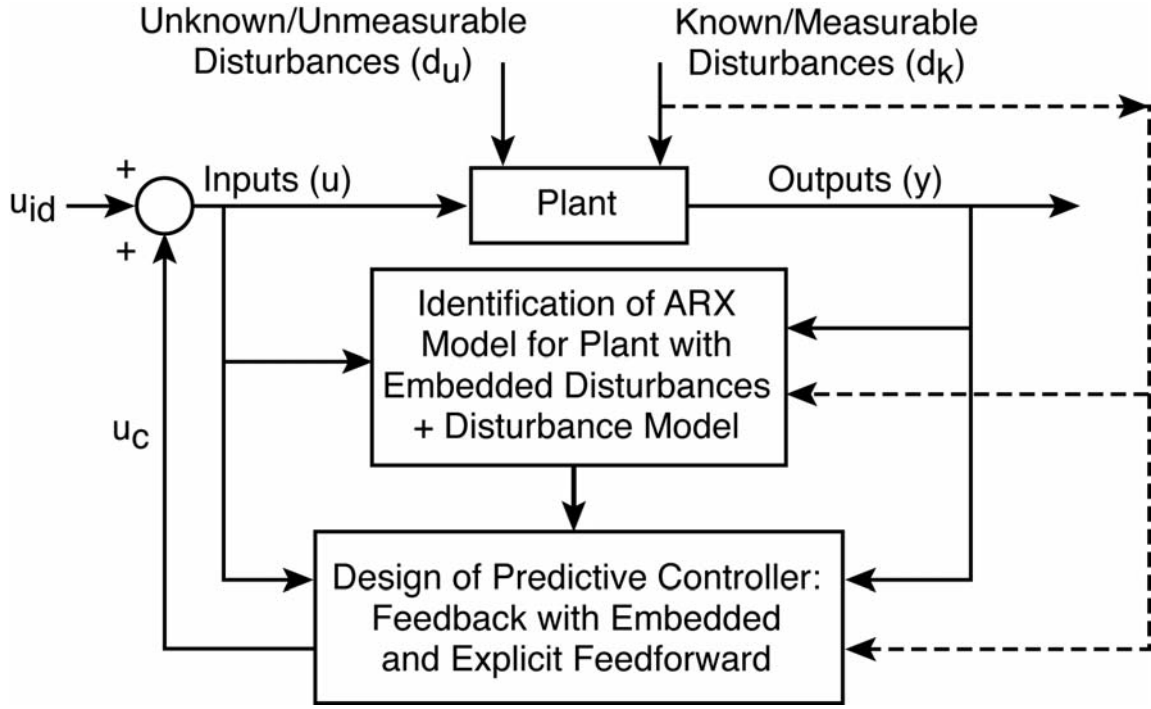


Figure 1.- Block diagram of GPC identification and control procedure.

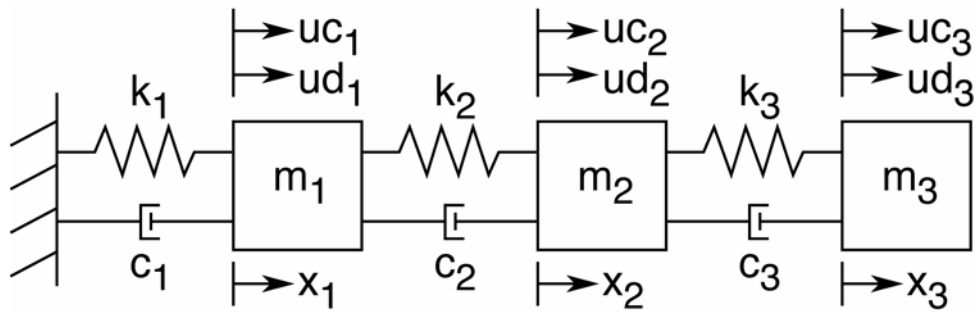


Figure 2.- Three-degree-of-freedom mass-spring-dashpot system.

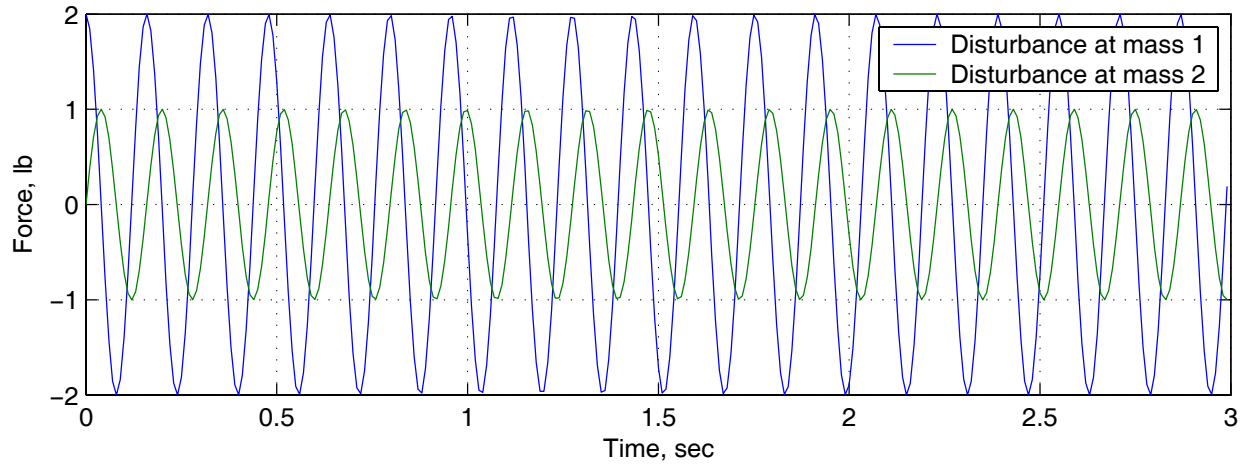
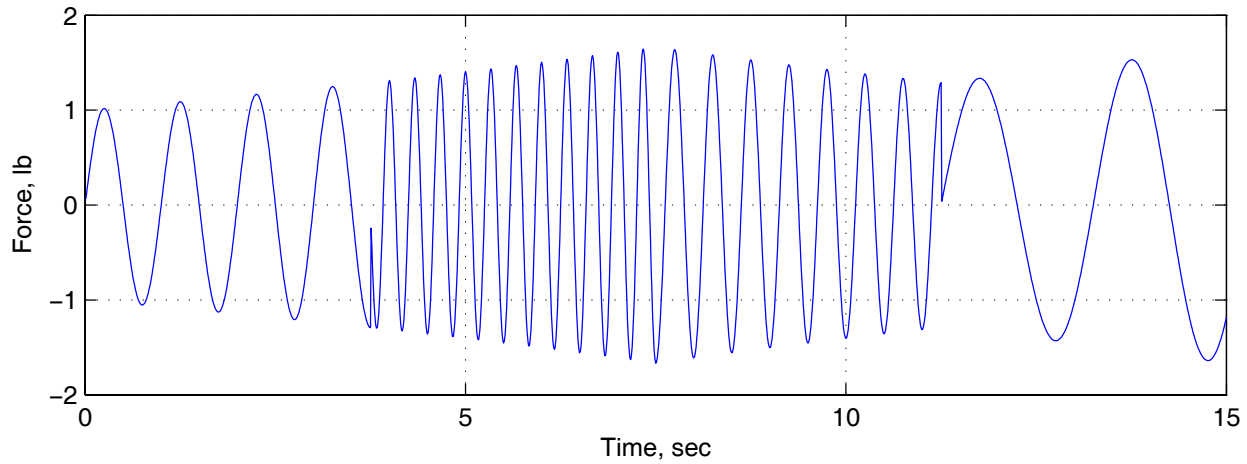
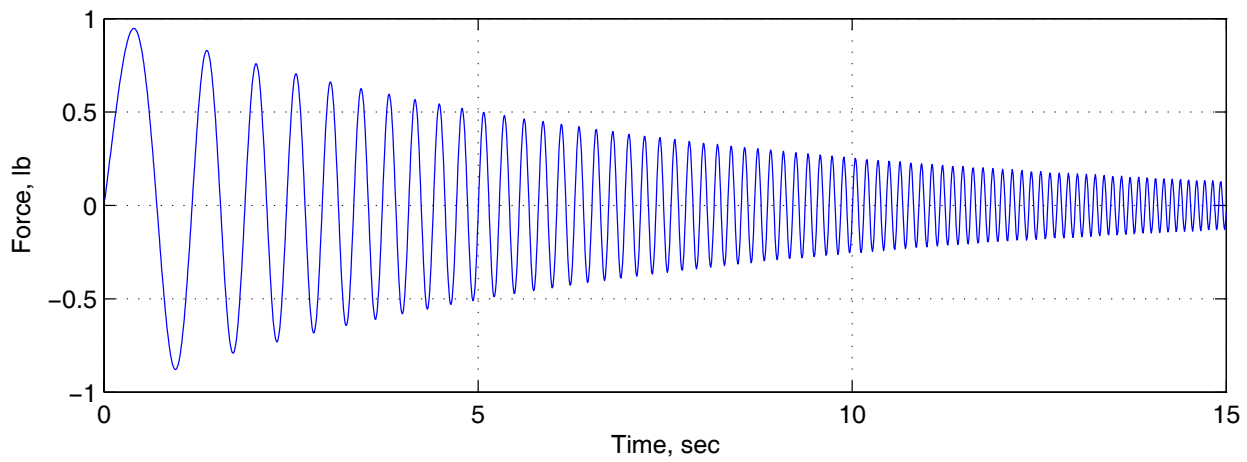


Figure 3.- Steady-state sinusoidal disturbances imposed on 3-DOF math model at masses 1 and 2 ( $ud_1$  and  $ud_2$ ).



(a) Piecewise varying frequency and amplitude



(b) Continuously varying frequency and amplitude

Figure 4.- Non-steady-state disturbances imposed on 3-DOF math model at mass 2 ( $ud_2$ ).

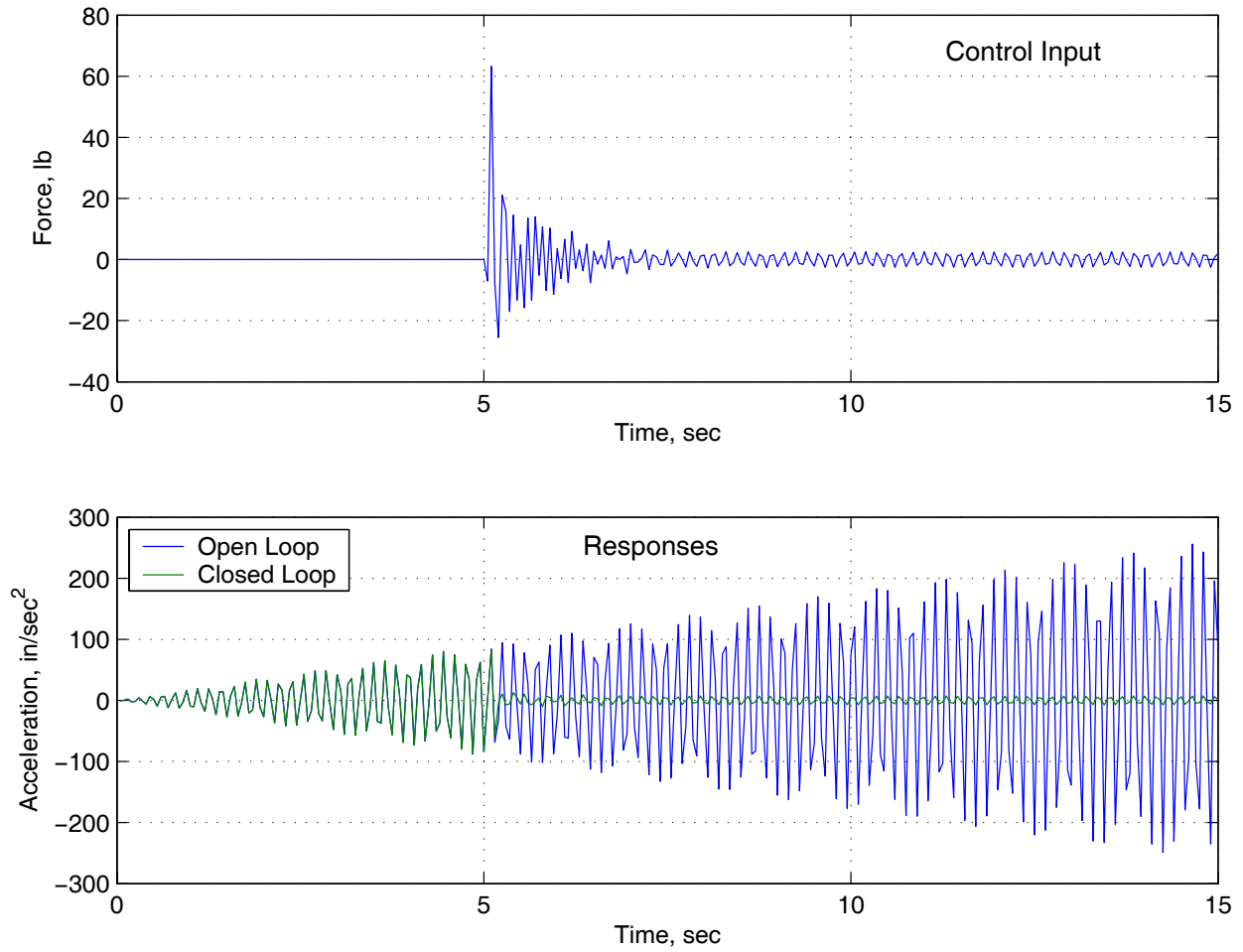


Figure 5.- Feedback only for 3 DOF system with steady-state disturbances (Control:  $uc_3$ ; Output:  $\ddot{x}_1$ ; Disturbance:  $ud_1$  and  $ud_2$ ).

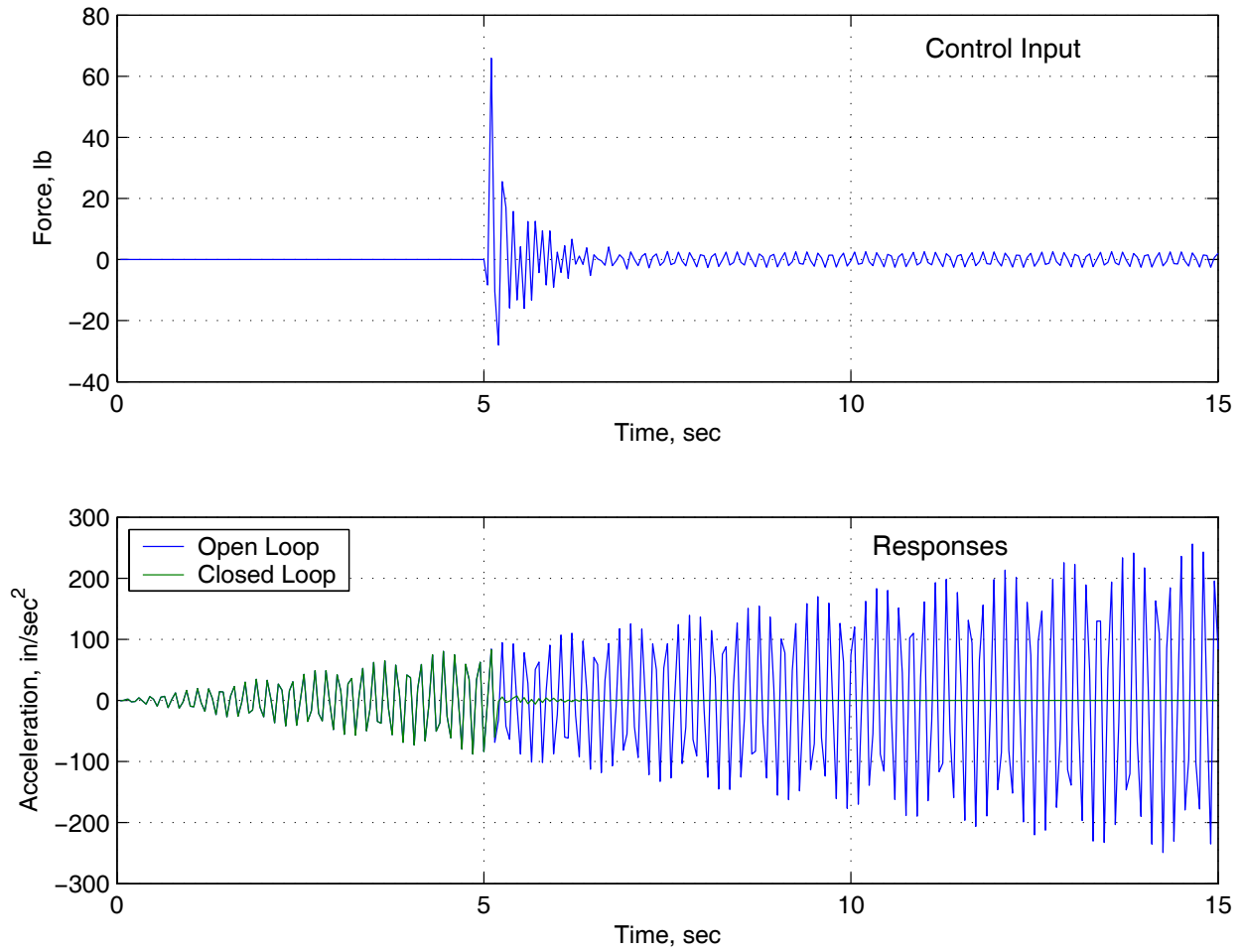


Figure 6.- Feedback with embedded feedforward for 3 DOF system with steady-state disturbances (Control:  $uc_3$ ; Output:  $\ddot{x}_1$ ; Disturbance:  $ud_1$  and  $ud_2$ ).

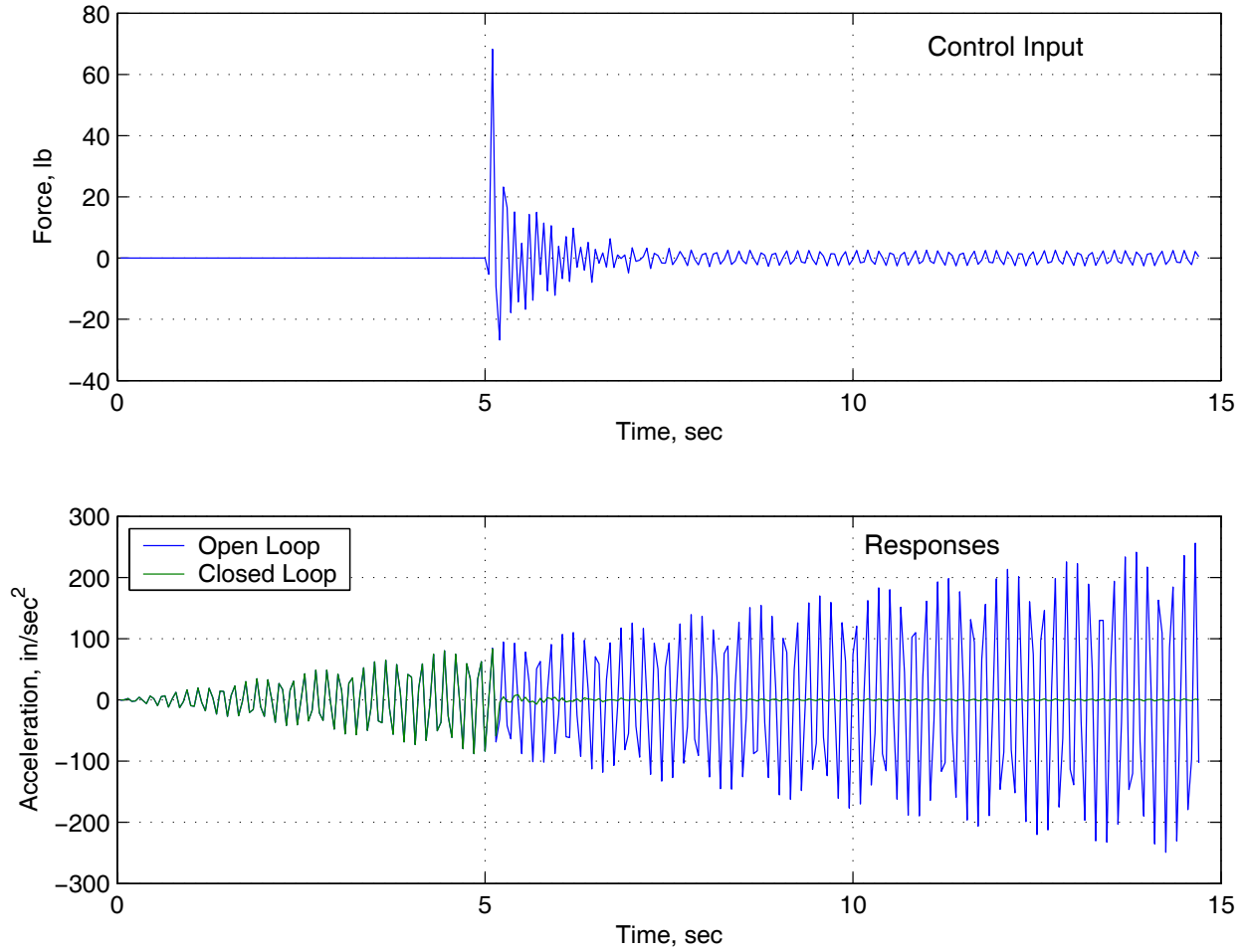


Figure 7.- Feedback with explicit feedforward of both steady-state disturbances for 3 DOF system (Control:  $uc_3$ ; Output:  $\ddot{x}_1$ ; Disturbance:  $ud_1$  and  $ud_2$ ).

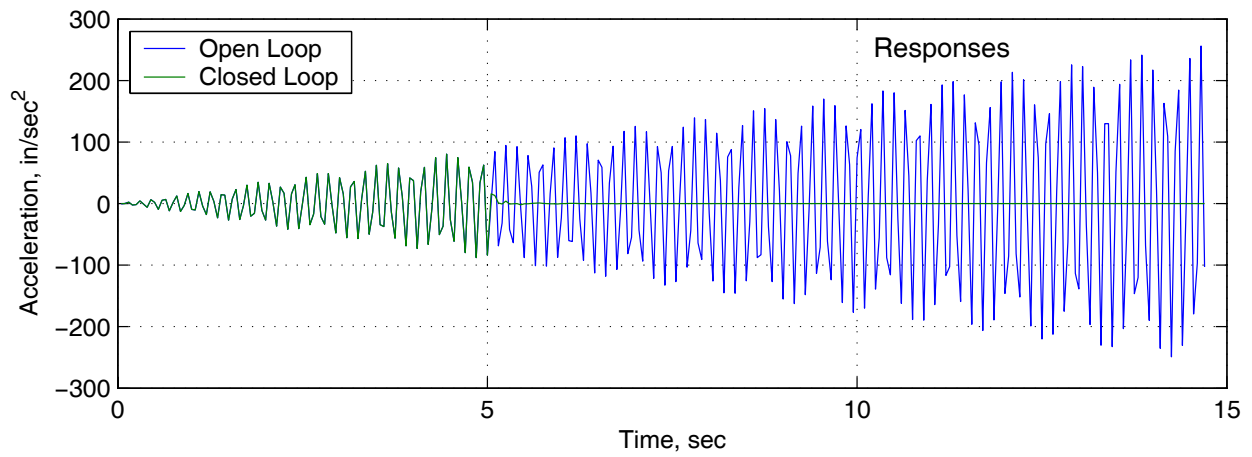
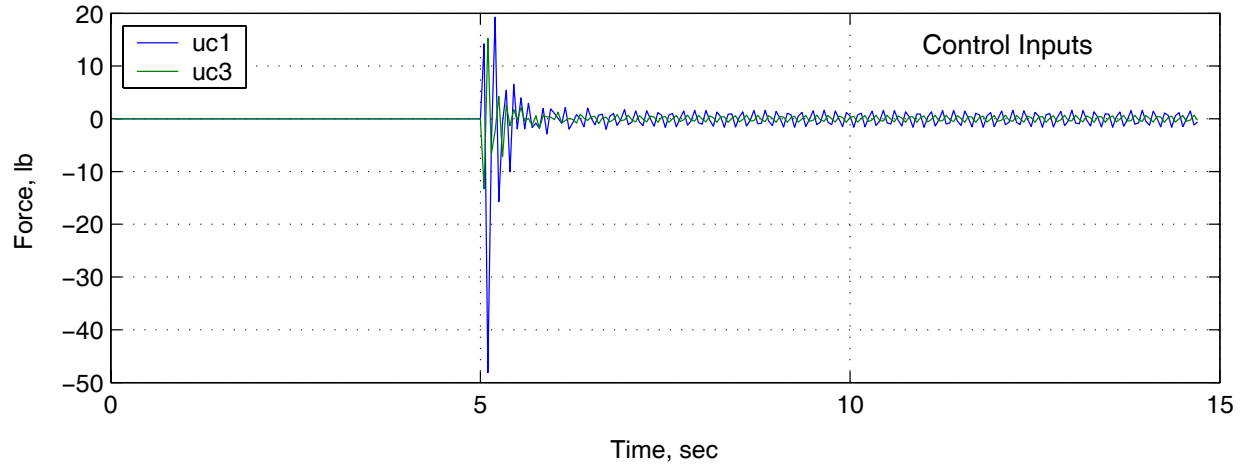


Figure 8.- Feedback with explicit feedforward of both steady-state disturbances for 3 DOF system (Control:  $uc_1$  and  $uc_3$ ; Output:  $\ddot{x}_1$ ; Disturbance:  $ud_1$  and  $ud_2$ ).

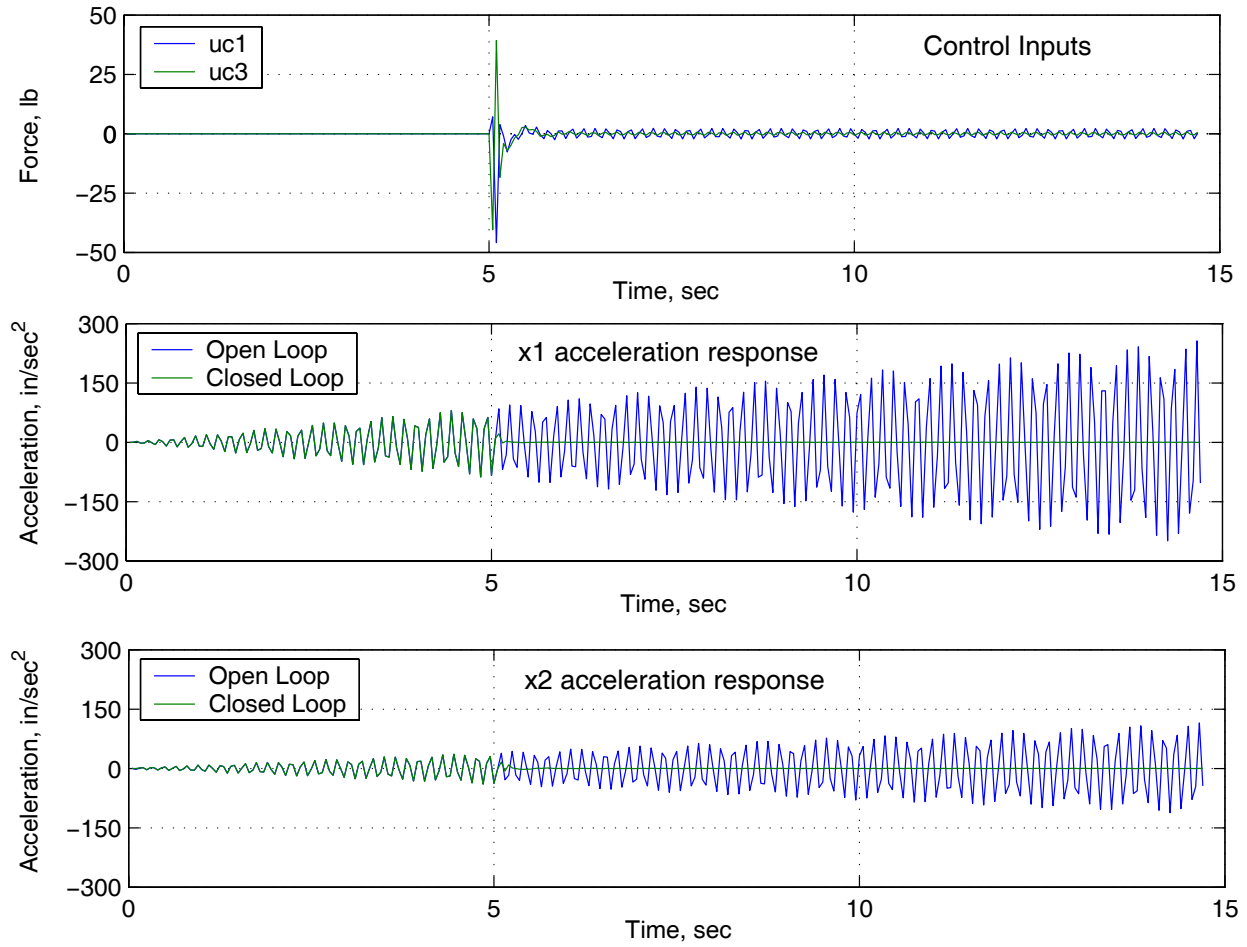


Figure 9.- Feedback with explicit feedforward of both steady-state disturbances for 3 DOF system (Control:  $uc_1$  and  $uc_3$ ; Output:  $\ddot{x}_1$  and  $\ddot{x}_2$ ; Disturbance:  $ud_1$  and  $ud_2$ )

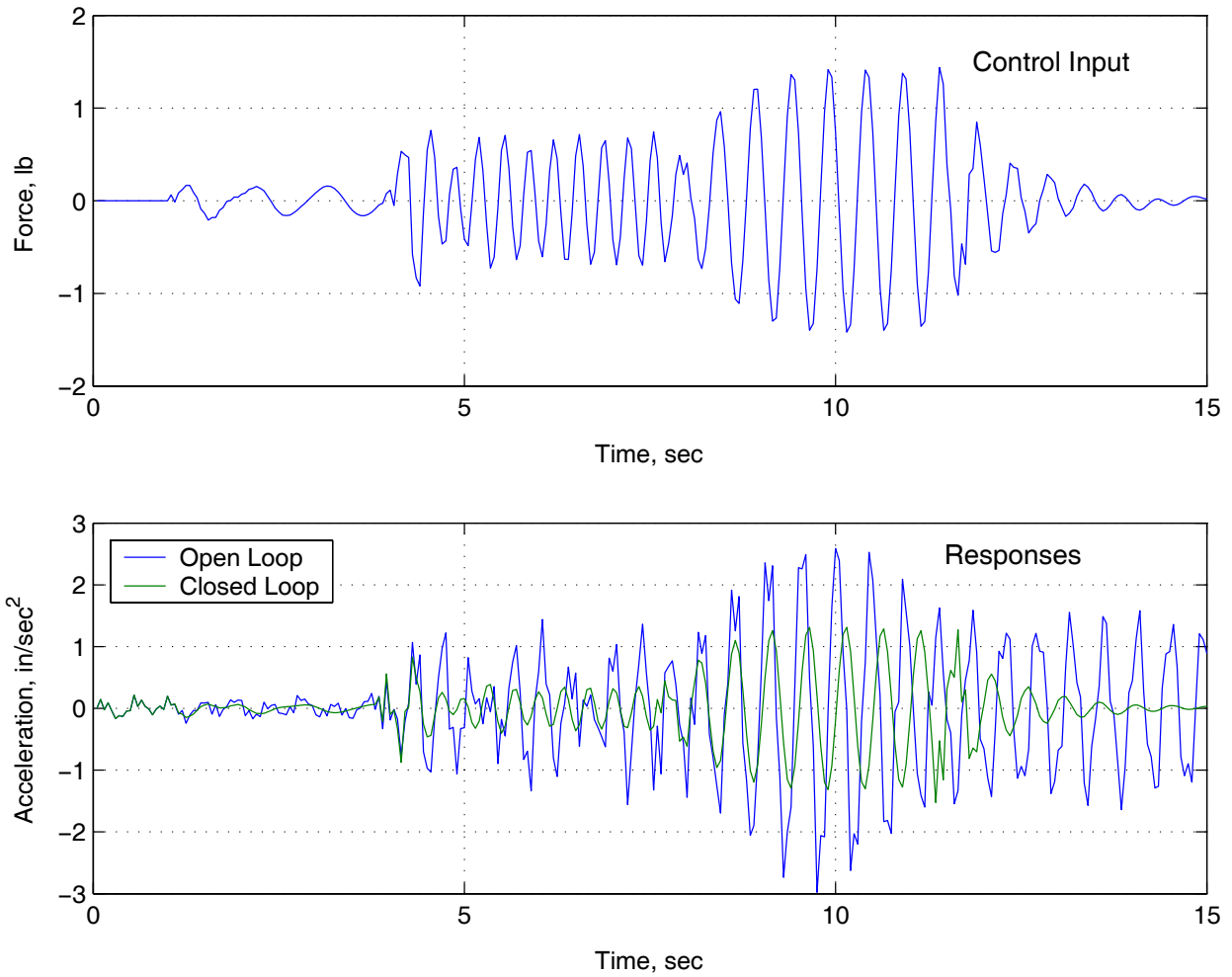


Figure 10.- Feedback with embedded feedforward of disturbance with piecewise varying amplitude and frequency (Control:  $uc_3$ ; Output:  $\ddot{x}_1$ ; Disturbance:  $ud_2$ ).

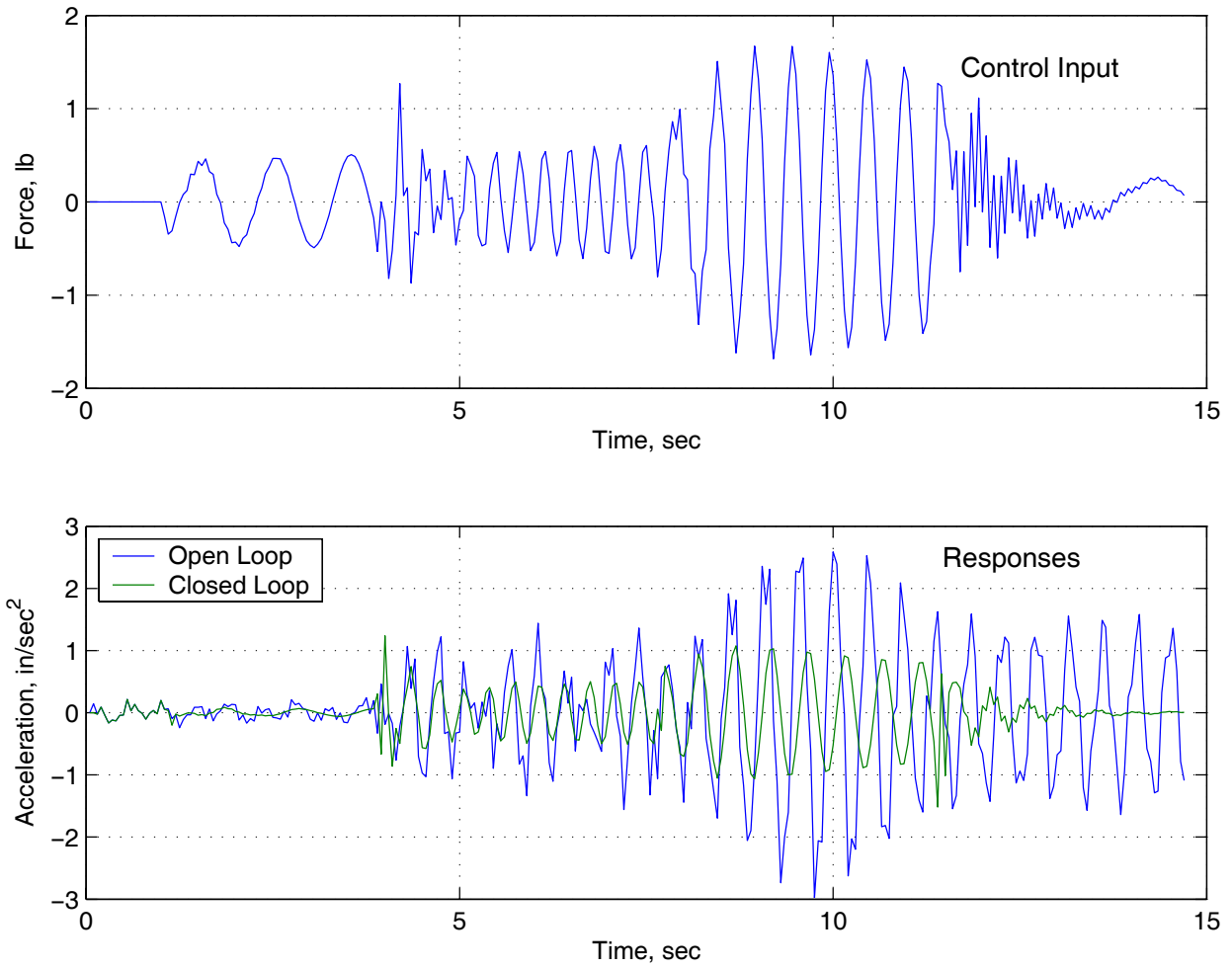


Figure 11.- Feedback with explicit feedforward of disturbance with piecewise varying amplitude and frequency (Control:  $uc_3$ ; Output:  $\ddot{x}_1$ ; Disturbance:  $ud_2$ ).

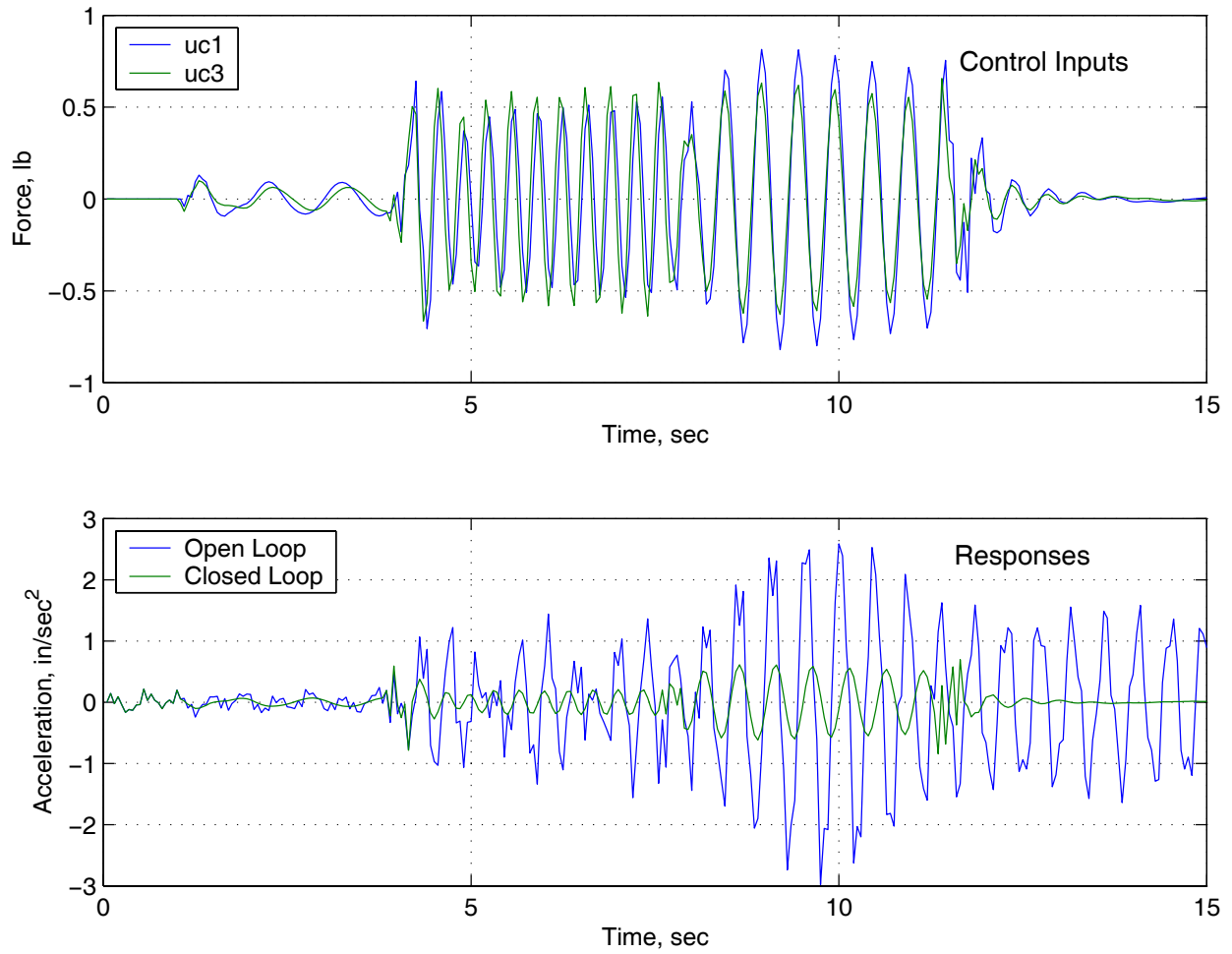


Figure 12.- Feedback with embedded feedforward of disturbance with piecewise varying amplitude and frequency (Control:  $uc_1$  and  $uc_3$ ; Output:  $\ddot{x}_1$ ; Disturbance:  $ud_2$ ).

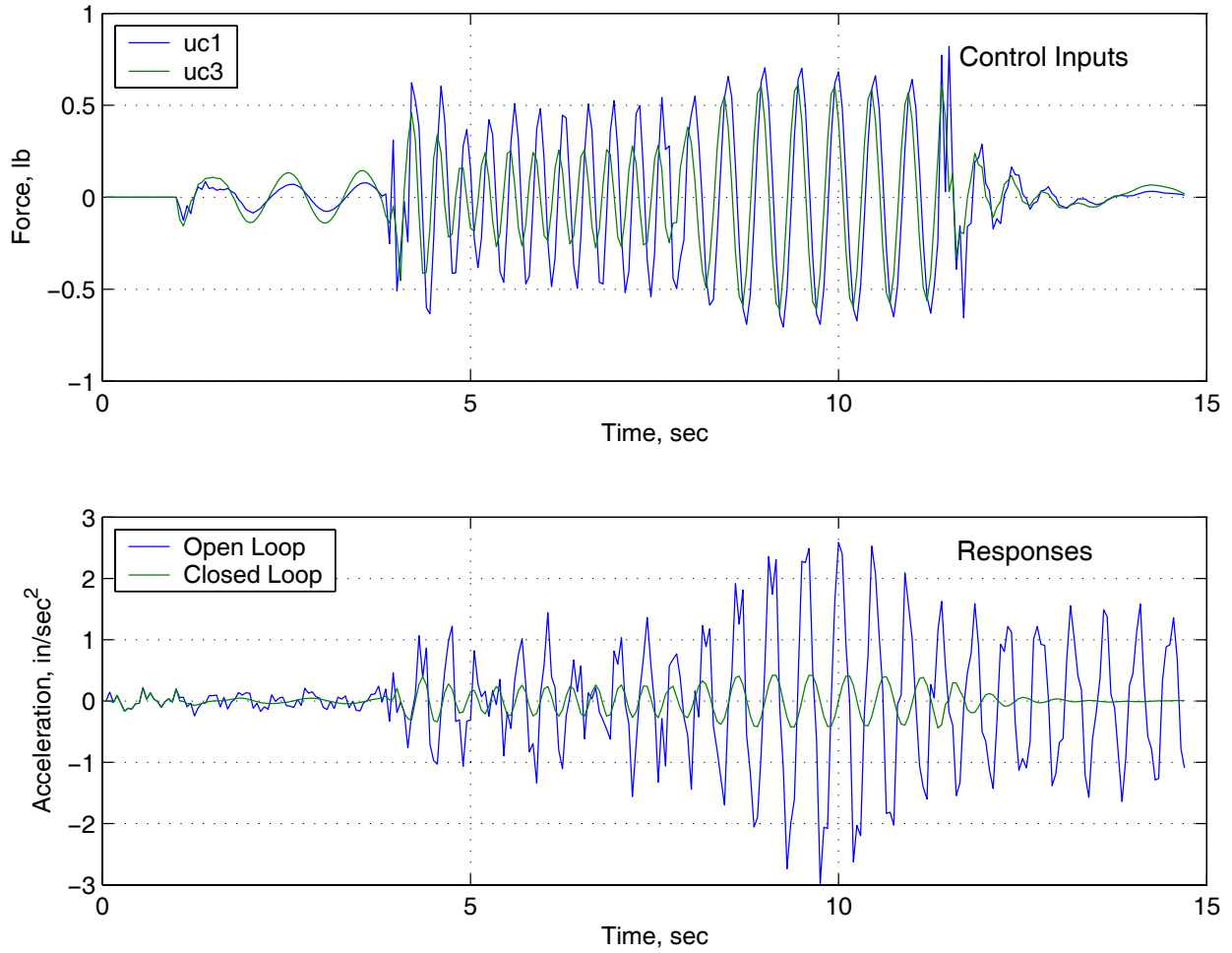


Figure 13.- Feedback with explicit feedforward of disturbance with piecewise varying amplitude and frequency (Control:  $uc_1$  and  $uc_3$ ; Output:  $\ddot{x}_1$ ; Disturbance:  $ud_2$ ).

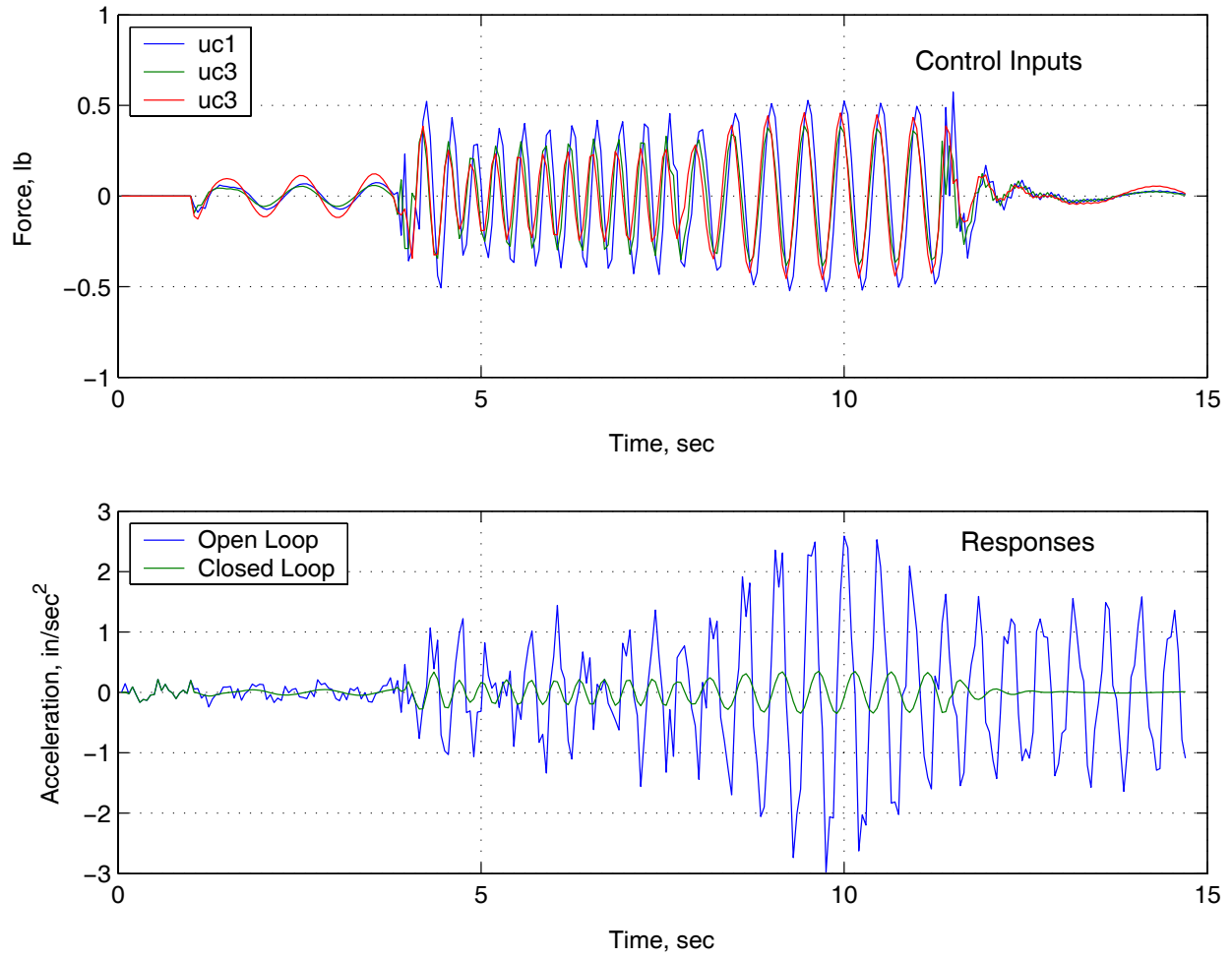


Figure 14.- Feedback with explicit feedforward of disturbance with piecewise varying amplitude and frequency (Control:  $uc_1$ ,  $uc_2$ , and  $uc_3$ ; Output:  $\ddot{x}_1$ ; Disturbance:  $ud_2$ ).

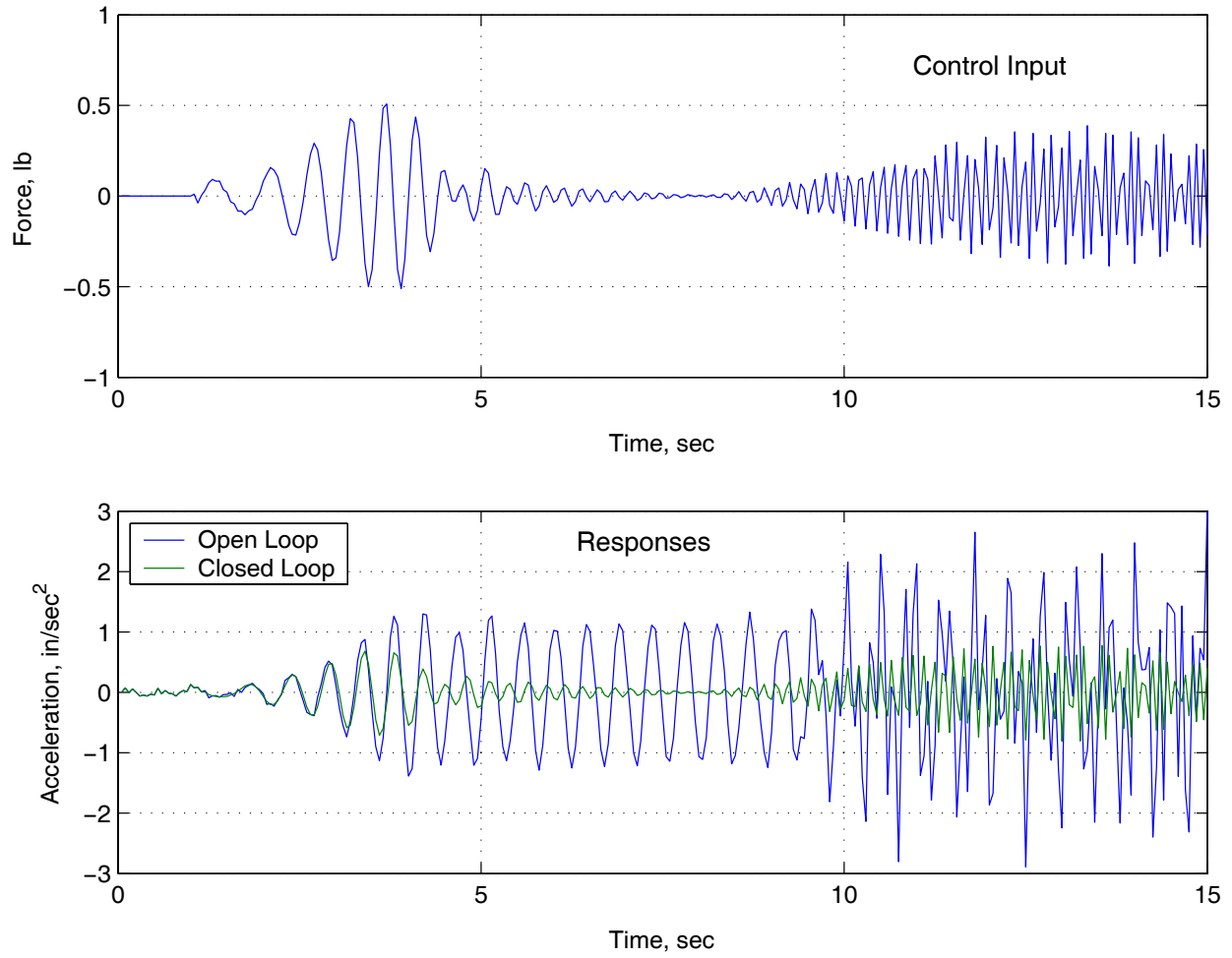


Figure 15.- Feedback with embedded feedforward of disturbance with continuously varying frequency and amplitude (Control:  $u_{C3}$ ; Output:  $\ddot{x}_1$ ; Disturbance:  $u_{D2}$ ).

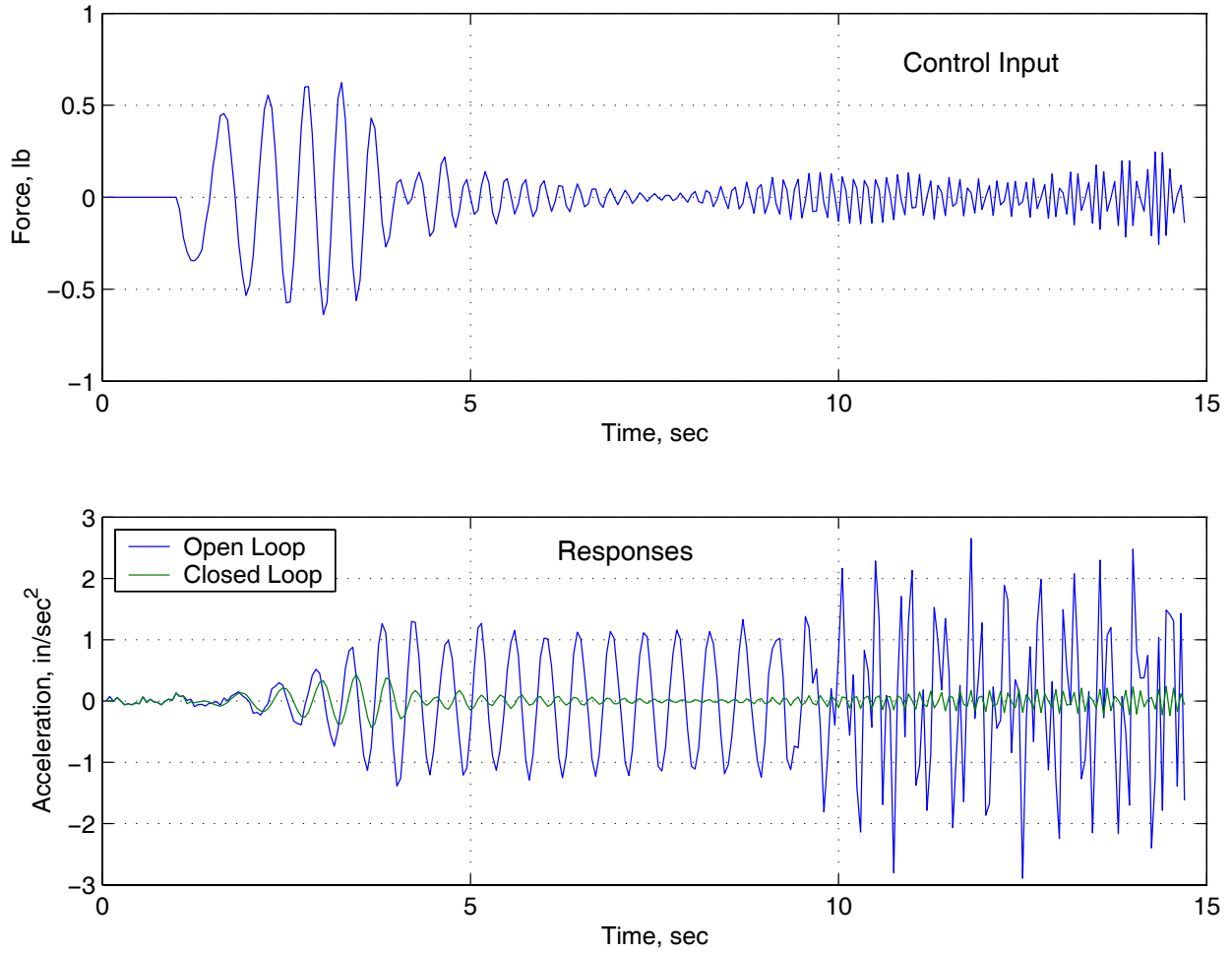


Figure 16.- Feedback with explicit feedforward of disturbance with continuously varying frequency and amplitude acting at mass 2 (Control:  $uc_3$ ; Output:  $\ddot{x}_1$ ; Disturbance  $ud_2$ ).

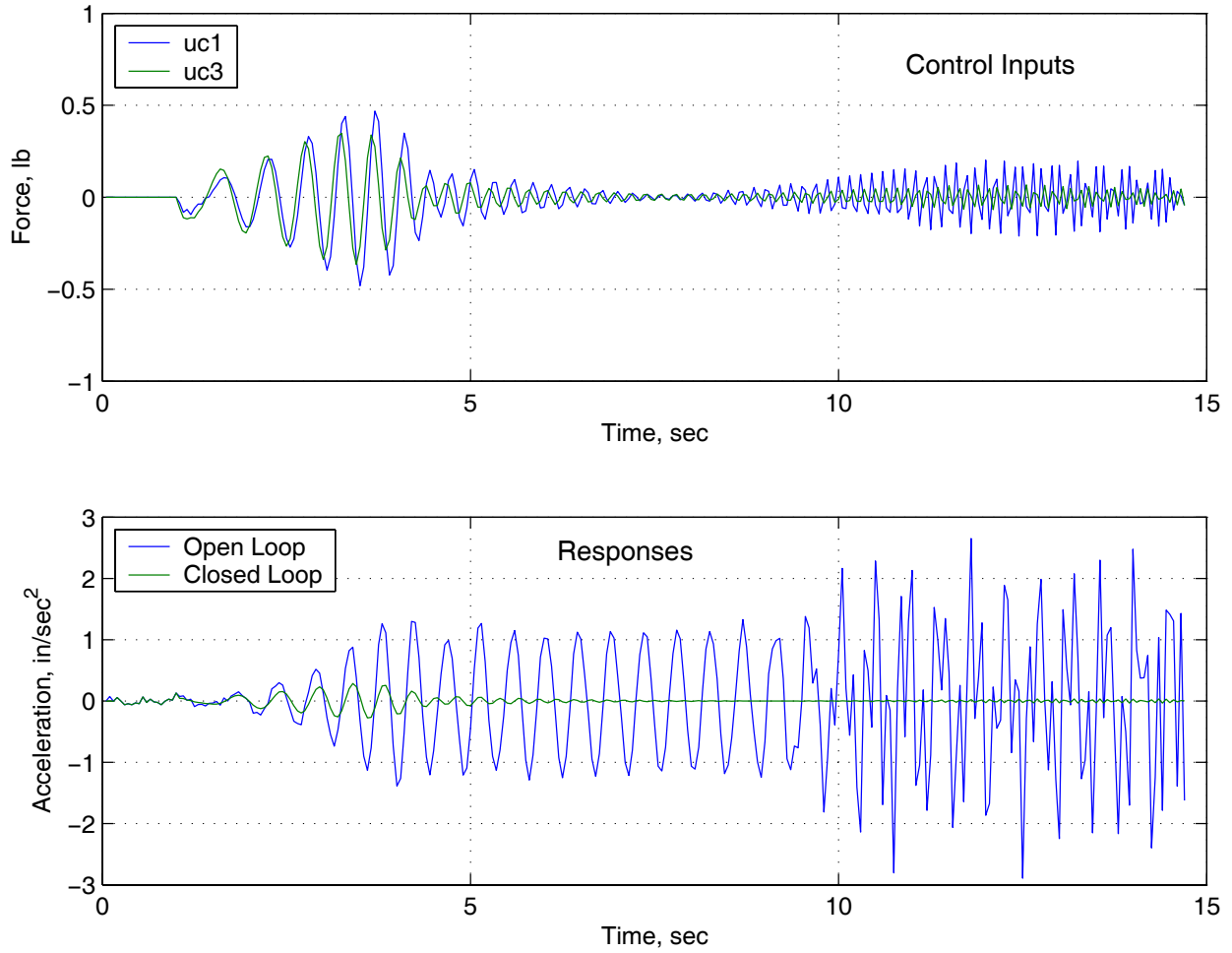


Figure 17.- Feedback with explicit feedforward of disturbance with continuously varying frequency and amplitude (Control:  $uc_1$  and  $uc_3$ ; Output:  $\ddot{x}_1$ ; Disturbance:  $ud_2$ ).

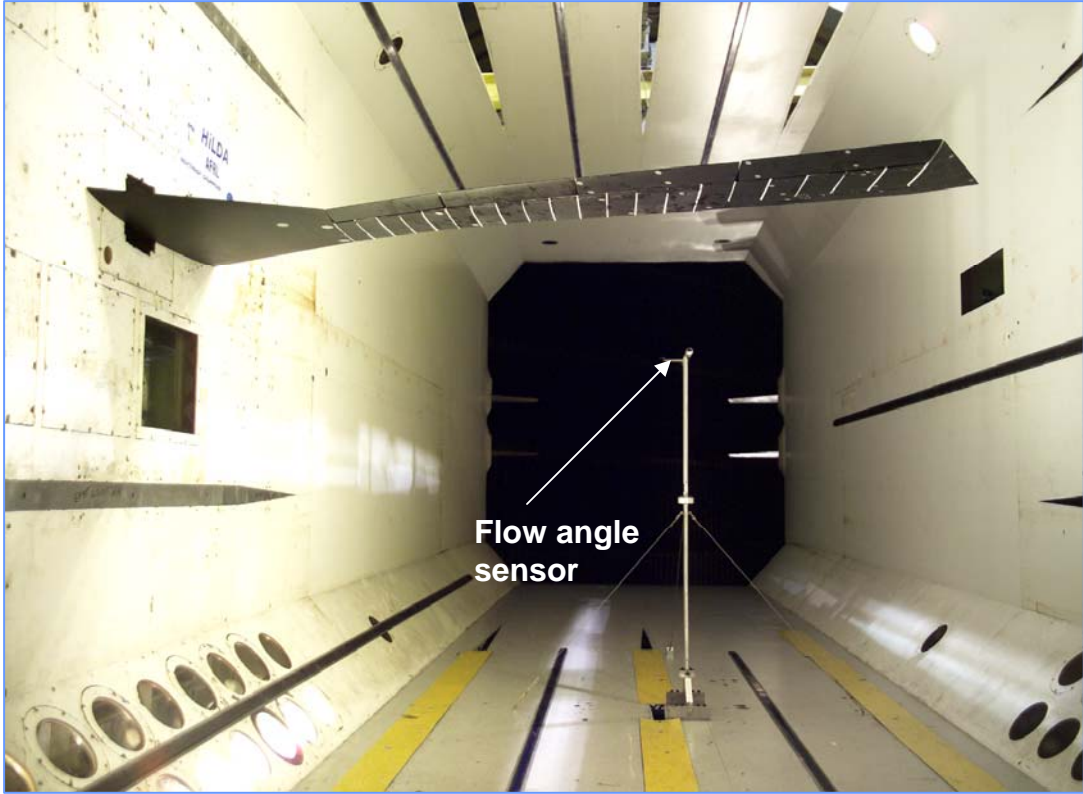


Figure 18.- HiLDA wing model in Langley Transonic Dynamics Tunnel. View looking upstream.



Figure 19.- Biplane vanes of TDT airstream oscillator system. View looking downstream toward model in test section.

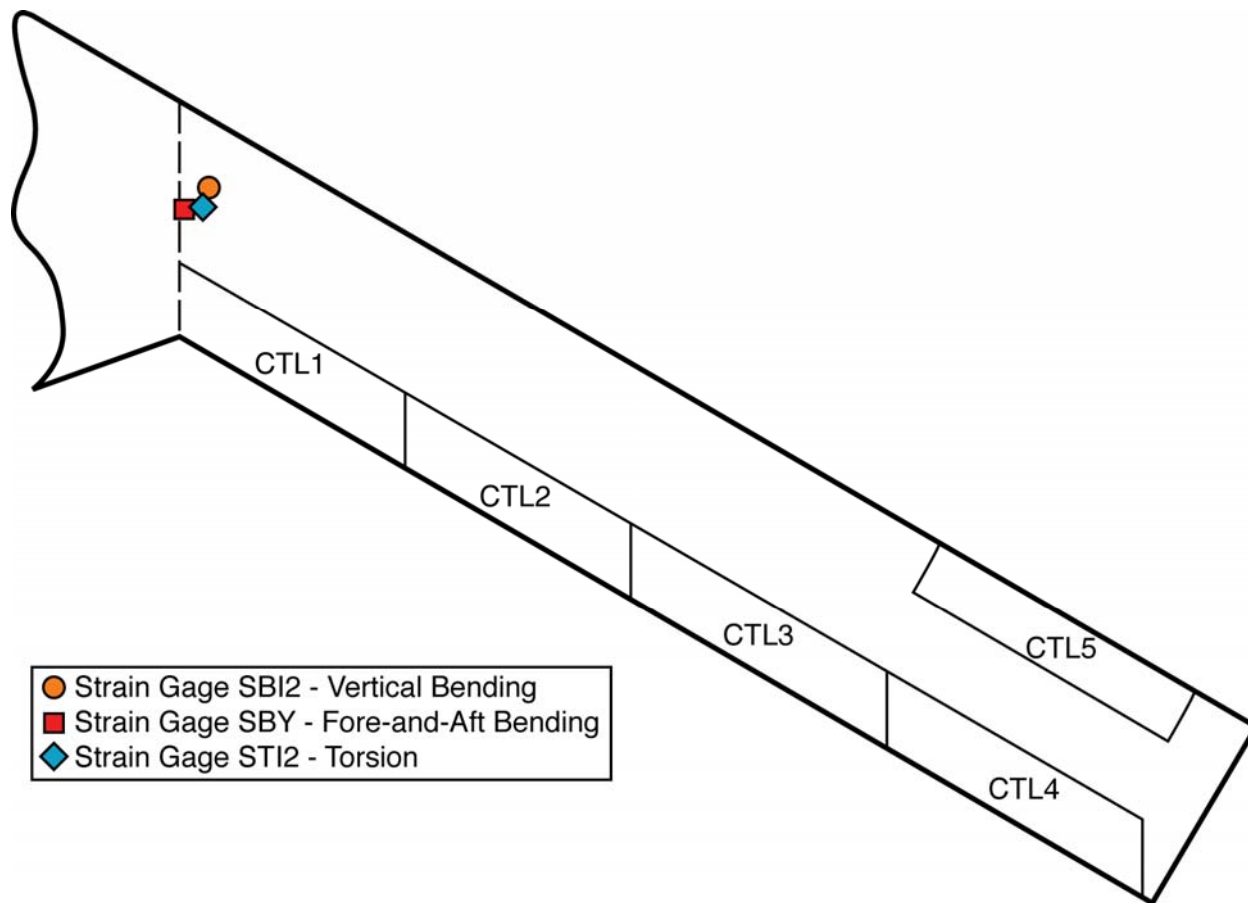


Figure 20.- Schematic of HiLDA model wing planform showing arrangement of control surfaces and locations of strain-gage response sensors used for simulations.

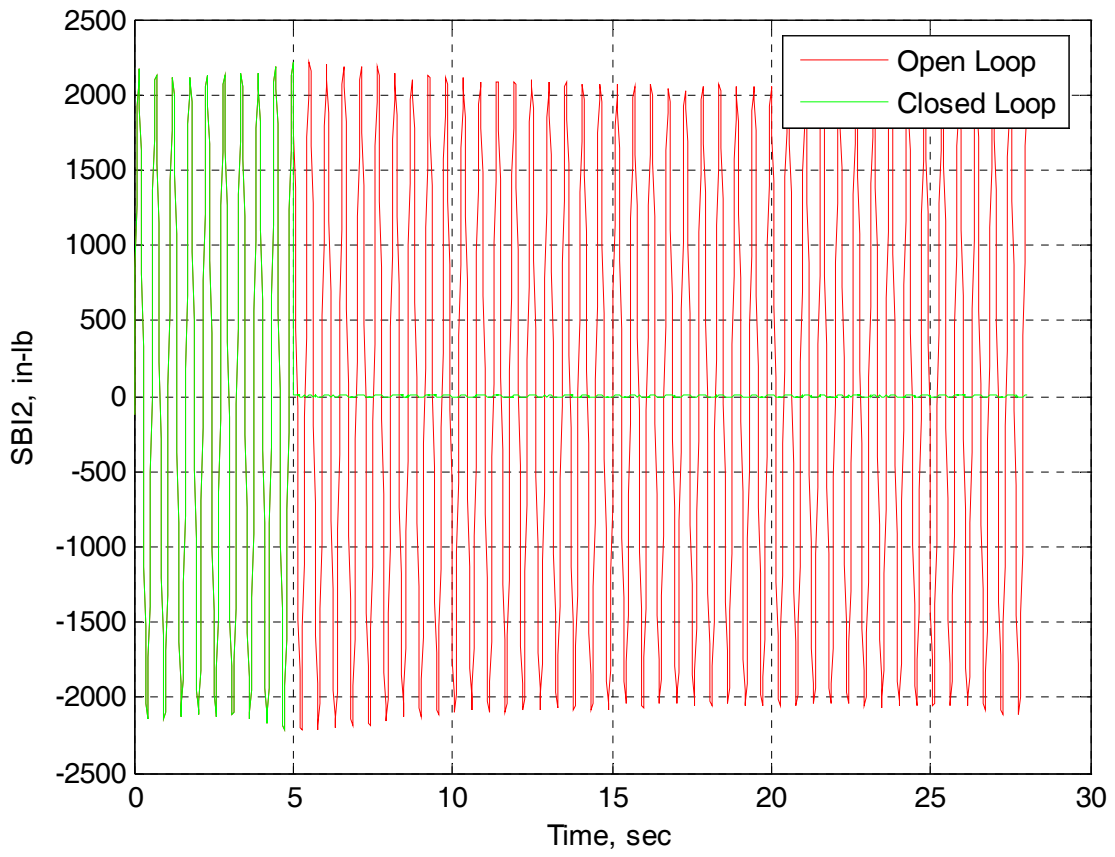


Figure 21.- Time histories of open- and closed-loop vertical bending moment (SBI2) during gust excitation at 2 Hz. Embedded feedforward.

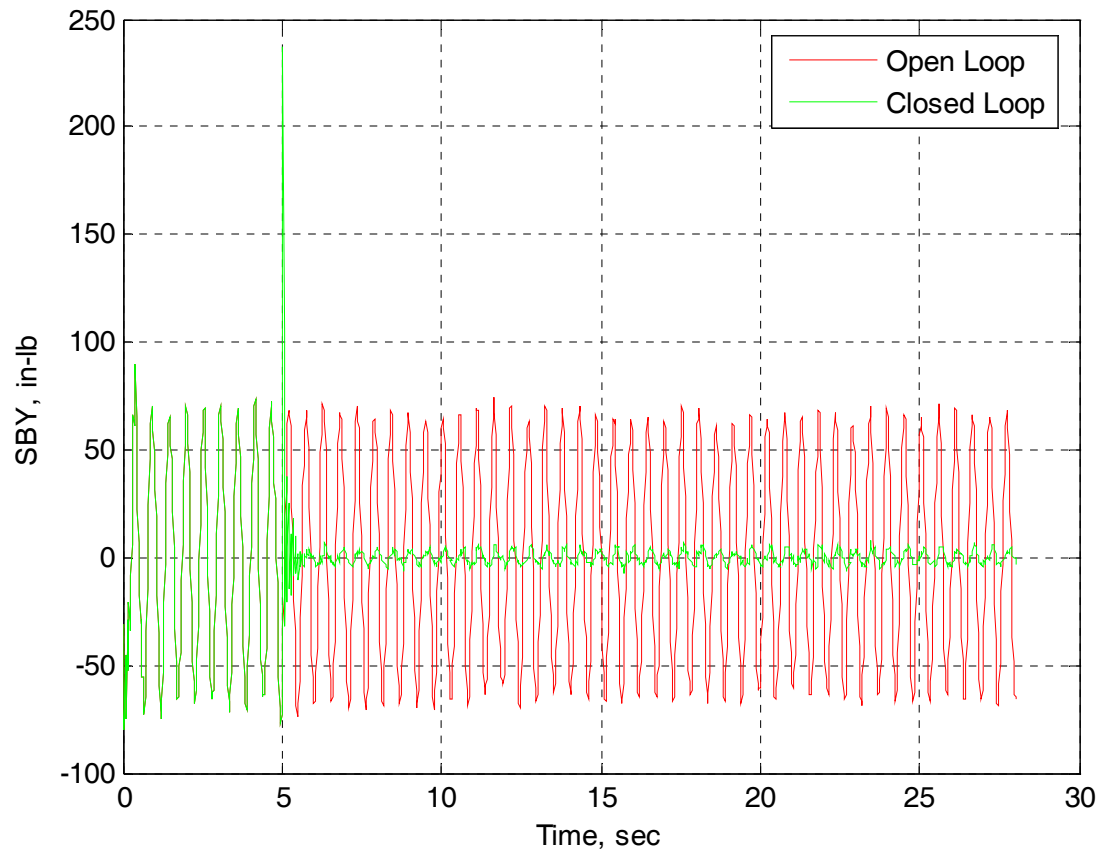


Figure 22.- Time histories of open- and closed-loop fore-and-aft bending moment (SBY) during gust excitation at 2 Hz. Embedded feedforward.

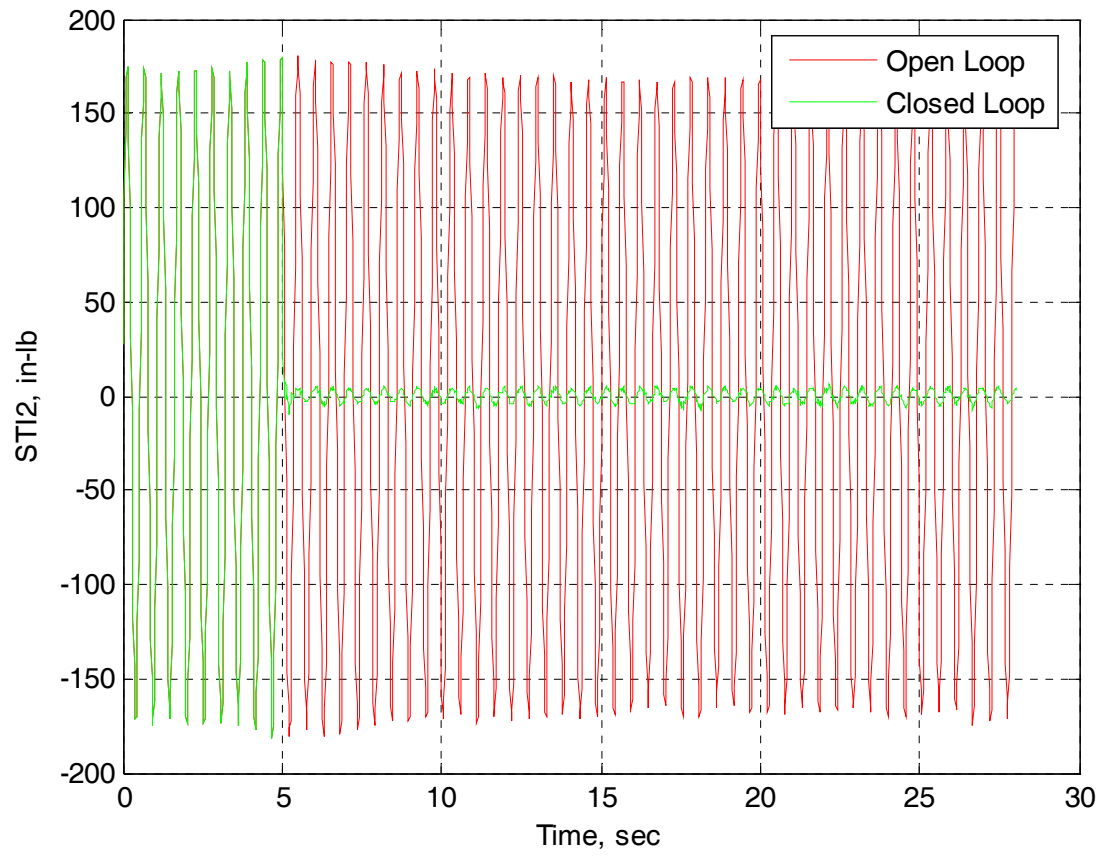


Figure 23.- Time histories of open- and closed-loop torsional moment (STI2) during gust excitation at 2 Hz. Embedded feedforward.

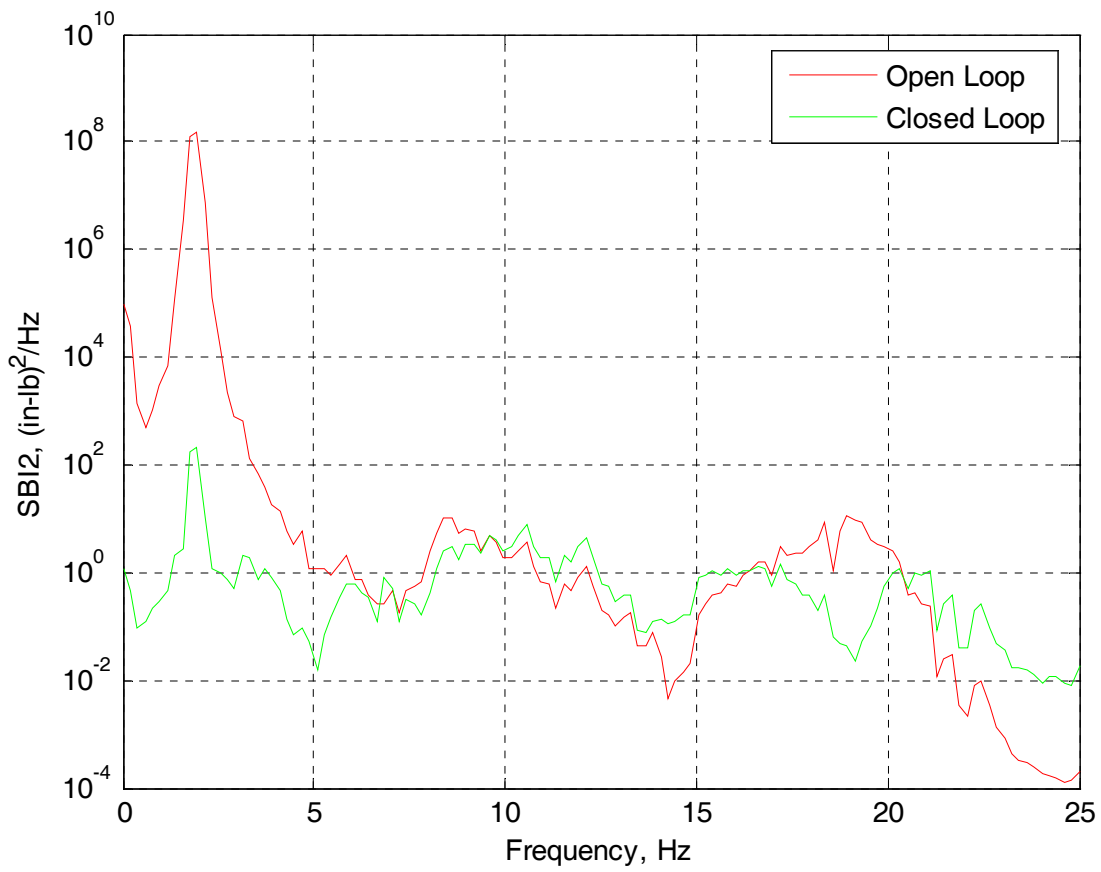


Figure 24.- Open- and closed-loop power spectral densities for vertical bending moment (SBI2) during gust excitation at 2 Hz. Embedded feedforward.

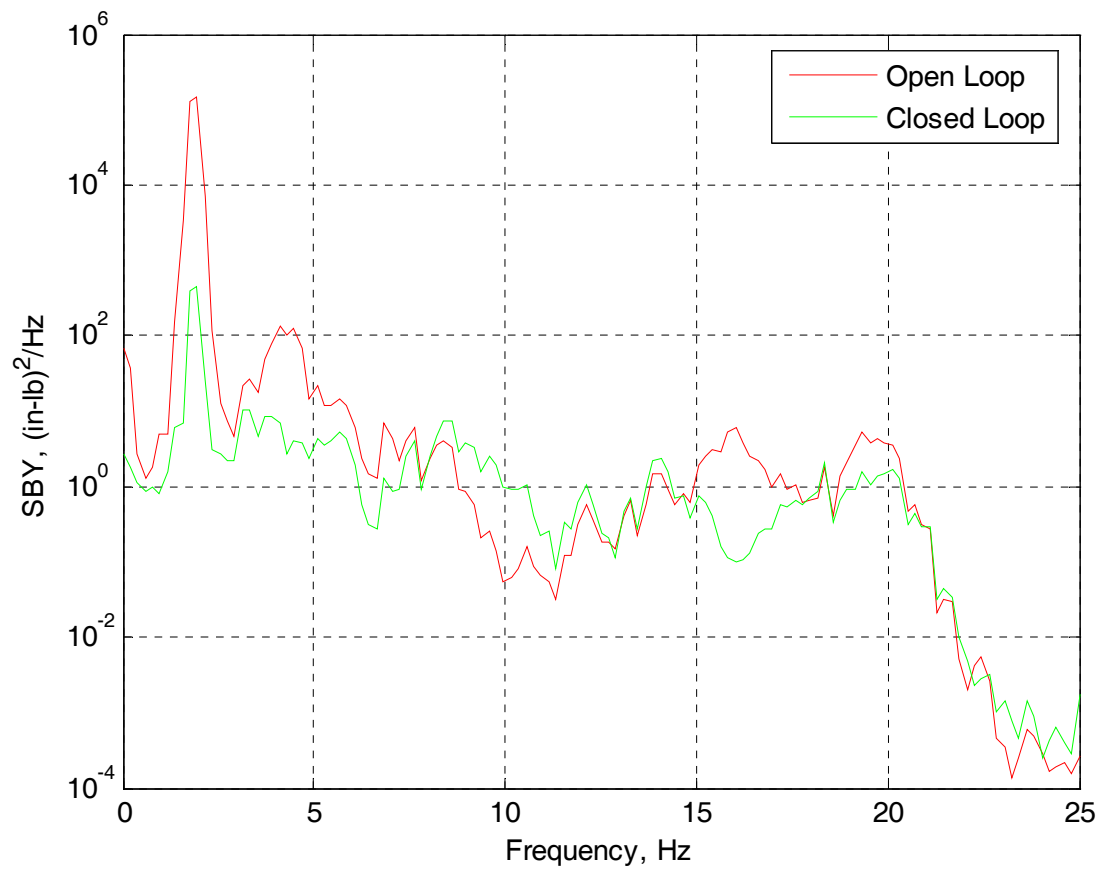


Figure 25.- Open- and closed-loop power spectral densities for fore-and-aft bending moment (SBY) during gust excitation at 2 Hz. Embedded feedforward.

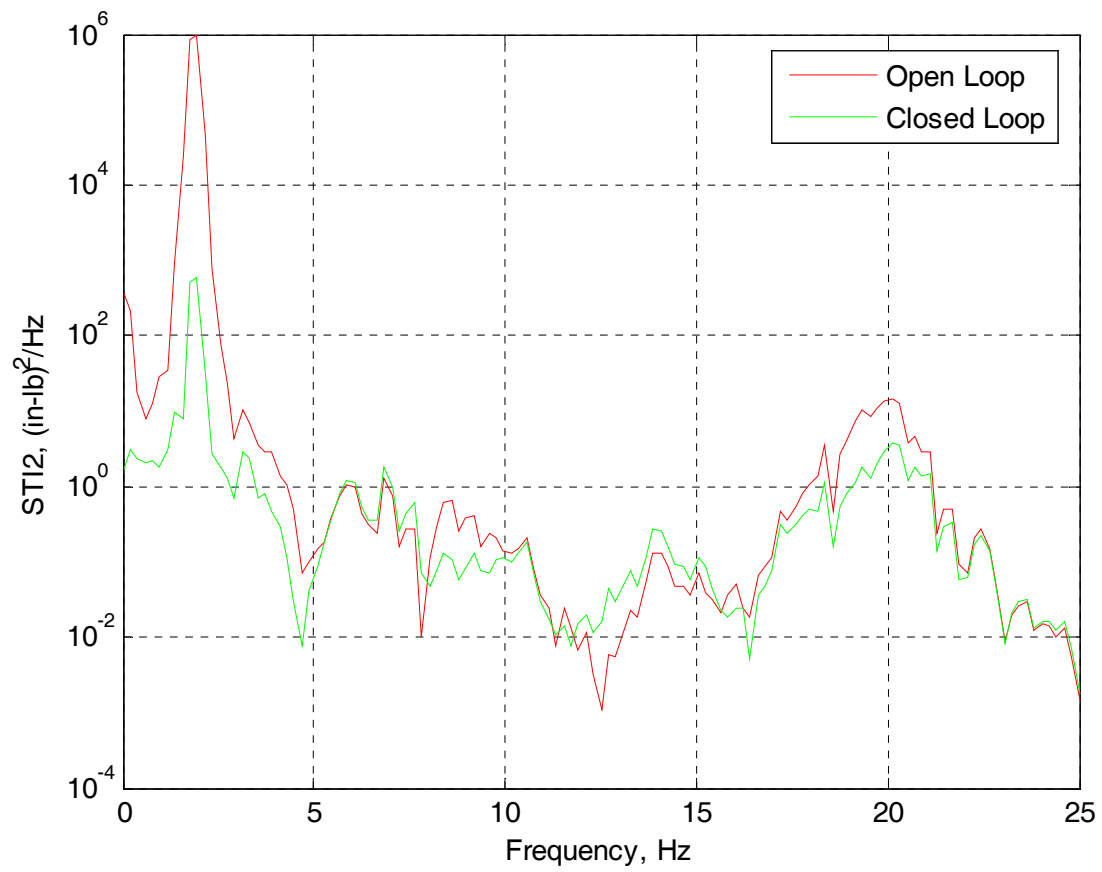


Figure 26.- Open- and closed-loop power spectral densities for torsional moment (STI2) during gust excitation at 2 Hz. Embedded feedforward.

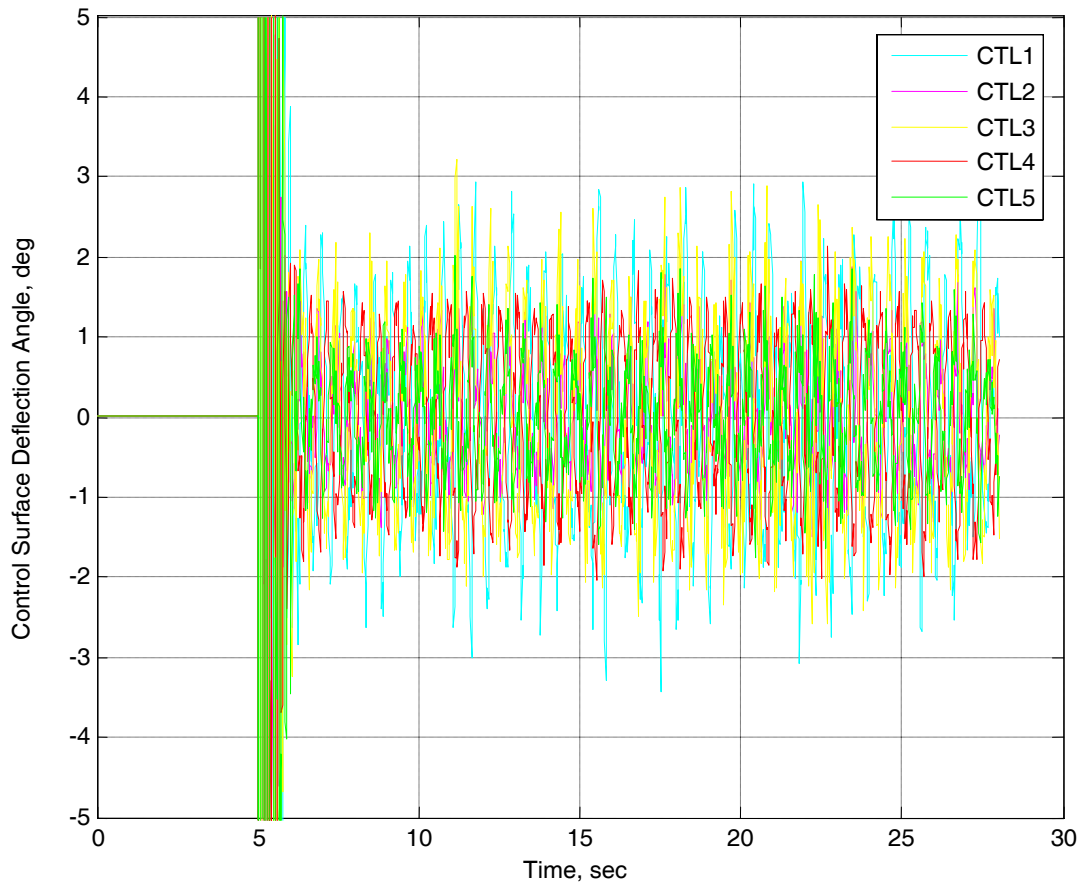


Figure 27.- Time histories of closed-loop control inputs (CTL1-CTL5) during gust excitation at 2 Hz. Embedded feedforward.

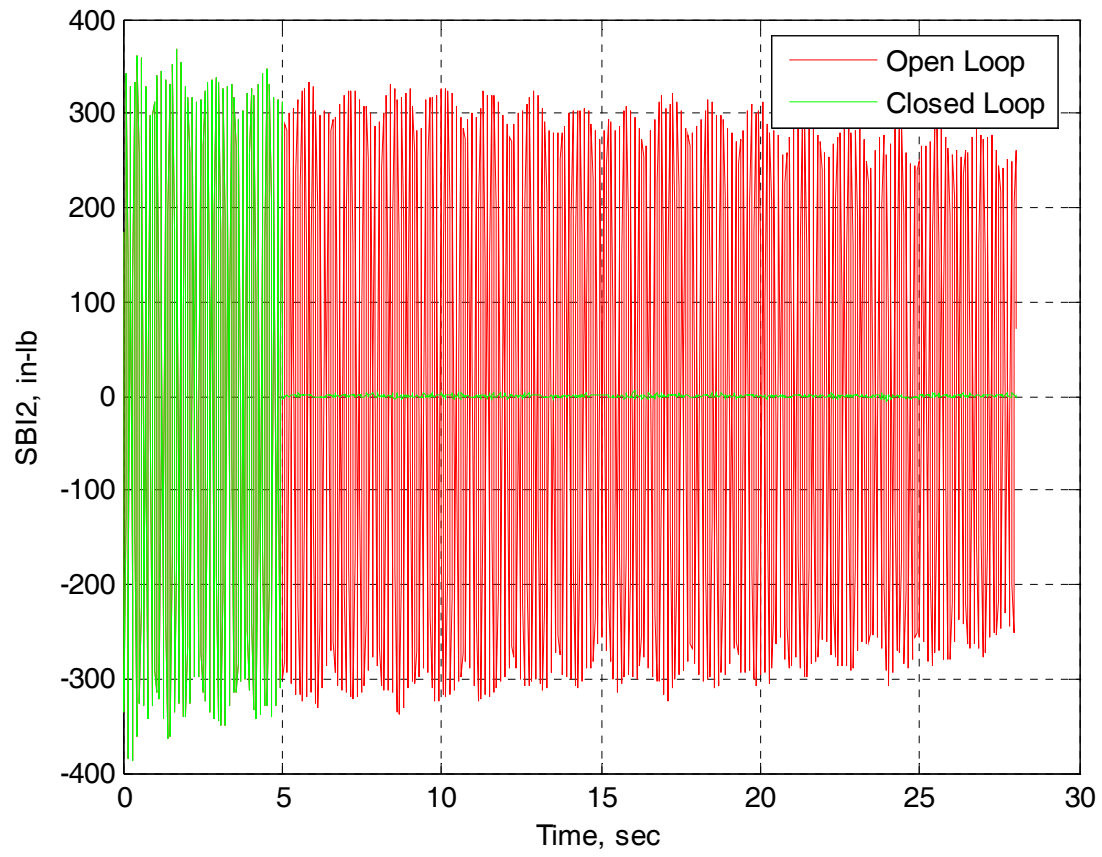


Figure 28.- Time histories of open- and closed-loop vertical bending moment (SBI2) during gust excitation at 8 Hz. Embedded feedforward.

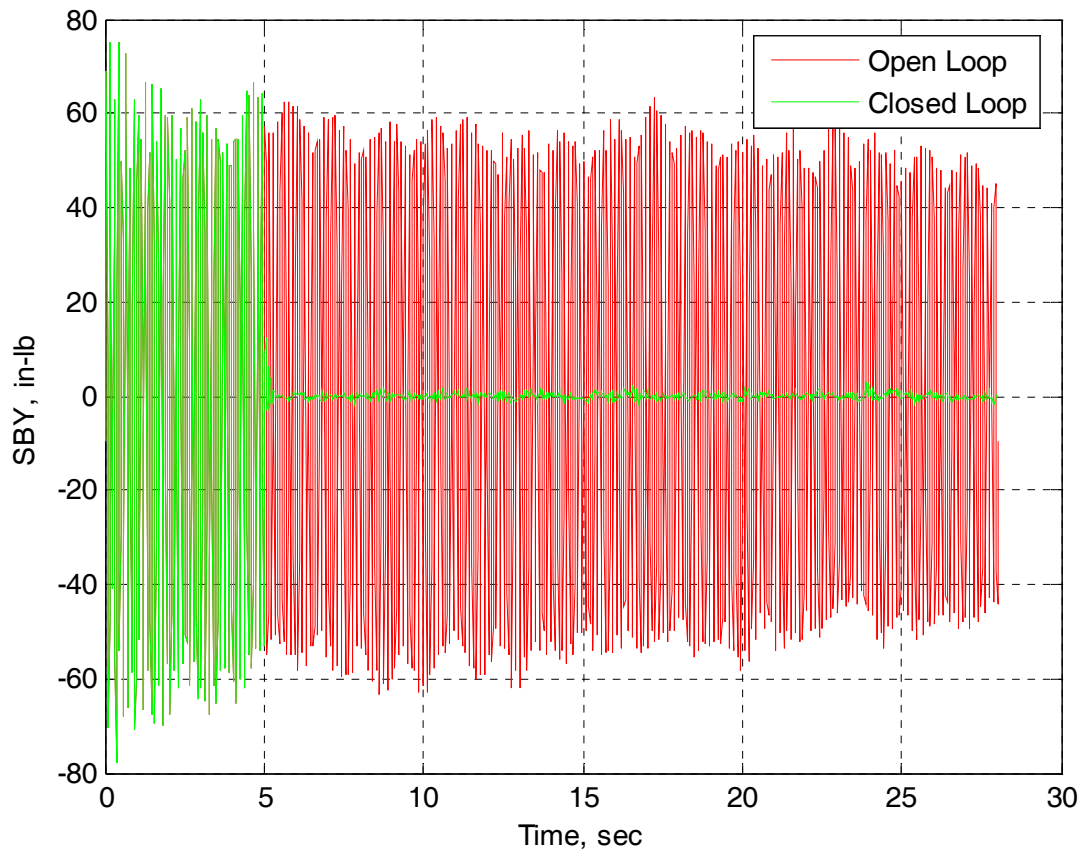


Figure 29.- Time histories of open- and closed-loop fore-and-aft bending moment (SBY) during gust excitation at 8 Hz. Embedded feedforward.

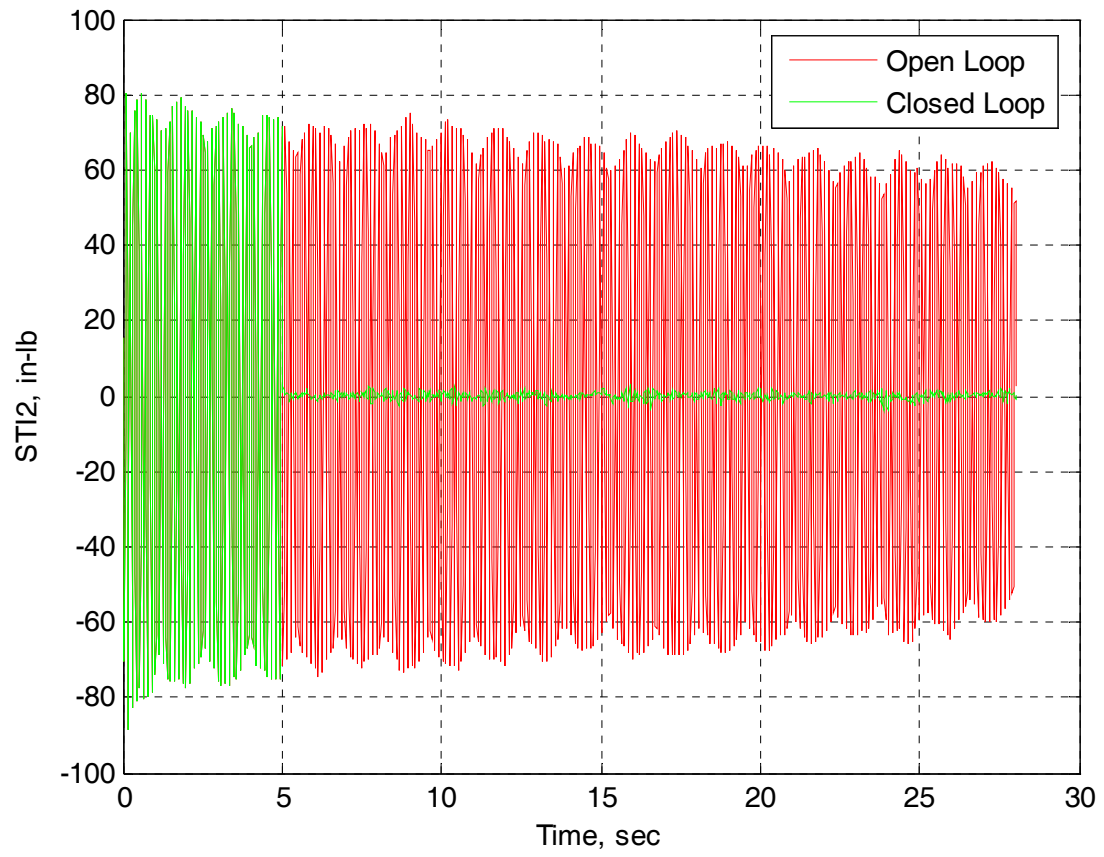


Figure 30.- Time histories of open- and closed-loop torsional moment (STI2) during gust excitation at 8 Hz. Embedded feedforward.

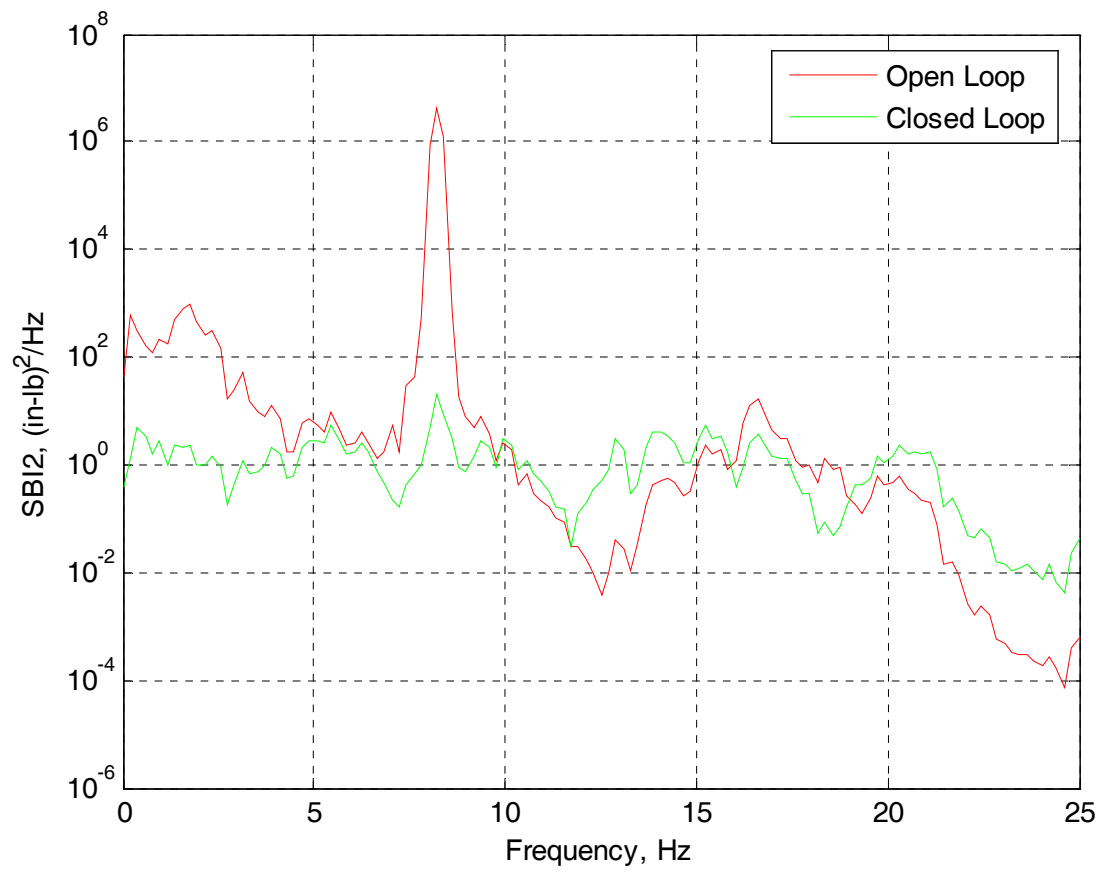


Figure 31.- Open- and closed-loop power spectral densities for vertical bending moment (SBI2) during gust excitation at 8 Hz. Embedded feedforward.

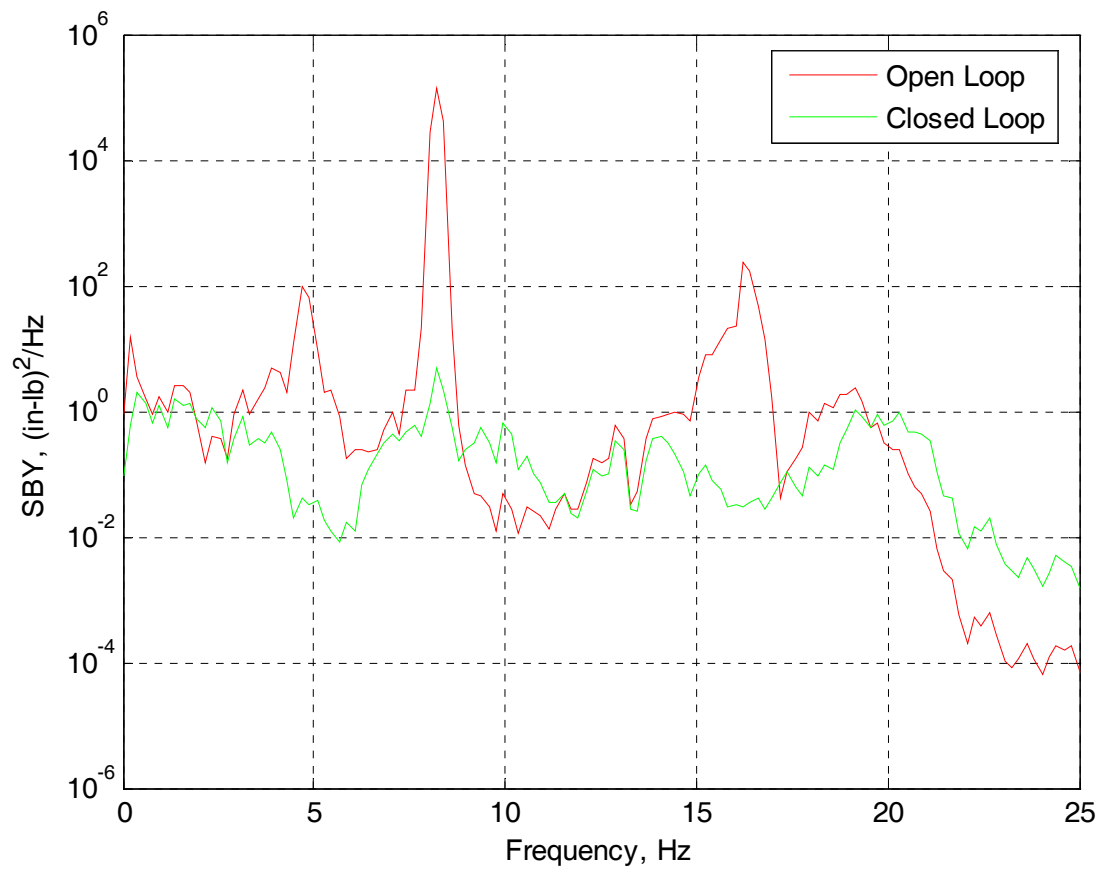


Figure 32.- Open- and closed-loop power spectral densities for fore-and-aft bending moment (SBY) during gust excitation at 8 Hz. Embedded feedforward.

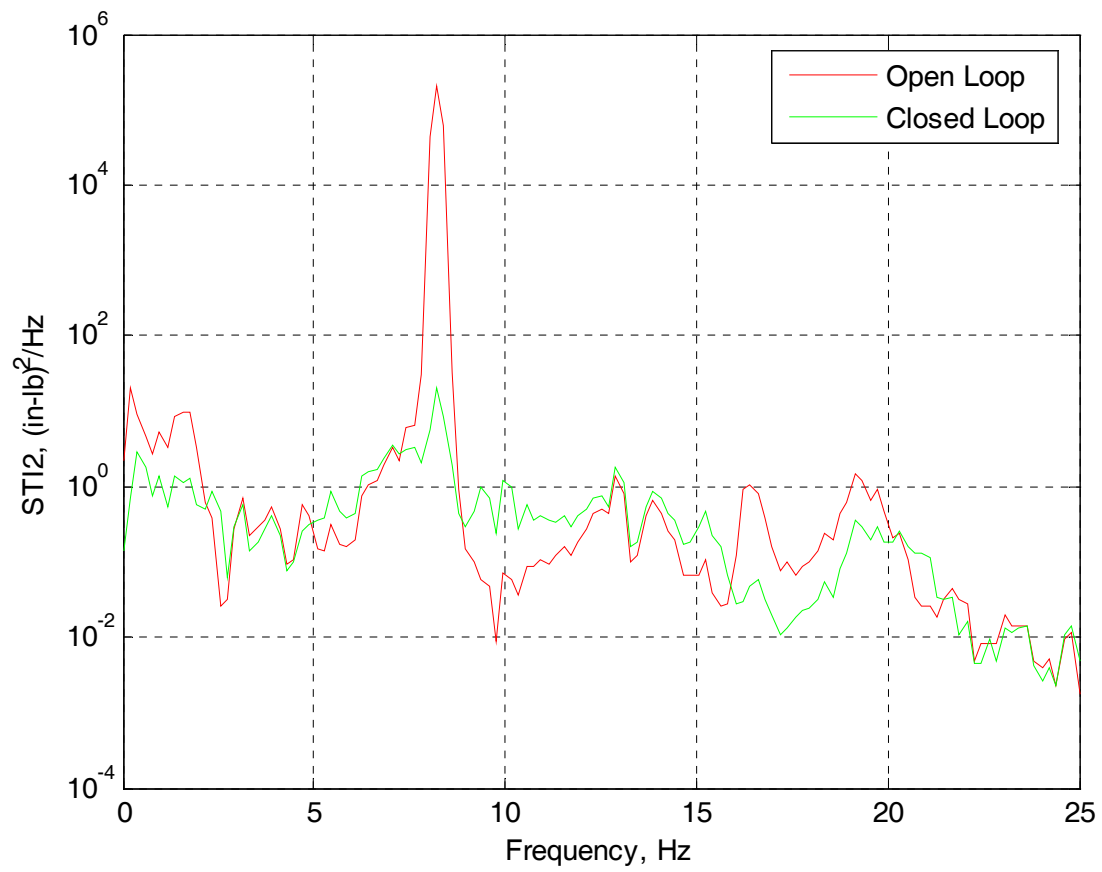


Figure 33.- Open- and closed-loop power spectral densities for torsional moment (STI2) during gust excitation at 8 Hz. Embedded feedforward.

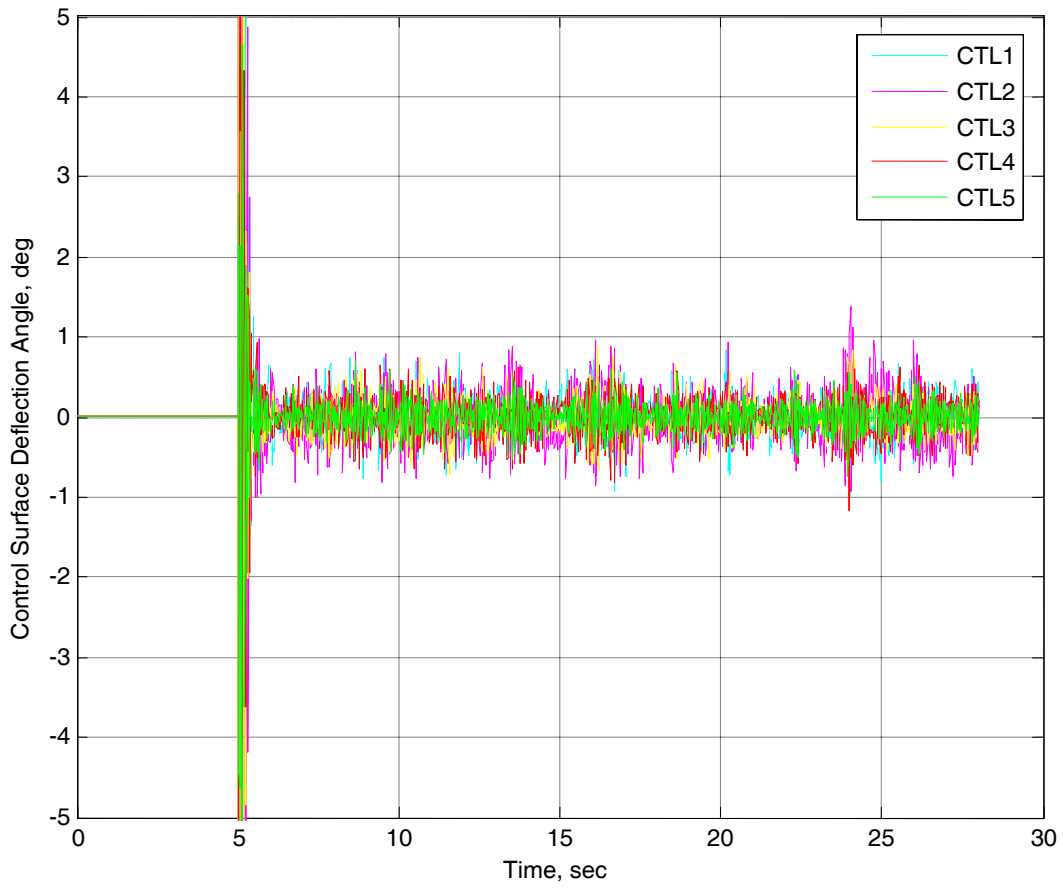


Figure 34.- Time histories of closed-loop control inputs (CTL1-CTL5) during gust excitation at 8 Hz. Embedded feedforward.

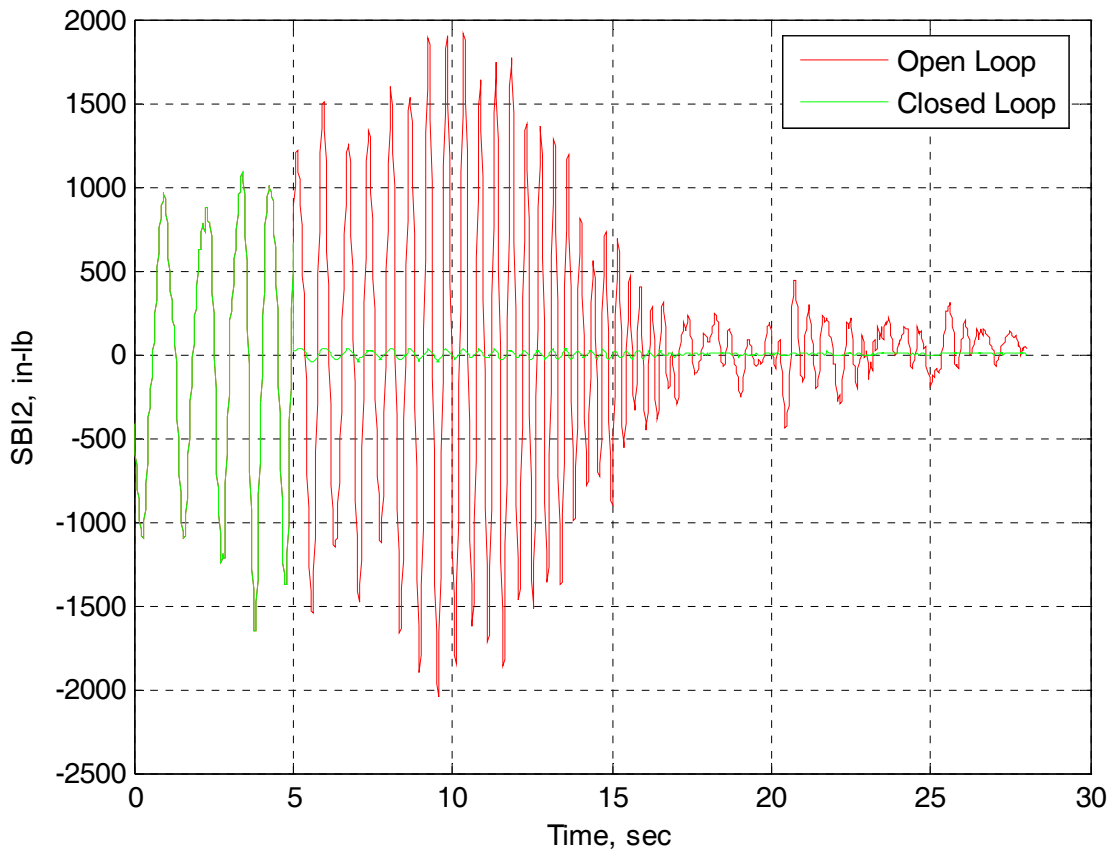


Figure 35.- Time histories of open- and closed-loop vertical bending moment (SBI2) while sweeping gust frequency from 0.5 to 10 Hz. Embedded feedforward.

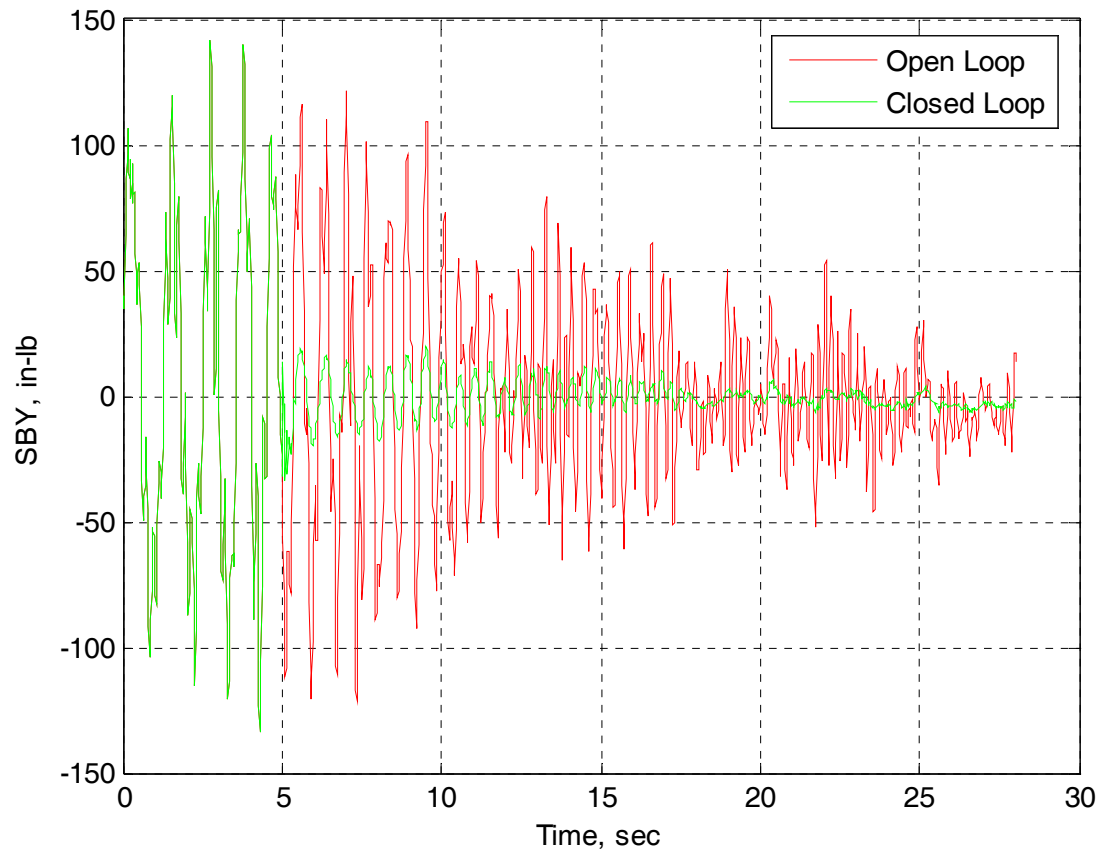


Figure 36.- Time histories of open- and closed-loop fore-and-aft bending moment (SBY) while sweeping gust frequency from 0.5 to 10 Hz. Embedded feedforward.

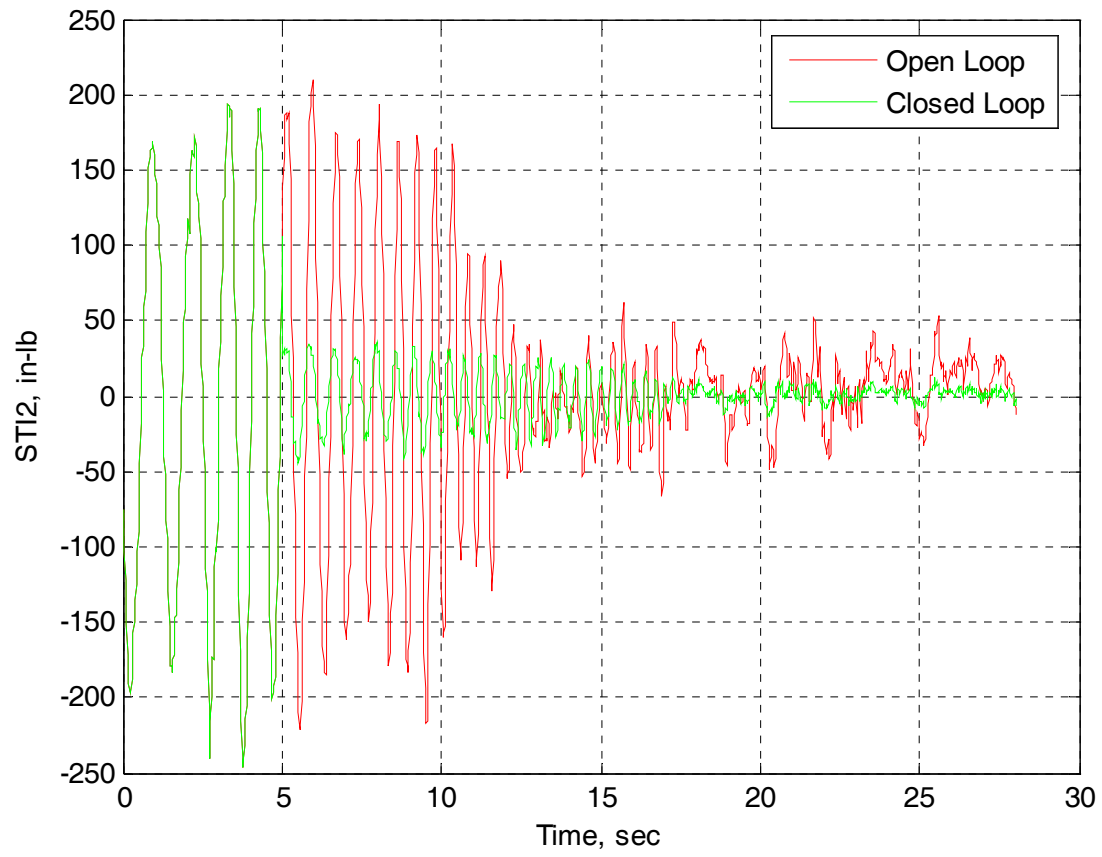


Figure 37.- Time histories of open- and closed-loop torsional moment (STI2) while sweeping gust frequency from 0.5 to 10 Hz. Embedded feedforward.

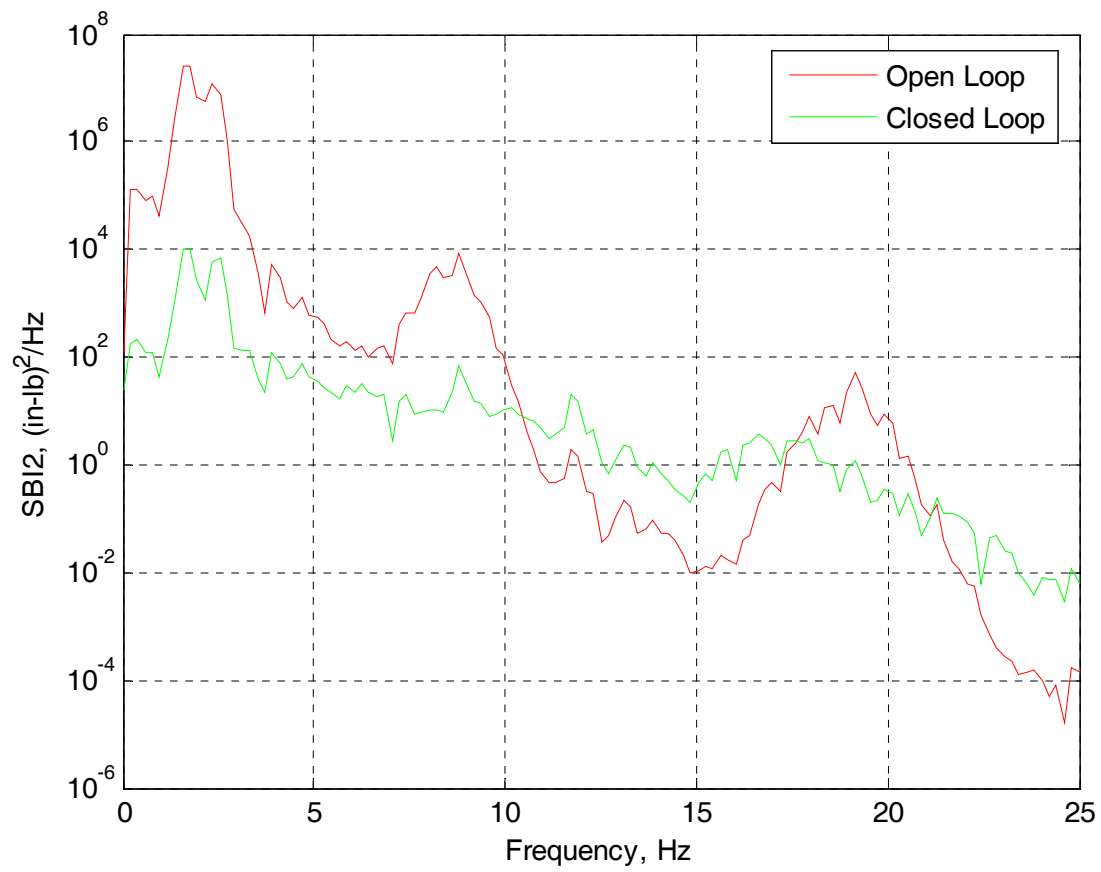


Figure 38.- Open- and closed-loop power spectral densities for vertical bending moment (SBI2) while sweeping gust frequency from 0.5 to 10 Hz. Embedded feedforward.

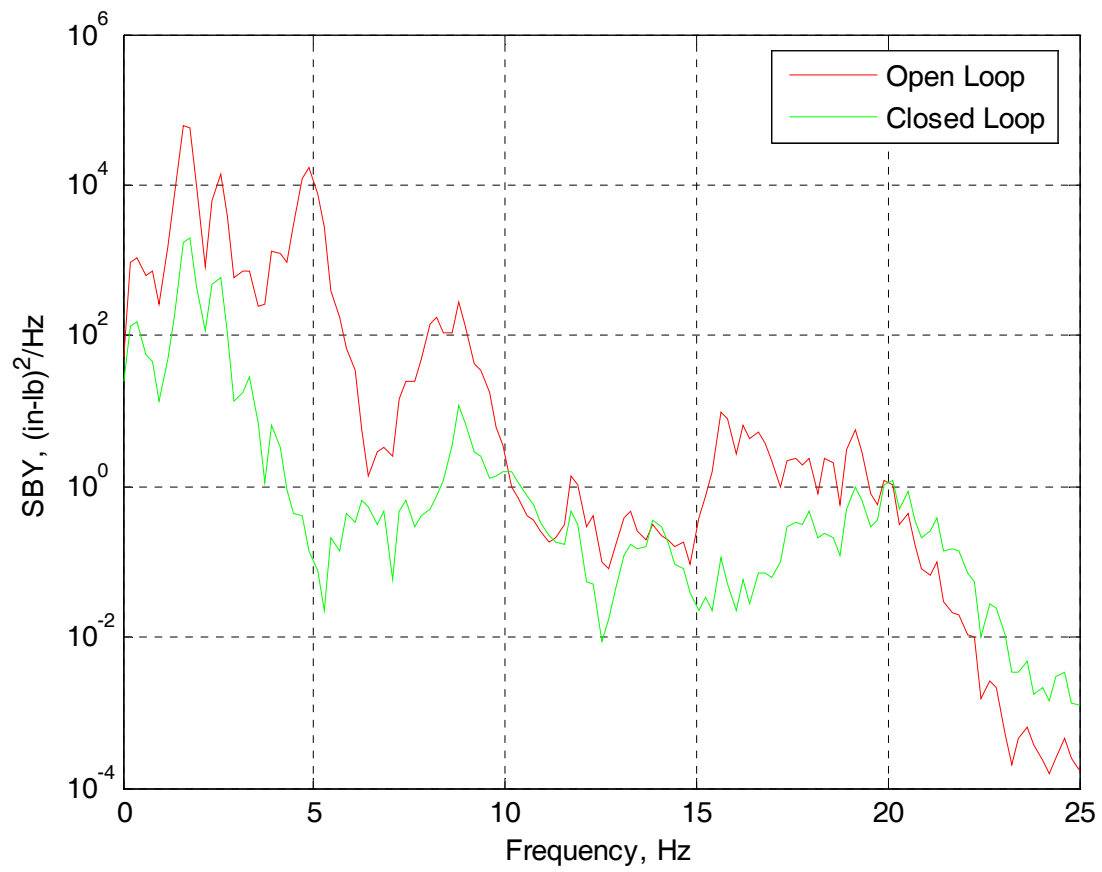


Figure 39.- Open- and closed-loop power spectral densities for fore-and-aft bending moment (SBY) while sweeping gust frequency from 0.5 to 10 Hz. Embedded feedforward.

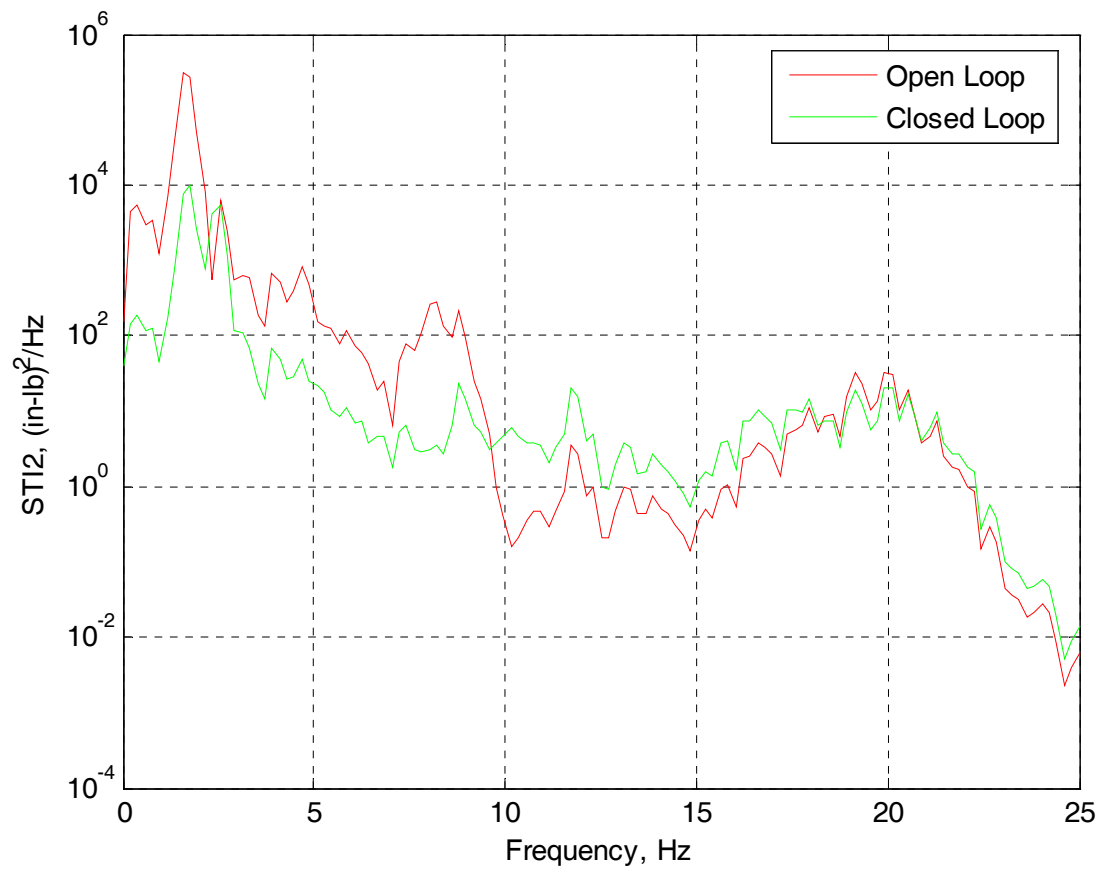


Figure 40.- Open- and closed-loop power spectral densities for torsional moment (STI2) while sweeping gust frequency from 0.5 to 10 Hz. Embedded feedforward.

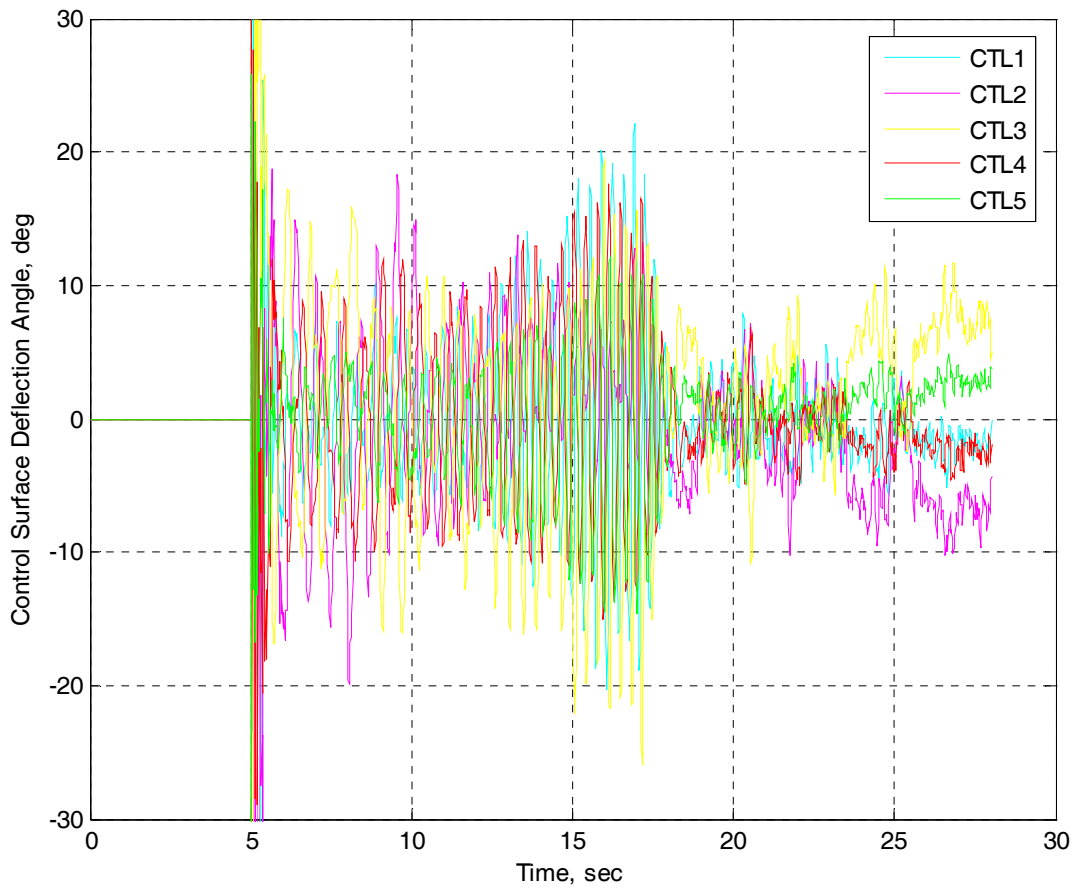


Figure 41.- Time histories of closed-loop control inputs (CTL1-CTL5) while sweeping gust frequency from 0.5 to 10 Hz. Embedded feedforward.

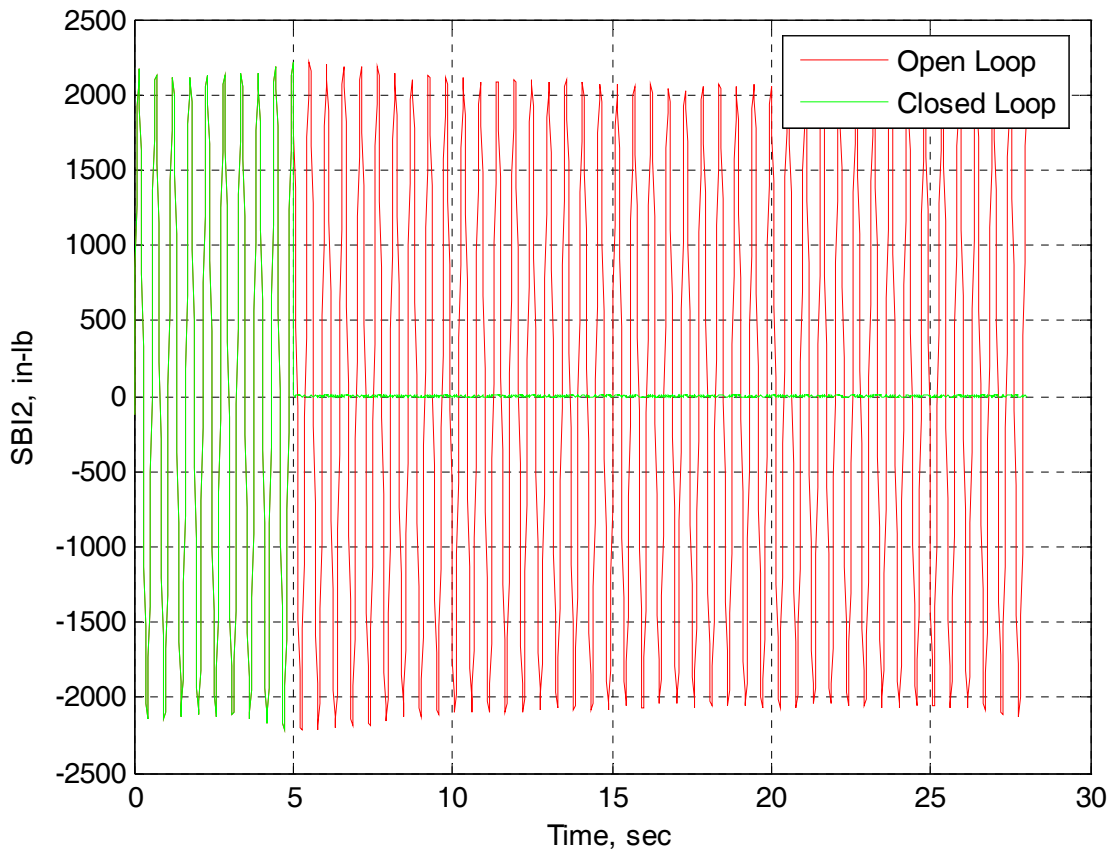


Figure 42.- Time histories of open- and closed-loop vertical bending moment (SBI2) during gust excitation at 2 Hz. Explicit feedforward.

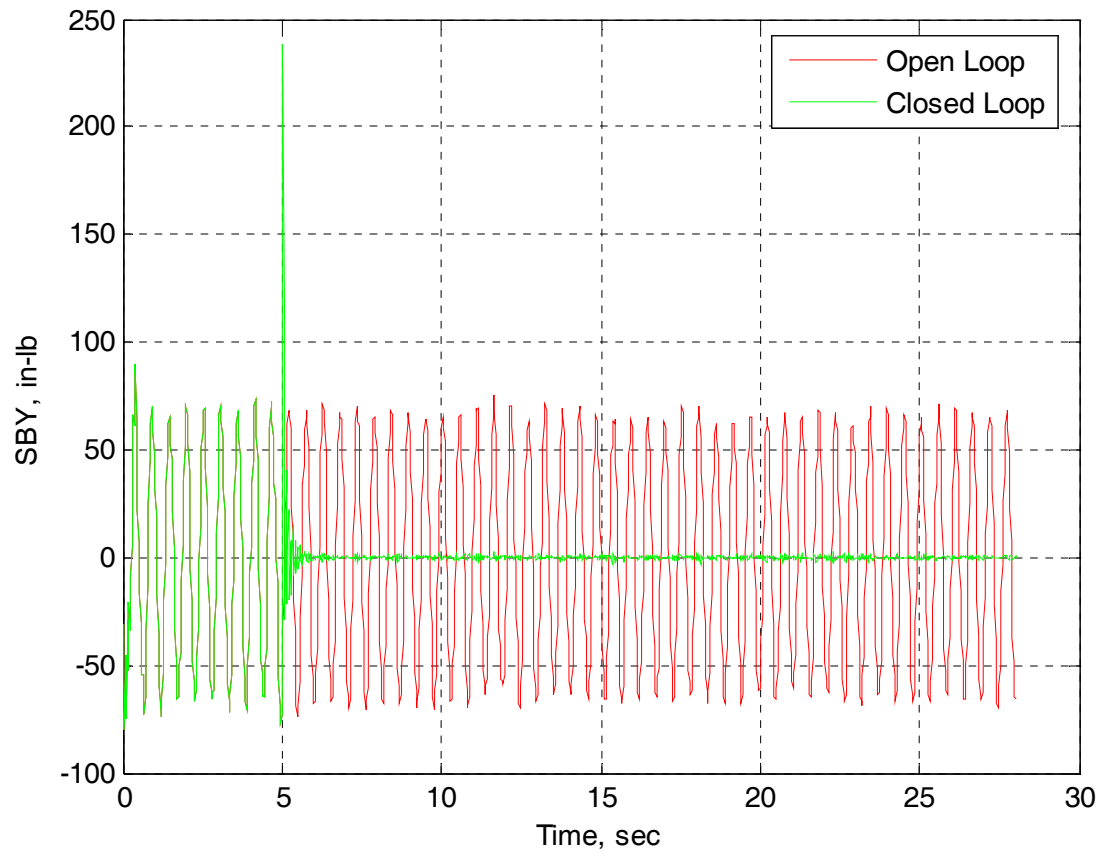


Figure 43.- Time histories of open- and closed-loop fore-and-aft bending moment (SBY) during gust excitation at 2 Hz. Explicit feedforward.

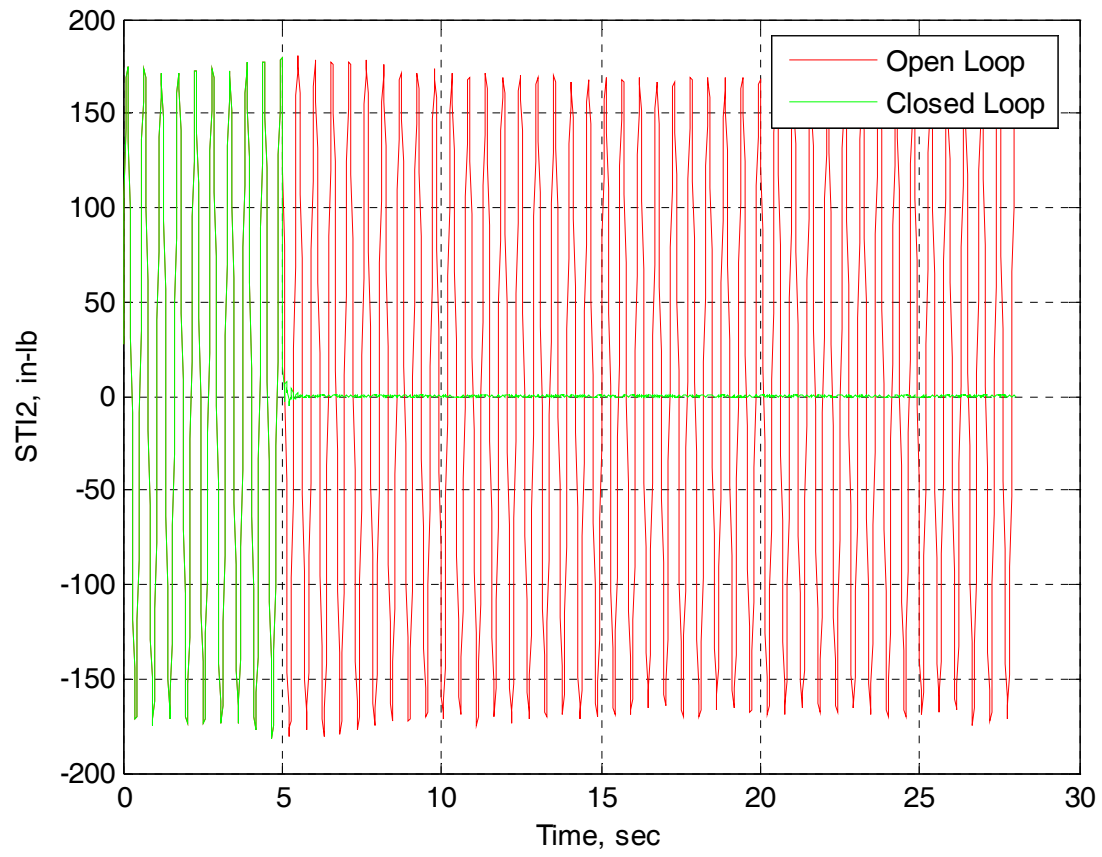


Figure 44.- Time histories of open- and closed-loop torsional moment (STI2) during gust excitation at 2 Hz. Explicit feedforward.

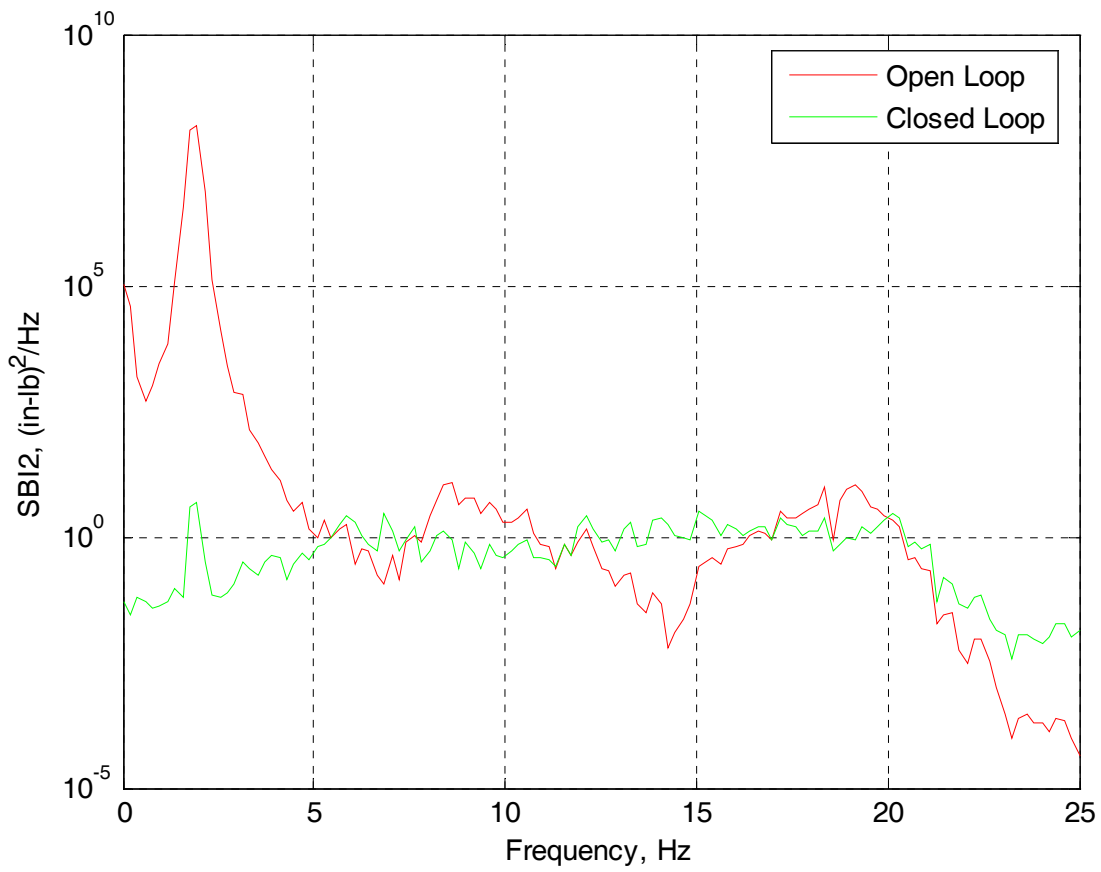


Figure 45.- Open- and closed-loop power spectral densities for vertical bending moment (SBI2) during gust excitation at 2 Hz. Explicit feedforward.

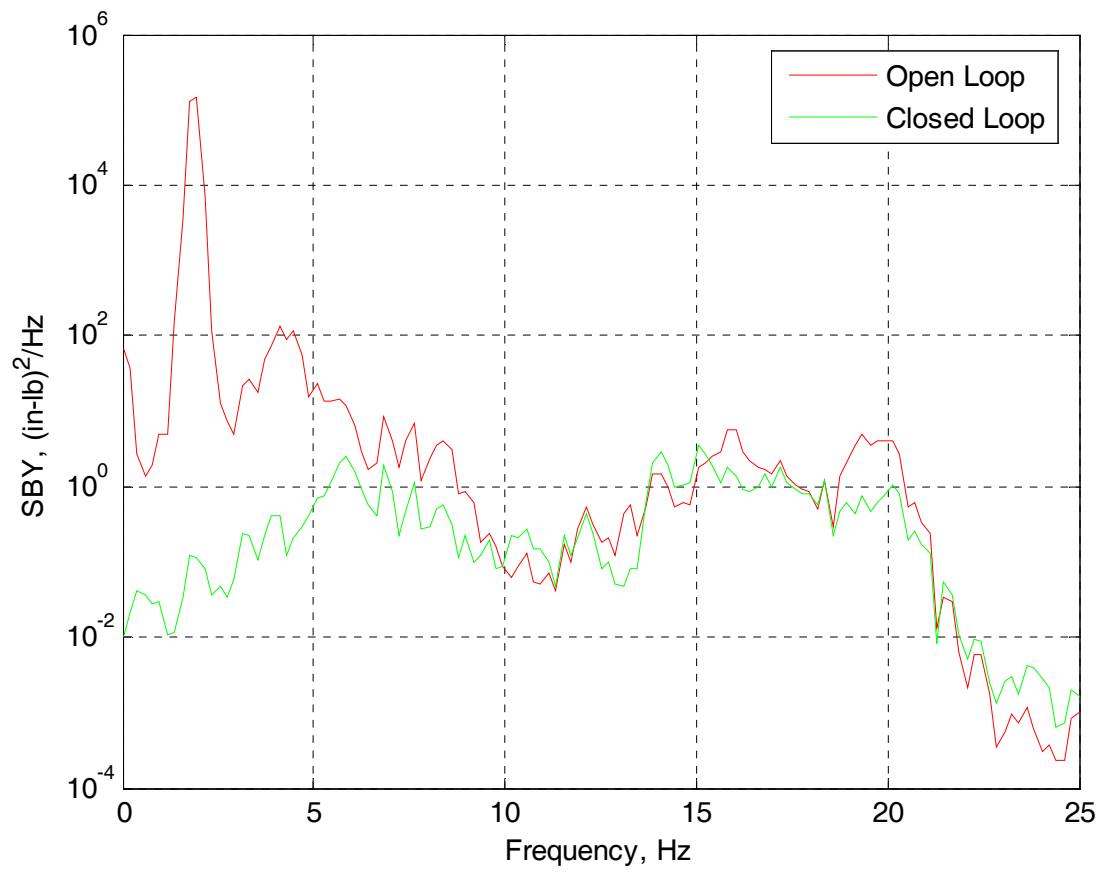


Figure 46.- Open- and closed-loop power spectral densities for fore-and-aft bending moment (SBY) during gust excitation at 2 Hz. Explicit feedforward.

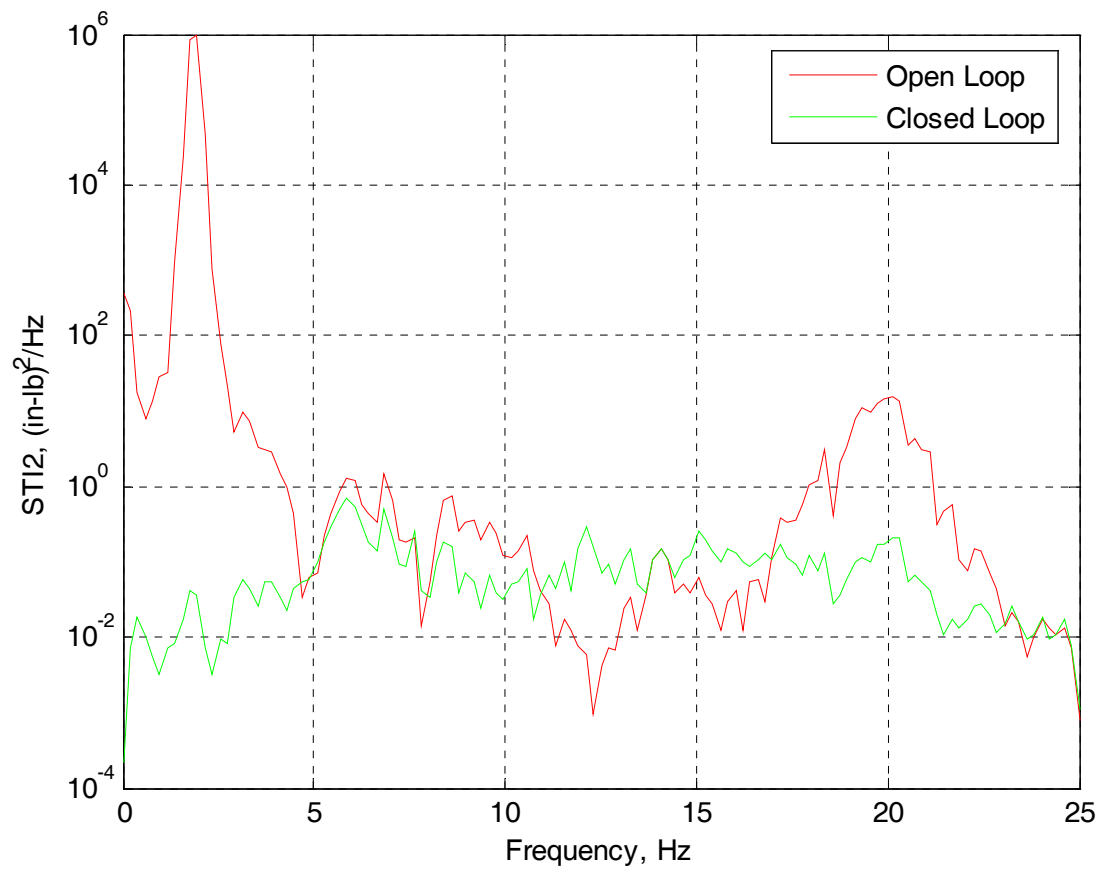


Figure 47.- Open- and closed-loop power spectral densities for torsional moment (STI2) during gust excitation at 2 Hz. Explicit feedforward.

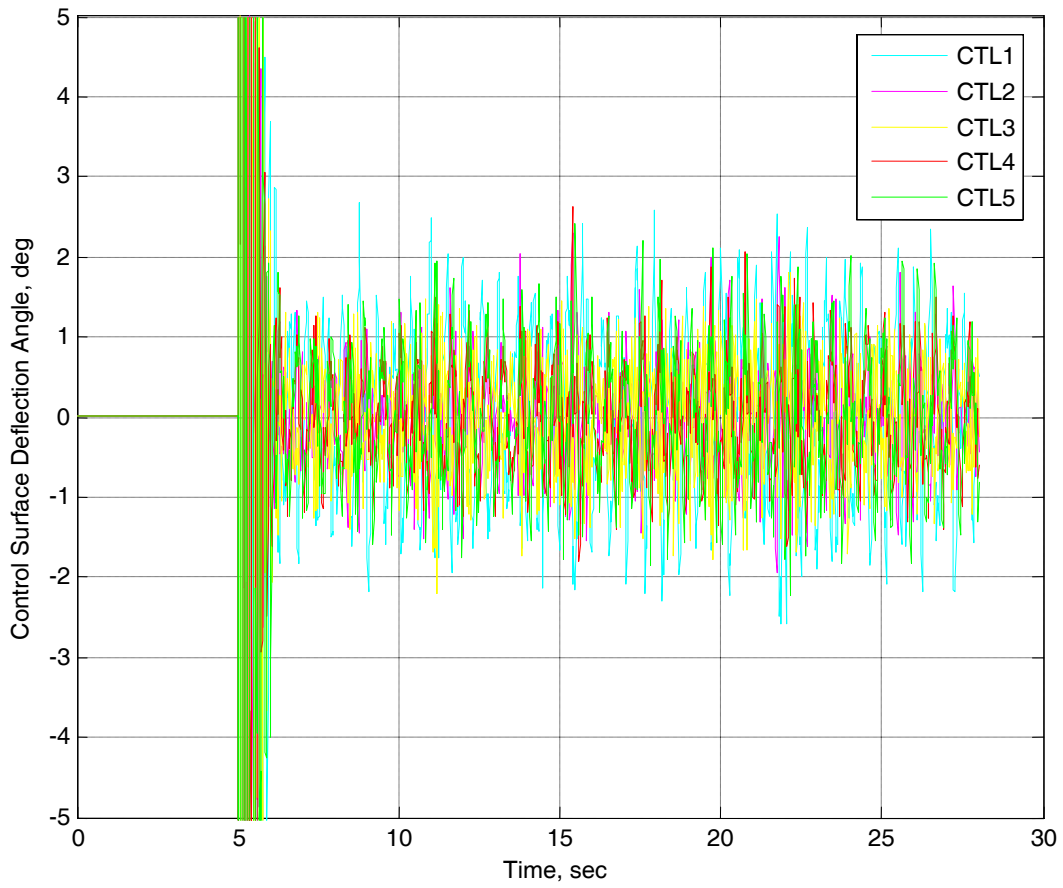


Figure 48.- Time histories of closed-loop control inputs (CTL1-CTL5) during gust excitation at 2 Hz. Explicit feedforward.

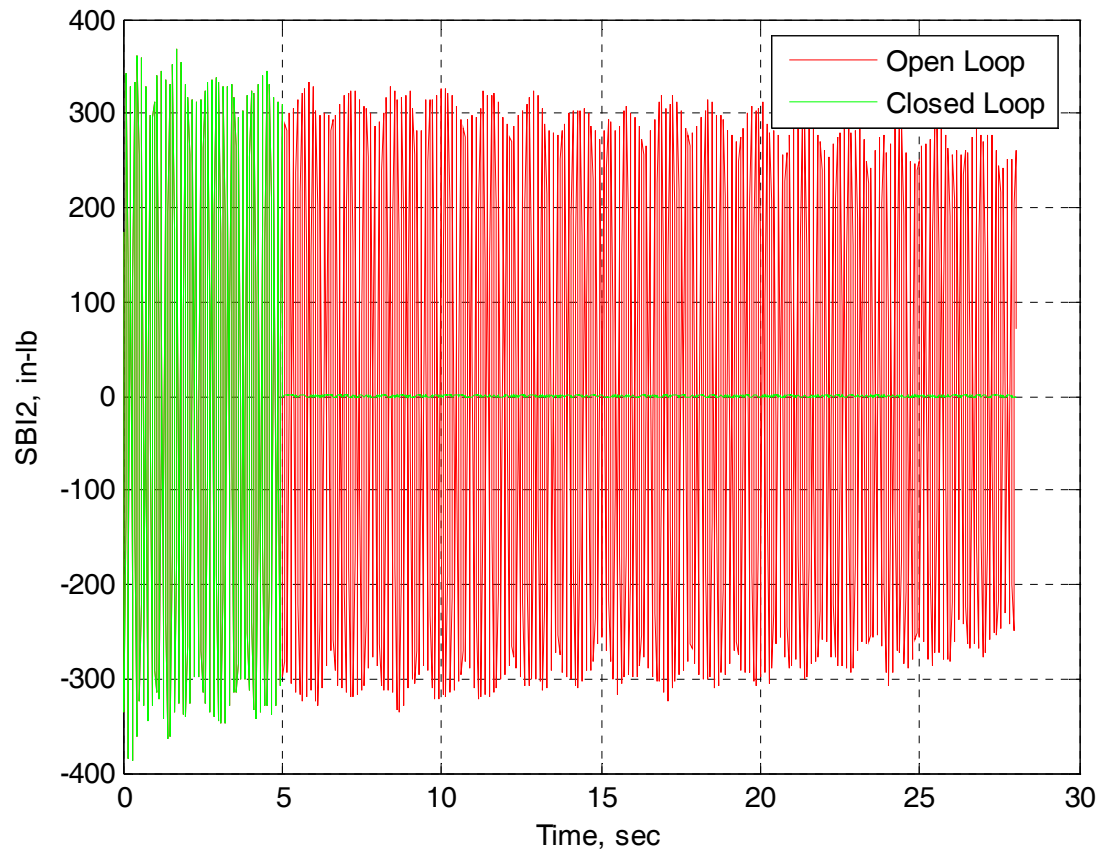


Figure 49.- Time histories of open- and closed-loop vertical bending moment (SBI2) during gust excitation at 8 Hz. Explicit feedforward.

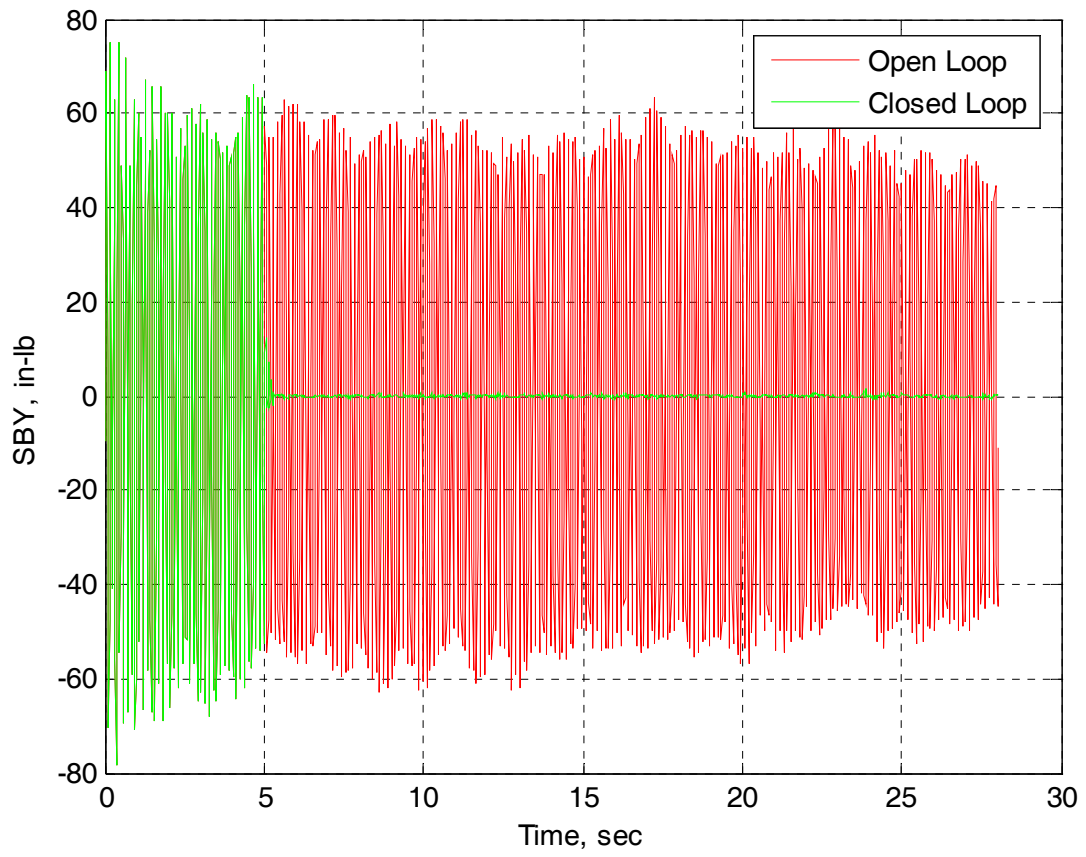


Figure 50.- Time histories of open- and closed-loop fore-and-aft bending moment (SBY) during gust excitation at 8 Hz. Explicit feedforward.

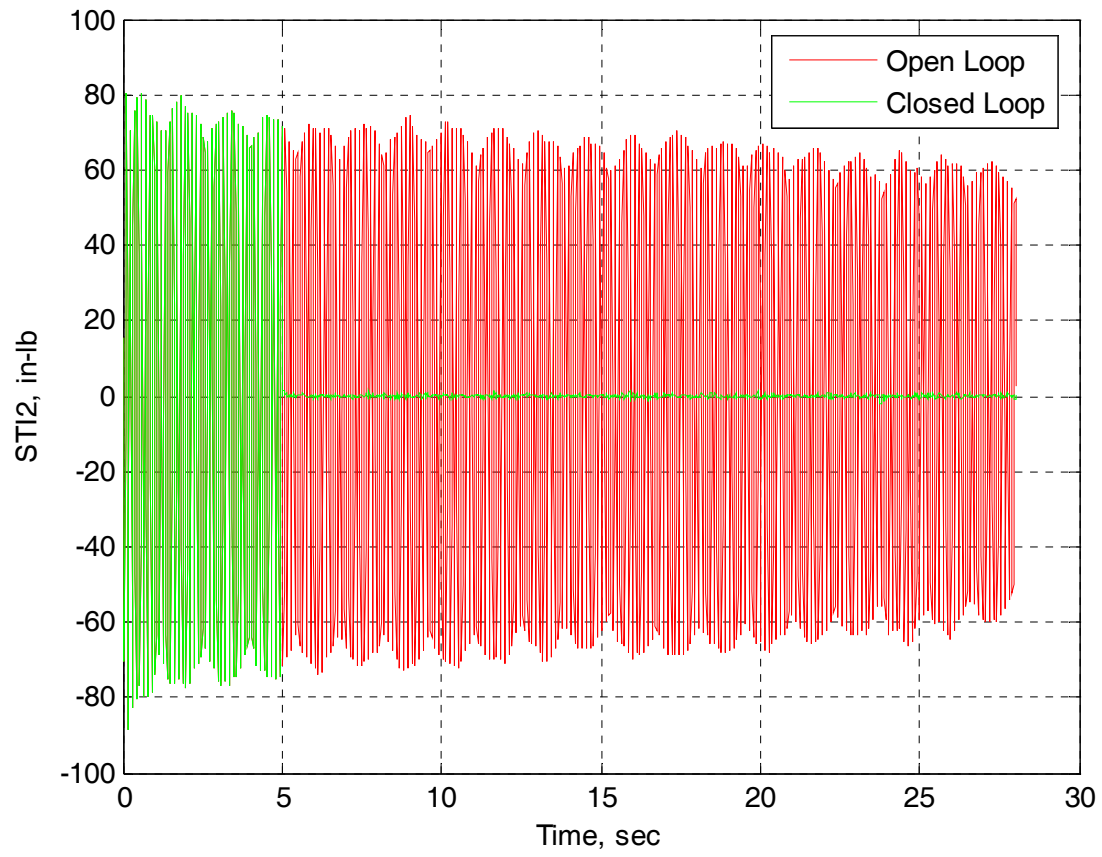


Figure 51.- Time histories of open- and closed-loop torsional moment (STI2) during gust excitation at 8 Hz. Explicit feedforward.

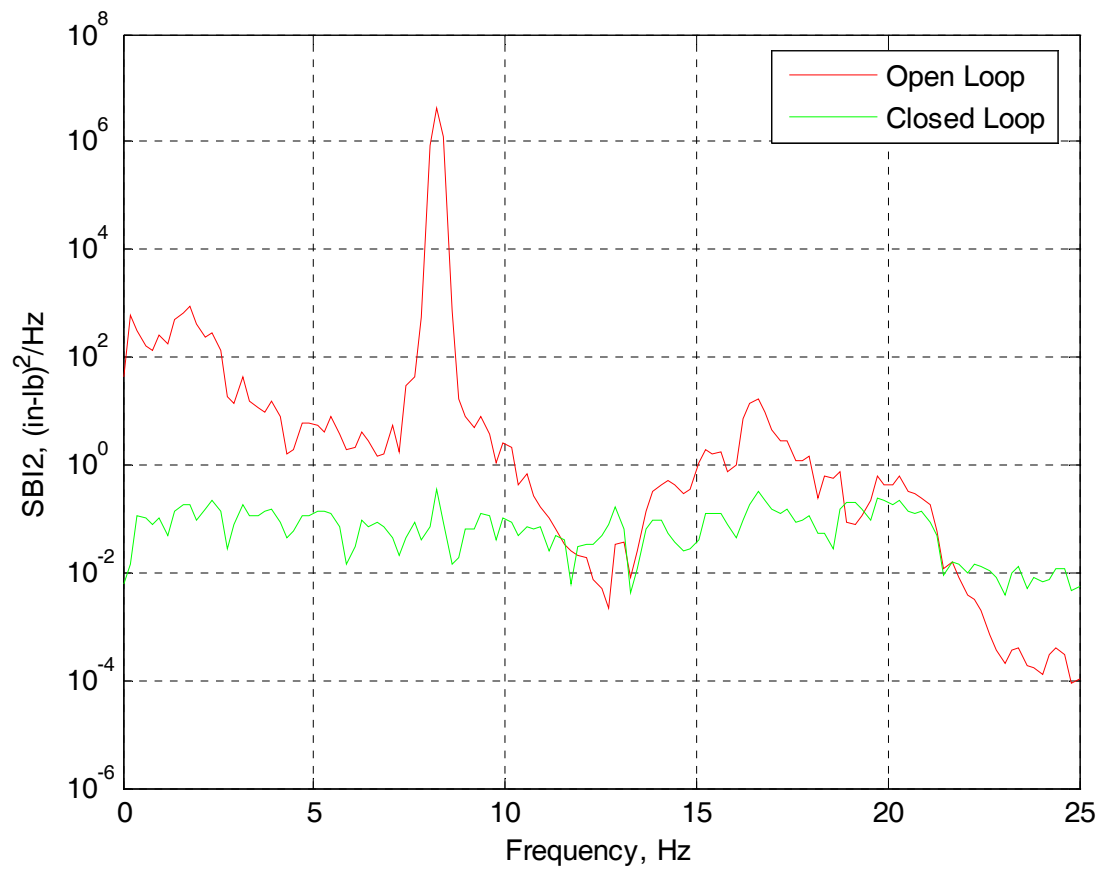


Figure 52.- Open- and closed-loop power spectral densities for vertical bending moment (SBI2) during gust excitation at 8 Hz. Explicit feedforward.

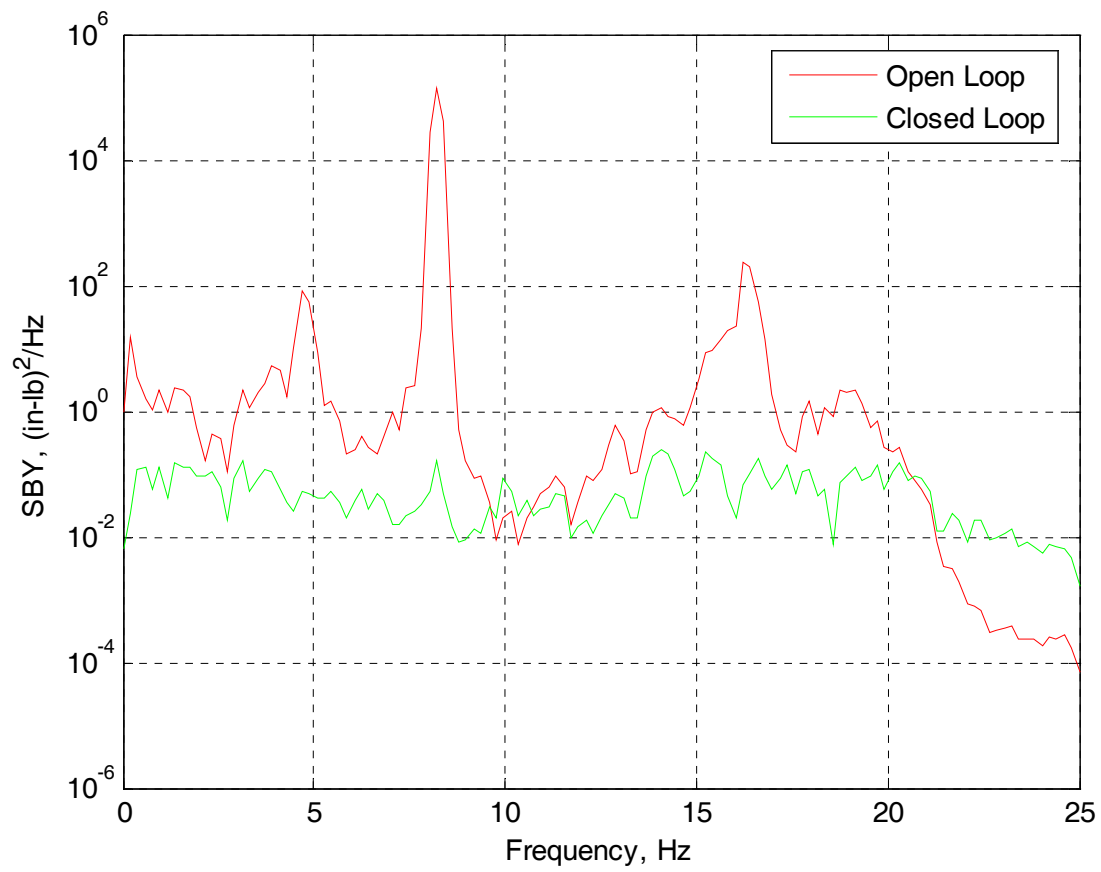


Figure 53.- Open- and closed-loop power spectral densities for fore-and-aft bending moment (SBY) during gust excitation at 8 Hz. Explicit feedforward.

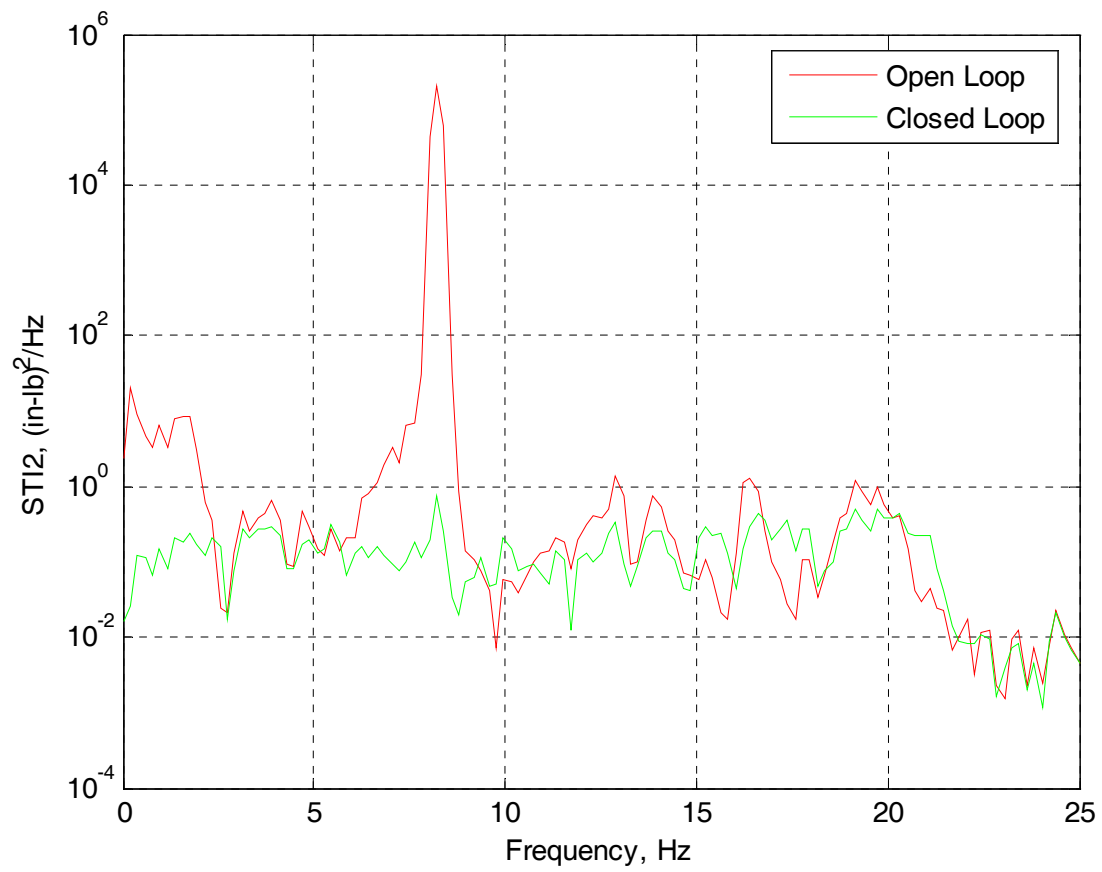


Figure 54.- Open- and closed-loop power spectral densities for torsional moment (STI2) during gust excitation at 8 Hz. Explicit feedforward.

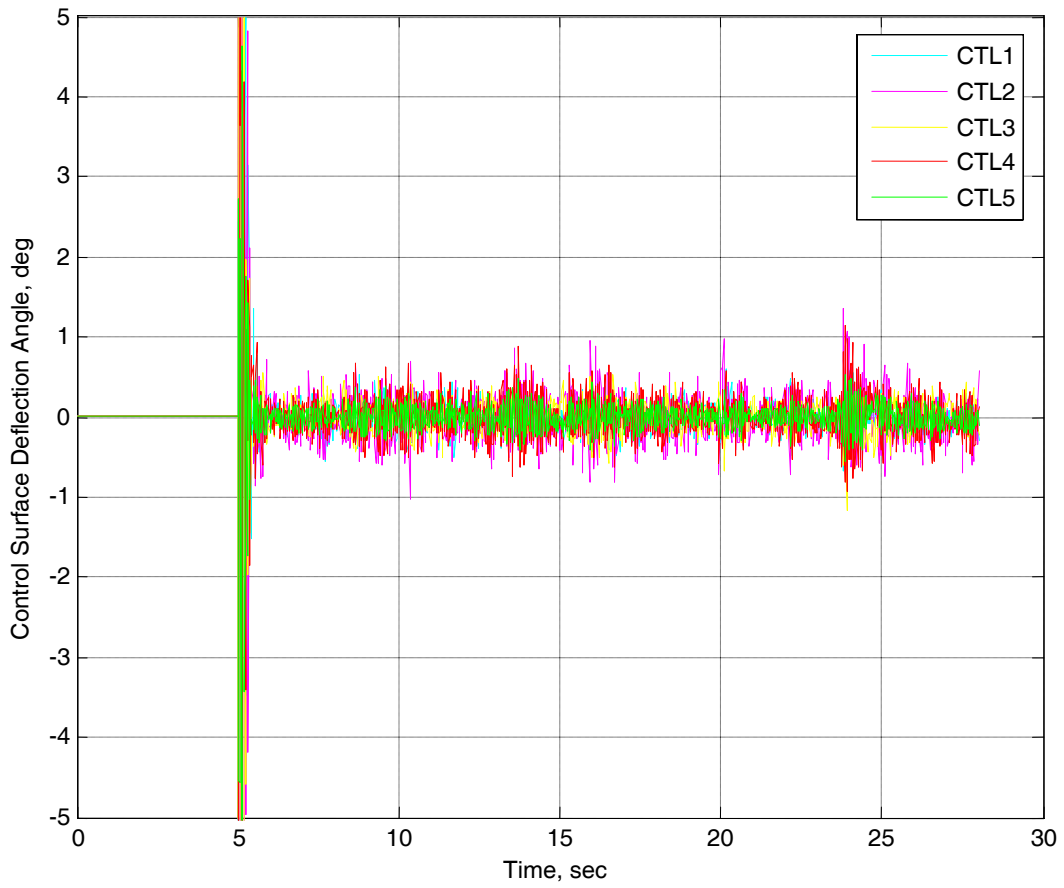


Figure 55.- Time histories of closed-loop control inputs (CTL1-CTL5) during gust excitation at 8 Hz. Explicit feedforward.

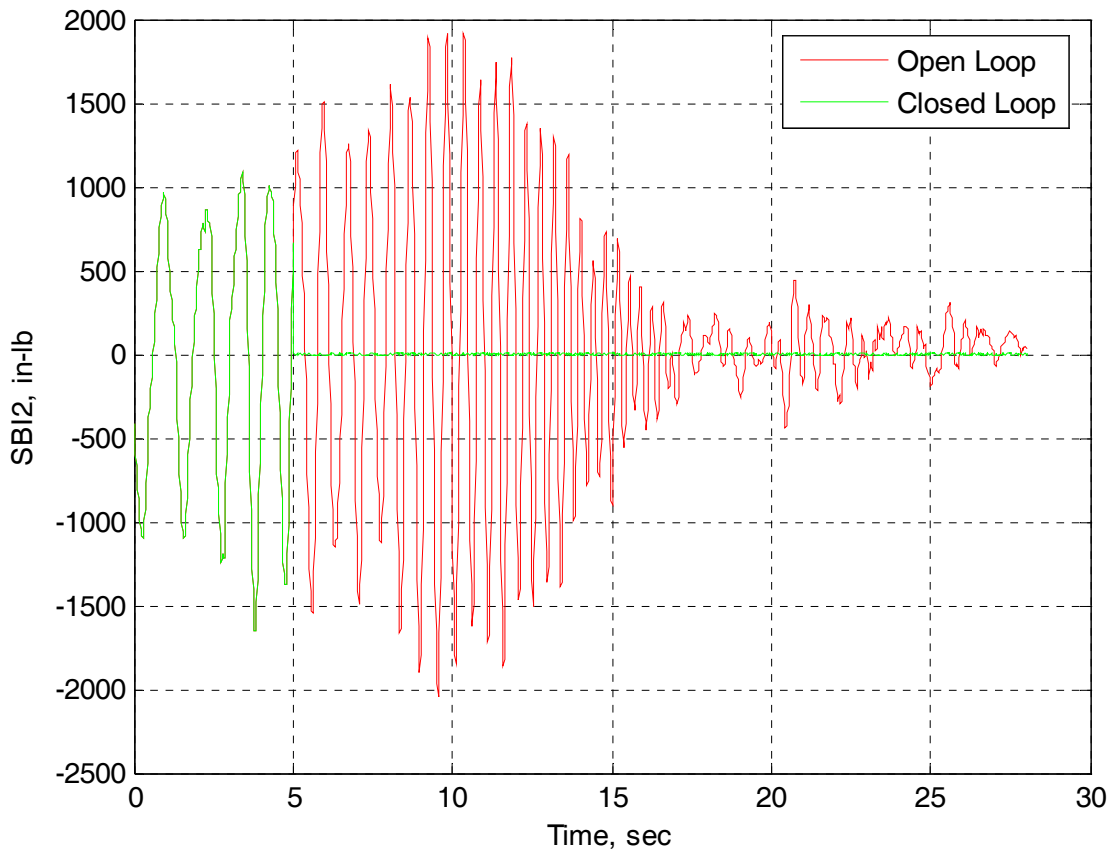


Figure 56.- Time histories of open- and closed-loop vertical bending moment (SBI2) while sweeping gust frequency from 0.5 to 10 Hz. Explicit feedforward.

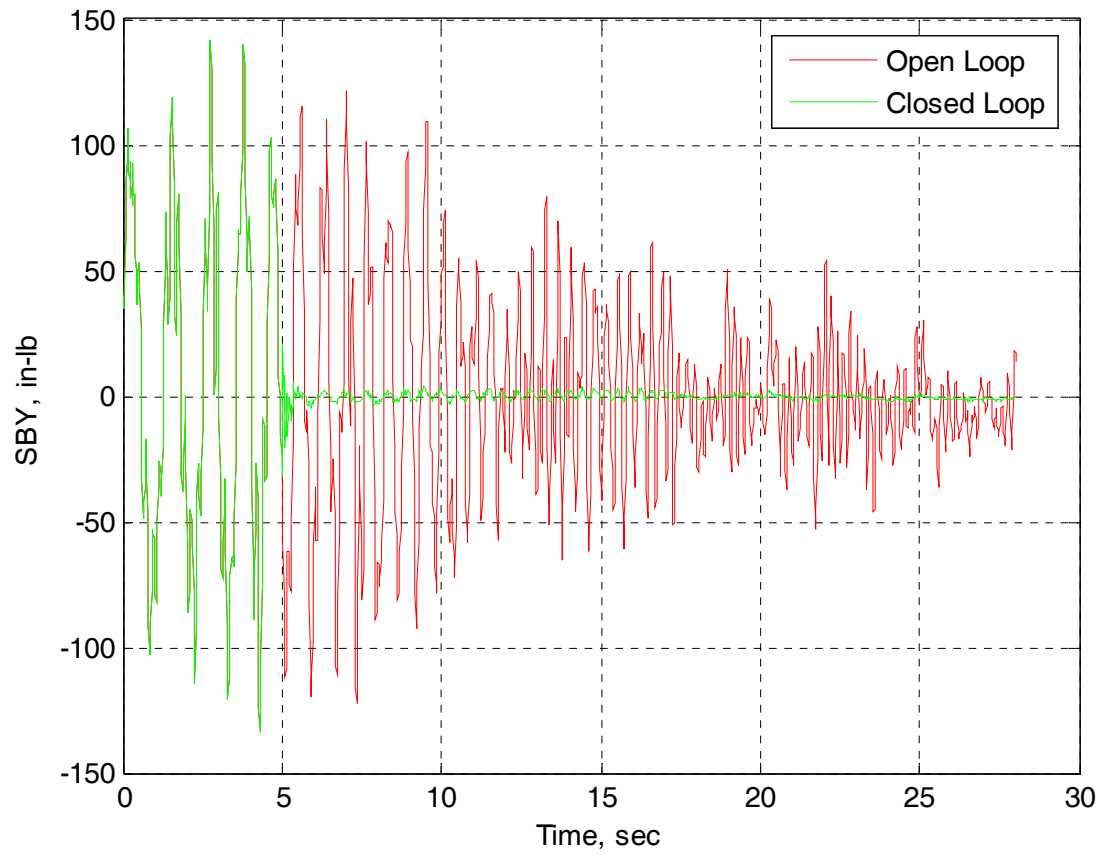


Figure 57.- Time histories of open- and closed-loop fore-and-aft bending moment (SBY) while sweeping gust frequency from 0.5 to 10 Hz. Explicit feedforward.

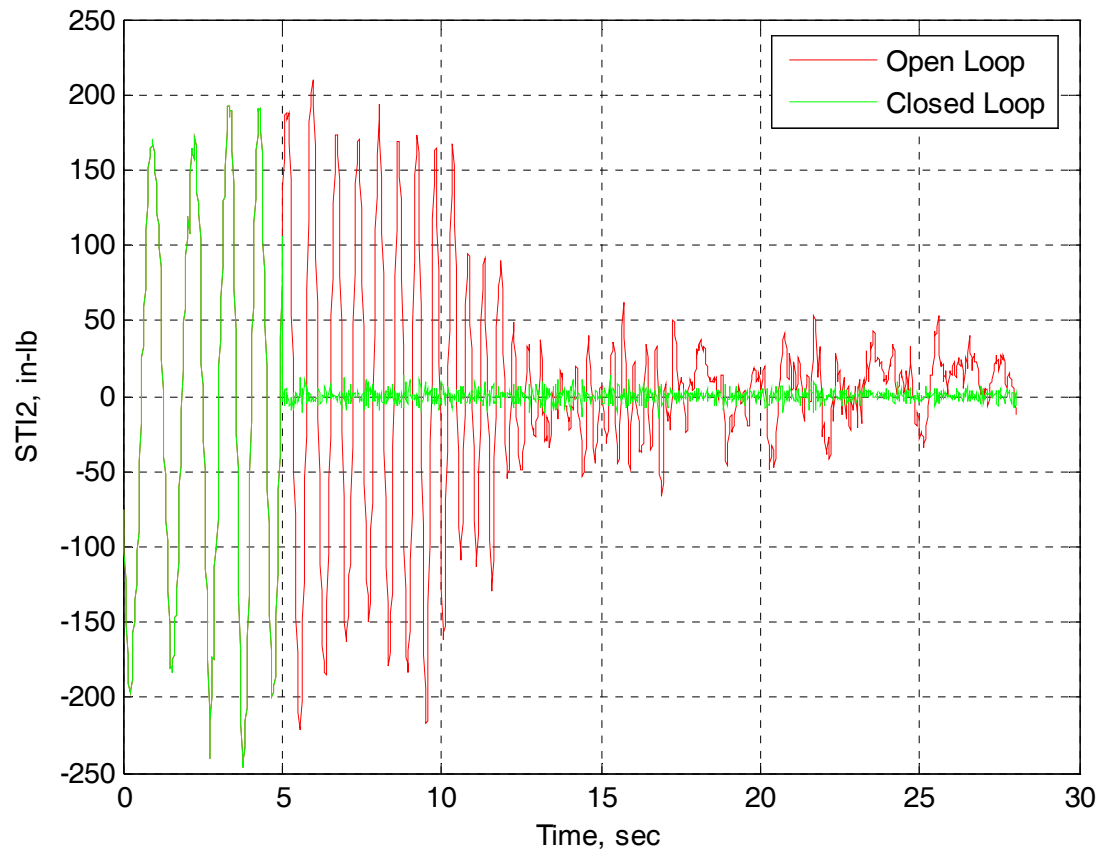


Figure 58.- Time histories of open- and closed-loop torsional moment (STI2) while sweeping gust frequency from 0.5 to 10 Hz. Explicit feedforward.

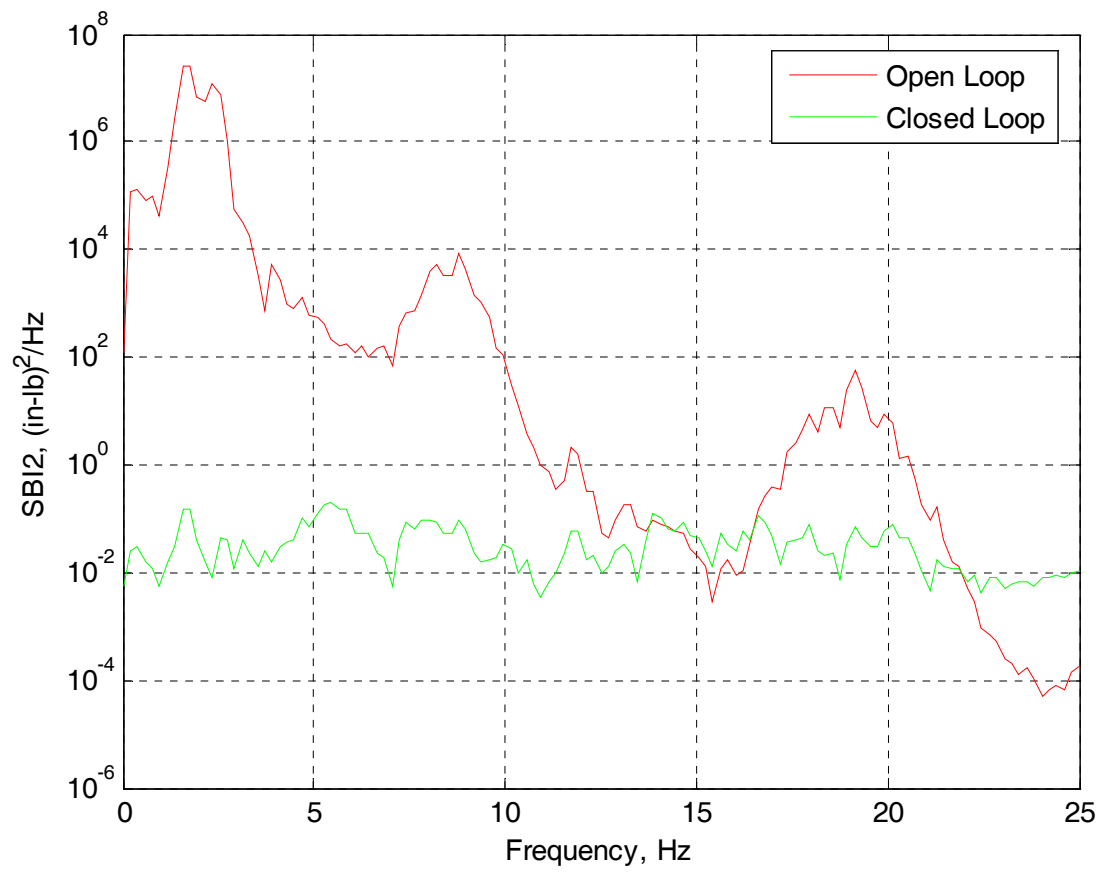


Figure 59.- Open- and closed-loop power spectral densities for vertical bending moment (SBI2) while sweeping gust frequency from 0.5 to 10 Hz. Explicit feedforward.

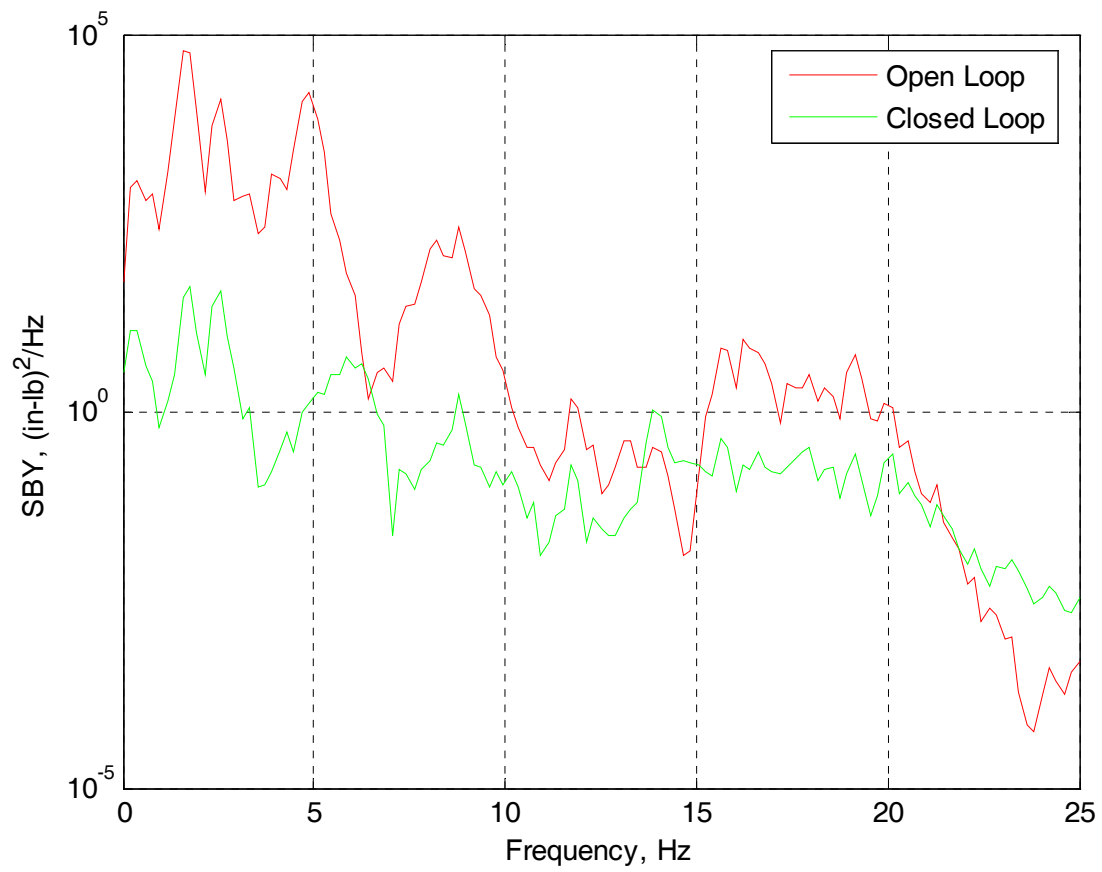


Figure 60.- Open- and closed-loop power spectral densities for fore-and-aft bending moment (SBY) while sweeping gust frequency from 0.5 to 10 Hz. Explicit feedforward.

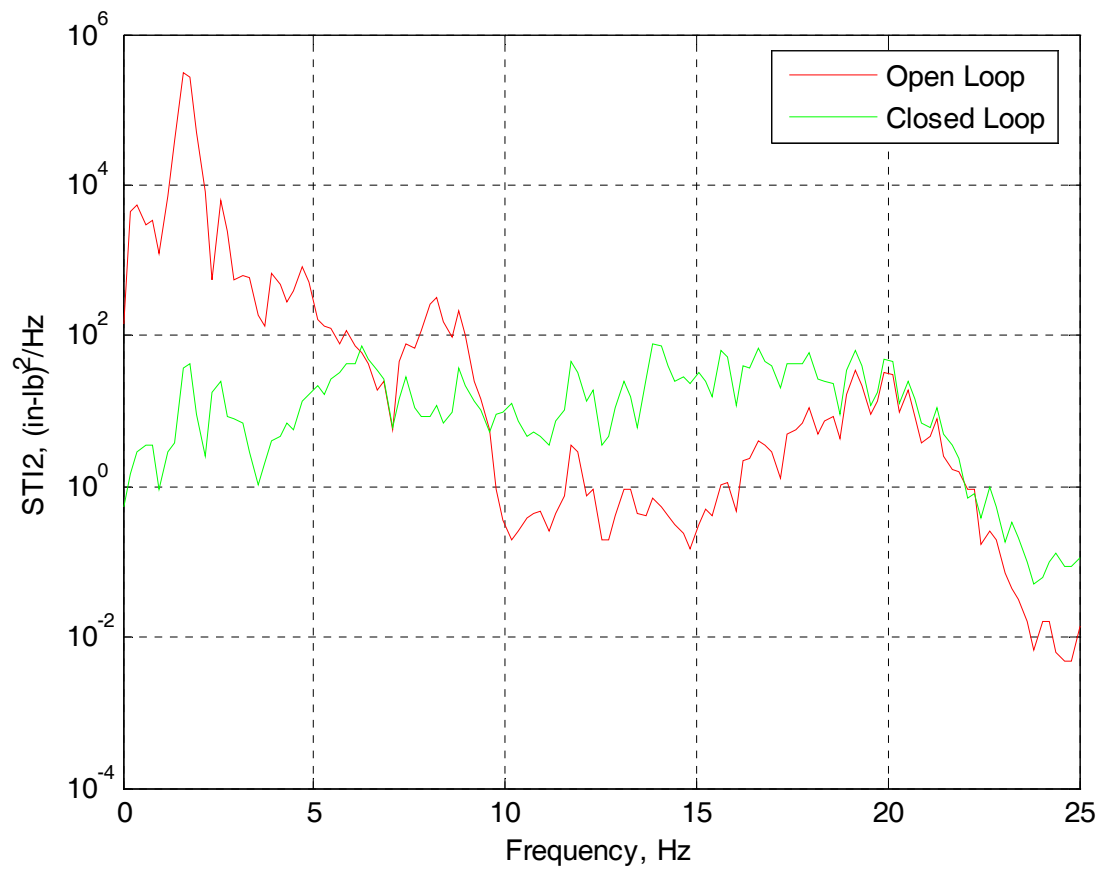


Figure 61.- Open- and closed-loop power spectral densities for torsional moment (STI2) while sweeping gust frequency from 0.5 to 10 Hz. Explicit feedforward.

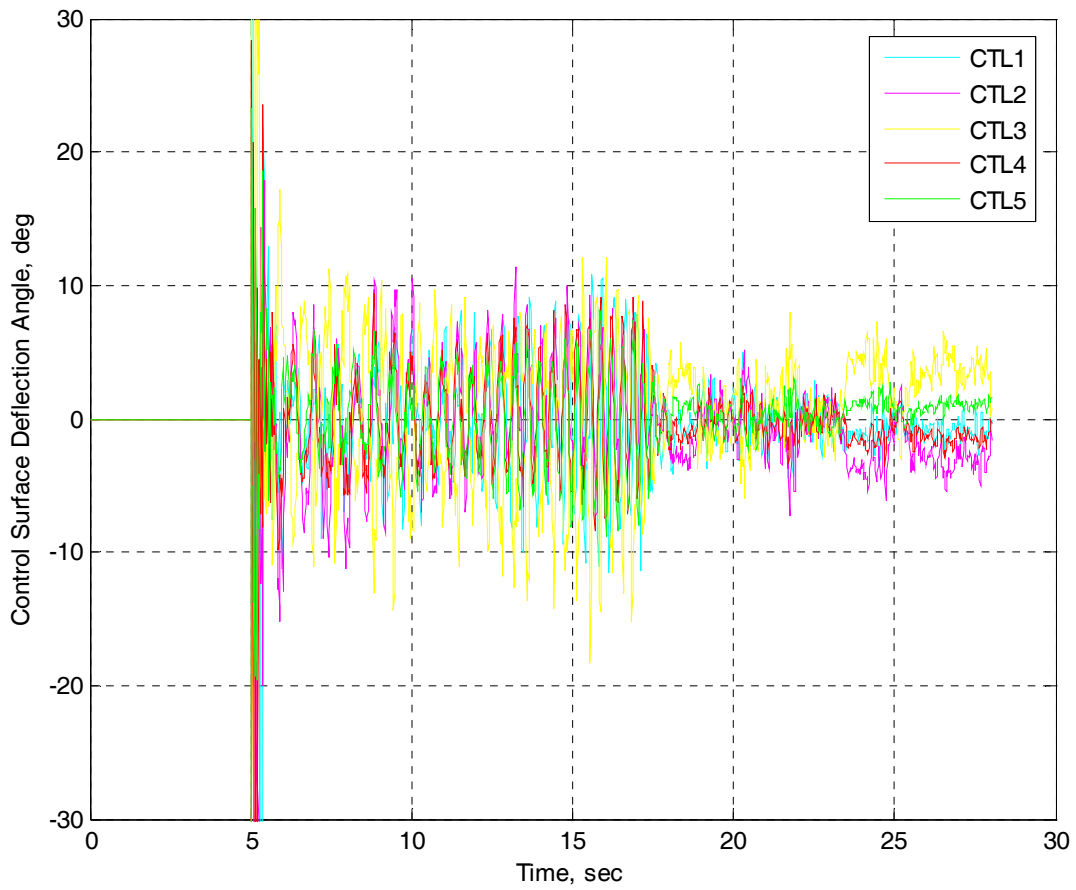


Figure 62.- Time histories of closed-loop control inputs (CTL1-CTL5) while sweeping gust frequency from 0.5 to 10 Hz. Explicit feedforward.

**REPORT DOCUMENTATION PAGE**

*Form Approved  
OMB No. 0704-0188*

The public reporting burden for this collection of information is estimated to average 1 hour per response, including the time for reviewing instructions, searching existing data sources, gathering and maintaining the data needed, and completing and reviewing the collection of information. Send comments regarding this burden estimate or any other aspect of this collection of information, including suggestions for reducing this burden, to Department of Defense, Washington Headquarters Services, Directorate for Information Operations and Reports (0704-0188), 1215 Jefferson Davis Highway, Suite 1204, Arlington, VA 22202-4302. Respondents should be aware that notwithstanding any other provision of law, no person shall be subject to any penalty for failing to comply with a collection of information if it does not display a currently valid OMB control number.

**PLEASE DO NOT RETURN YOUR FORM TO THE ABOVE ADDRESS.**

<b>1. REPORT DATE</b> (DD-MM-YYYY)		<b>2. REPORT TYPE</b>		<b>3. DATES COVERED</b> (From - To)	
<b>4. TITLE AND SUBTITLE</b>			<b>5a. CONTRACT NUMBER</b>		
			<b>5b. GRANT NUMBER</b>		
			<b>5c. PROGRAM ELEMENT NUMBER</b>		
<b>6. AUTHOR(S)</b>			<b>5d. PROJECT NUMBER</b>		
			<b>5e. TASK NUMBER</b>		
			<b>5f. WORK UNIT NUMBER</b>		
<b>7. PERFORMING ORGANIZATION NAME(S) AND ADDRESS(ES)</b>				<b>8. PERFORMING ORGANIZATION REPORT NUMBER</b>	
<b>9. SPONSORING/MONITORING AGENCY NAME(S) AND ADDRESS(ES)</b>				<b>10. SPONSORING/MONITOR'S ACRONYM(S)</b>	
				<b>11. SPONSORING/MONITORING REPORT NUMBER</b>	
<b>12. DISTRIBUTION/AVAILABILITY STATEMENT</b>					
<b>13. SUPPLEMENTARY NOTES</b>					
<b>14. ABSTRACT</b>					
<b>15. SUBJECT TERMS</b>					
<b>16. SECURITY CLASSIFICATION OF:</b>			<b>17. LIMITATION OF ABSTRACT</b>	<b>18. NUMBER OF PAGES</b>	<b>19a. NAME OF RESPONSIBLE PERSON</b>
<b>a. REPORT</b>	<b>b. ABSTRACT</b>	<b>c. THIS PAGE</b>			<b>19b. TELEPHONE NUMBER</b> (Include area code)